COHERENT ABSORPTION IN WEAKLY ABSORBING LAYERS

Giuseppe Pirruccio

The cover image is a pictorial representation of a light beam impinging on a multilayer stack where a layer of graphene is embedded. The light is scattered and propagates in the proximity of the graphene. While the light propagates its energy is dissipated by the graphene.

Coherent absorption in weakly absorbing layers

PROEFSCHRIFT

ter verkrijging van de graad van doctor aan de
Technische Universiteit Eindhoven, op gezag van de
rector magnificus prof.dr.ir. C.J. van Duijn, voor een
commissie aangewezen door het College voor
Promoties, in het openbaar te verdedigen op
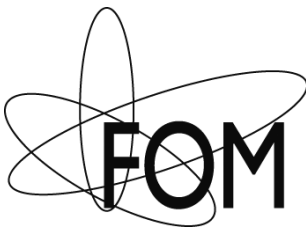maandag 13 november 2014 om 14:00 uur

door

Giuseppe Pirruccio

geboren te Palermo, Italy

Dit proefschrift is goedgekeurd door de promotiecommissie:

voorzitter: prof.dr.ir. G.M.W. Kroesen
1^e promotor: prof.dr. J. Gómez Rivas
2^e promotor: prof.dr. A. Fiore   (Technische Universiteit Eindhoven)
leden: prof.dr. L. Martin-Moreno   (Universidad de Zaragoza)
                 prof.dr. A. P. Mosk   (University of Twente)
                 dr. R.W. van der Heijden   (Technische Universiteit Eindhoven)
adviseur: dr. M. A. Verschuuren   (Philips Research)

Don't stop. No sleep.

Contents

CHAPTER 1

INTRODUCTION

1.1 Optical absorption

Few fundamental natural phenomena are able to dramatically influence our daily life. Light is certainly one of the most striking and evident. Our daily life is regulated, by the alternation of day and night. The vision plays a crucial role in detecting and interpreting information from visible light to build a representation of the surrounding environment. When light intensity is sufficiently high our eyes are able to detect it and images of the outside world are formed on our retina. On the other hand, when light intensity is lower than the detection threshold of our eye, we perceive the world around us as dark. Our eye is not only able to measure the intensity of the light; it is also sensitive to its wavelength, which gives us the experience of the colors. The range of wavelengths which our eye is sensitive to is called the visible range of the electromagnetic spectrum. An object is characterized by a certain color because it absorbs all the wavelengths except those detected by our eye. These particular wavelengths are scattered off the object and they are absorbed by the photoreceptors in our eye. Therefore, we can state that the ability of our vision system to detect light relies on the fundamental processes of scattering and absorption. A classic example is the blue color of the sky, which is caused by the wavelength dependent scattering of sunlight off the molecules of the atmosphere [1].

When light of a certain wavelength interacts with matter it is scattered: it can be transmitted, reflected and absorbed [2]. Following the description of scattering given by Bohren and Huffman [2], if a scatterer is illuminated by an electromagnetic wave, its electric charges are set into oscillation. Accelerated electric charges radiate electromagnetic energy called the scattered field. The incident energy may be absorbed by the scatterer and transformed into different forms (e.g. thermal energy). In this case the scattering is inelastic. Therefore, reradiation and absorption are not independent processes and are both part of the scattering process. A medium is called transparent if most of the light

intensity is transmitted through it and opaque if light is not transmitted. In the latter case, light can be reflected and absorbed. The propagation of light in the material forming the object is described by its refractive index, $\tilde{n}$, defined as the ratio of the speed of light in vacuum and the phase velocity of light in the material. A medium is absorbing if its refractive index is a complex quantity, i.e. $\tilde{n} = n + i\kappa$. This can be easily described in the case in which the light wave propagating in the material along the z-direction can be approximated by a plane wave. In this scenario, by inserting the complex refractive index into the expression for the electric field of the plane electromagnetic wave we obtain

$$\mathbf{E}(z, t) = Re\left[\mathbf{E_0}e^{i(\tilde{k}z - \omega t)}\right] = Re\left[\mathbf{E_0}e^{i\left(\frac{2\pi(n+i\kappa)}{\lambda_0}z - \omega t\right)}\right] = e^{-\frac{2\pi\kappa}{\lambda_0}z}Re\left[\mathbf{E_0}e^{i\left(\frac{2\pi n}{\lambda_0}z - \omega t\right)}\right], \quad (1.1)$$

where $\mathbf{E}_0$ is the amplitude, t is the time, λ_0 is the vacuum wavelength, $\tilde{k}$ is the wavenumber associated to the complex refractive index $\tilde{n}$, $\tilde{k} = 2\pi\tilde{n}/\lambda_0$, and ω is the angular frequency of the wave. We see that $\tilde{k}$ gives an exponential decay along z, as expected from the Beer-Lambert law. From Eq. (1.1), we can define the intensity absorption coefficient as $4\pi\kappa/\lambda_0$. This relation reveal that a material is weakly absorbing in two situations: if $\kappa << 1$ or if it is very thin. The quantity describing the fraction of light absorbed by a medium is called absorption length and it is defined as the distance after which the intensity of the light drops to $1/e$, i.e., $\lambda_0/4\pi\kappa$.

Absorption comes in different tastes, some are helpful, some represent an impediment. For example, in the field of nanophotonics, absorption plays a crucial but often undesired role preventing expected applications because it is typically associated with losses of energy and reduced efficiency of the devices. However, for solar cells and photodetectors, optimizing absorption is the design goal, because the optical power needs to be converted into photocurrent. Another important field of applications in which optical absorption plays a crucial role is Solid State Lighting (SSL). In a typical SSL device a thick phosphor layer is pumped by a blue LED. The blue light is partly absorbed and partly transmitted by the layer. The fraction of the light that is absorbed is efficiently converted into photoluminescence and radiated out of the device. Finding ways to gain control on the absorption of the blue light in the phosphor translates into a better control on the intensity of the photoluminescence. This aspect is extremely relevant in order to gain on the overall efficiency and performance of the SSL device. Moreover, as Eq.(1.1) describes, by enhancing the absorption in the luminescent layer it is possible to reduce its thickness, which leads to a reduction in the material and eventually in the cost of the device.

This thesis focuses on the interaction of light with weakly absorbing materials. By properly structuring the illumination pattern and the materials, we will describe and exploit new ways to considerably enhance light absorption. The materials investigated in this thesis play a crucial role in lighting applications and photodetection.

1.2   Phase controlled absorption and scattering

Scattering of electromagnetic waves by any medium is related to the heterogeneity of that medium. Everything except vacuum is heterogeneous and the fact that a medium possesses a refractive index is itself the macroscopic manifestation of the presence of scattering. If a scatterer (e.g. an electron, an atom, a molecule, or a particle) is illuminated by an electromagnetic wave electric charges are set into oscillatory motion by the electric field of the incident wave. Accelerated electric charges radiate electromagnetic energy. This secondary radiation is called the scattered field. Thus, scattering is excitation followed by reradiation and describes any deviation from free-wave motion. Examples of scattering processes are: diffuse reflection by rough surfaces, diffraction by slits, gratings and edges, specular reflection and refraction at optically smooth interfaces, and also optical absorption. Absorption corresponds to the case in which the reradiated wave and the incident one are in antiphase and interfere destructively.

Absorption is generally measured indirectly. Indeed, it is usually easier to measure the fraction of the light transmitted and diffused by an object than to measure the fraction of the light absorbed. Transmission, reflection and absorption are related with each other by energy conservation, which gives us a convenient way to calculate absorption as the amount of energy which is not transmitted nor reflected. This approach, although being practical, might lead to the misconception of the absorption being a secondary process dependent on transmission and reflection. On the contrary, absorption can be calculated independently using Poynting's theorem,

$$Q = -\nabla \cdot \mathbf{S}, \tag{1.2}$$

where Q is the rate of change of the energy per unit volume, i.e. the time-averaged optical power dissipation density, and $\mathbf{S}$ is the Poynting vector representing the energy flux density, i.e. the rate of energy transfer per unit area. In the case of an electromagnetic field of single frequency and isotropic, dispersive and non-magnetic materials, Q results in [3, 4]

$$Q = \frac{1}{2}\omega\epsilon_0\epsilon''|\overline{\mathbf{E}}|^2, \tag{1.3}$$

where $\epsilon'' = 2n\kappa$ is the imaginary component of the permittivity of the material and $\overline{\mathbf{E}}$ is the total electric field where the overbar indicates the time average over a period. The total dissipated power is then evaluated by integrating Q over the volume occupied by the absorbing medium,

$$A = \int_V QdV. \tag{1.4}$$

In general it is desirable to find ways to control optical properties of systems. This is true also for the optical absorption. Eqs. (1.3) and (1.4) tells us that the optical absorption at a frequency ω is determined by two parameters: the optical properties of the material (ϵ'') and the intensity of the electric field.

Equation (1.4) does not leave much room for an active control of the absorption: once we fix the frequency of the incident wave and the material, ϵ'' is fixed. The electric field appears with a modulus square, which means that the information on the phase of the wave is lost. Therefore, the only parameter that we could vary is the angle of illumination, or more precisely the wavevector of the incident light. Asymmetric structures, indeed, have an angle-dependent optical response function, which leads to an angle-dependent intensity of the electric field intensity in the object.

Because of these limited options to control absorption, researchers have considered for long time absorption as a dull process. Only recently the interferometric property of absorption have been fully uncovered by making use of a proper combination of interference and dissipation in weakly absorbing materials [5]. Indeed absorption is insensitive to the phase of the incident wave only when a single wave is shined on an object. If multiple optical waves are shined on an object it is possible to exploit the phase relation among them by means of the superposition principle. Explicitly, Eq. (1.3) can be generalized to

$$Q = \frac{1}{2}\omega\epsilon_0\epsilon''\overline{\left|\sum_i \mathbf{E}_i\right|^2},\tag{1.5}$$

in which the modulus square is computed after the coherent sum of the vectors describing the electric fields of each wave ($\mathbf{E}_i$) is performed. This approach can be regarded as coherent absorption because it relies on interference between coherent optical fields associated with distinct incident light beams.

1.3   Coherent absorption in thin layers

Many opto-electronic applications and devices rely on light absorption in thin films. For instance, an ideal photodetector or photovoltaic cell should absorb all incident radiation over the range of wavelengths of interest and convert the energy into an electrical signal. Not only should the material absorb all radiation, it should also be thin enough to efficiently collect the photogenerated charge carriers. These requirements, strong absorption and thin materials, seem contradictory. In these cases, the interplay of dissipation and interference can be used to boost the performance of such devices.

Equation (1.5) tells us that, in presence of a non-zero imaginary component of the permittivity of a medium, absorption is caused by the interference of waves in the medium. Due to energy conservation, absorption is maximized when the waves scattered off the medium interfere destructively in the far field. By properly tuning the structural parameters and by designing the illumination scheme it is possible to engineer the far field interference pattern and therefore enhance the absorption. If the interference is completely destructive, perfect absorption is achieved. In the field of plasmonics the possibility of achieving perfect absorption has been recognized by Raether who described the excitation of Surface Plasmon Polaritons (SPPs) at a metal-dielectric interface. He

analyzed the excitation of SPPs in an Attenuated Total Reflectance (ATR) experiment [6]. ATR is an extended technique used to couple plane waves to evanescent modes. The system consists of a multilayer structure in which a prism is used to enable this coupling by providing the required extra momentum to the incident plane wave. The excitation of SPPs is recognized as a minimum in the reflectance. Raether described this minimum in terms of destructive interference between the scattered wave (leaky SPPs) reradiated back into free space radiation and the incoming wave. By tuning the thicknesses of the layers it is possible to match the amplitudes and the phases of these two waves, thus achieving zero reflectance and total absorption in the metal. A complementary way to interpret this total absorption is by considering the losses of the system. Raether identified two damping mechanisms of the SPPs: the internal damping due to ohmic losses and the radiative damping by which the SPP is reradiated out. He demonstrated that the reflectance can be exactly zero when these two damping terms equal each other. Due to total internal reflection the transmittance vanishes, leading to full absorption of the light in the metal layer [6].

In a similar ATR configuration Driessen and de Dood have demonstrated that very thin metal films deposited on a substrate can absorb almost all incident radiation when illuminated with *s*-polarized light [7]. In this case, the reflected and the incident wave are in phase, which creates an antinode in the thin film, a large part of the field is thus contained in the absorbing film.

Total absorption has been also investigated by Yariv in the framework of perfect energy transfer between dielectric waveguides and dissipative microresonators, which shows potential application in a variety of tasks relevant to optical fiber communication, e.g. modulation, switching and dispersion compensation [7–9]. When these two optical elements are placed in close proximity to each other they couple through the evanescent field of the light traveling in the waveguide. Yariv showed that by tuning the dissipation in the ring it is possible to completely transfer the energy from the waveguide to the ring and thereby achieve full absorption [10, 11]. This condition is known as critical coupling [12, 13] and it is the result of perfect destructive interference in the waveguide between the light transmitted through it and the light coupled out from the ring to the waveguide. The required phase-matching is achieved by tuning the length of the ring, while the amplitude-matching is given by the amount of dissipation in the ring. In close analogy to the ATR experiment, also the critical coupling theory is formulated in terms of internal and the out-coupling losses and it is realized when these two loss rates are equal [14].

Very recently a generalization of the concept of critical coupling has been formulated. This concept, known as Coherent Perfect Absorption (CPA), is also explained in terms of optimal interplay between interference and dissipation [5, 15]. The CPA gives a strong theoretical background to the theory of total absorption by drawing the analogy with the time-reversed counterpart of lasing. One way to understand lasing is by considering power balance; the power inside the laser cavity increases because of optical gain, but also decreases as radiation is lost through the cavity boundaries. The condition at which

gain compensates exactly the loss is known as the lasing threshold. The CPA is defined by time-reversing this process: the cavity is now lossy and there is an external supply of light to the cavity. At the point in which absorption compensates exactly for the radiative loss all the incident light is absorbed. The experimental demonstration of CPA has been realized by Wan and coauthors using a double side-polished silicon wafer defining the cavity and two collinear and counterpropagating incident beams [5]. The wavelength in their experiment corresponds to a region of the spectrum at which the silicon is weakly absorbing. Both the incident beams get partially reflected and partially transmitted at the air-silicon interface, exciting Fabry-Perot resonances in the layer. When the thickness of the layer and the incident wavelengths are properly tuned, the transmitted fraction of the first beam interferes destructively with the reflected fraction of the second beam, and viceversa. Light is therefore confined in the layer, and 100% absorption is achieved. Fig. 1.1 schematically shows the comparison between the single beam illumination [Fig. 1.1(a)] and the CPA configuration [Fig. 1.1(b)]. Alternatively, this process can be explained of as follows: the interference of coherent beams leads to an infinite path length (or residence time) of the light inside the cavity [15].

Wan and coauthors theoretically demonstrated that an arbitrary object can be made perfectly absorbing at discrete frequencies if a precise amount of dissipation is added under specific conditions of coherent monochromatic illumination [5]. It can be
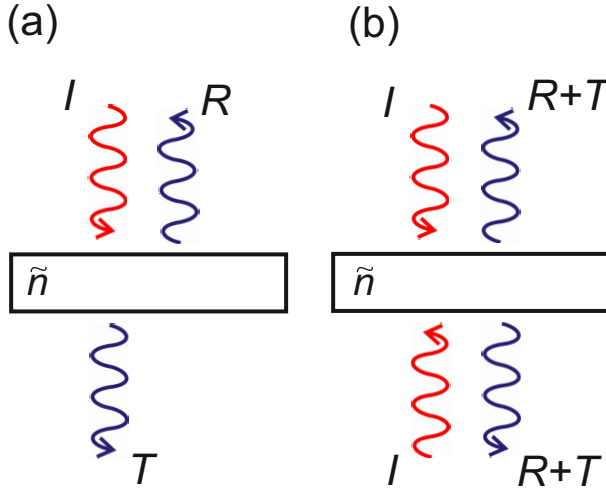
Figure 1.1: (a) A weakly absorbing slab, described by the complex refractive index $\tilde{n}$, is illuminated by a single wave (red curve) with intensity I. which is partially reflected and partially transmitted at the interfaces (blue curves). The intensity of the reflected and transmitted waves are R and T, respectively. Part of the light is absorbed by the slab. (b) Coherent Perfect Absorption configuration, in which the absorbing slab is illuminated by two waves of intensity I (red curves). By properly tuning the thickness and the wavelength of the slab, the scattered field $R + T$ vanishes and 100% is achieved.

rigorously shown within semiclassical laser theory that the first lasing mode in any cavity is an eigenvector of the electromagnetic scattering matrix (S matrix) with an infinite eigenvalue [16]; in analogy to this, the CPA resonances are given by the zero eigenvalues of the scattering matrix [15] (see Chapter 3). The authors demonstrated CPA for a simple two-mode cavity, but this phenomenon should also be possible in more complex systems. One difficulty in attaining perfect absorption in such systems would be producing the interfering excitation modes required by more complex phase patterns. Despite this, there are reasons to be optimistic. First, the time-reversed counterpart of perfect absorption - lasing - has already been achieved in more complex systems [17, 18]. Second, the recent invention of wavefront-shaping provides an unprecedented degree of freedom to control the absorption in complex media [19–23]. Particularly, manipulation and precise control of optical fields at the nanoscale is one of the most important and challenging problems in nanophotonics. Typical experiments are designed to be resonant at certain wavelengths by nanostructured matter, i.e. by fabricating structures which have dimensions comparable to the wavelength of the incident light. The structure of the illumination pattern gives additional degree of freedom in the realization and control of optical resonances.

By properly configuring multiple coherent lightwaves at the condition of critical coupling [24] in a multiple-port SPP resonator Yoon and coauthors theoretically showed that resonant total absorption is obtainable. This investigation has been followed by an experimental demonstration of the plasmonic analogue of the CPA in metallic grating, which can absorb multiple coherent light beams coupled to a single surface plasmon mode. The plasmonic coherent perfect absorption is explained by considering time-reversal symmetry of Surface Plasmon Amplification by Stimulated Emission of Radiation (SPASER) [25]. The plasmonic analogue of the CPA has been extended to spherical and cylindrical geometries by Noh and coauthors [26]. Differently from the previous works, they exploit localized surface plasmon modes instead of propagating SPP.

Kao and coauthors have shown in Ref. [27] that a desired nanoscale light hot spot in a planar metamaterial made of plasmonic resonators, can be engineered by adjusting the far-field spatial profile of the phase of an incoming monochromatic light beam. In this way they show subwavelength localization and absorption of optical energy. The absorption in plasmonic metamaterials much thinner than the wavelength can be modulated by using two collinear and counter-propagating light beams forming a standing wave [28]. The phenomenon relies on the coherent resonant interaction of light beams on the metamaterial. Due to this interaction they observed regimes of near-total absorption and near-total suppression of plasmonic losses, meaning that the interference of beams can eliminate the plasmonic Joule losses of light energy in the metamaterial or, in contrast, can lead to almost total absorption of light. This concept may serve applications in sensors, variable attenuators and in the domain of signal processing. Coherent Perfect Absorption has been also exploited to theoretically demonstrate beam-steering in a free-standing corrugated metal film [29]. The effect is shown to be phase sensitive, yielding CPA and superscattering in the same geometry.

The fields of applications in which Coherent Perfect Absorption can be applied spread well over the abovementioned ones. The concept of wavefront shaping and CPA is fully general and stays valid for all wave phenomena as long as a phase relation between the beams is defined. Fink and coauthors have realized the time reversal of an acoustic wave [30, 31]. The equivalent acoustic version of the CPA has been recently proposed in a similar fashion respect to the original optical experiment [32]. By designing appropriate acoustic metamaterial structures and by using pressure waves, Wei and coauthors showed that it is possible to tune the absorption from unity to zero. This effect can be relevant to attenuate acoustic waves in applications of sound-screening, noise control, and vibration damping.

1.4   Outline of this Thesis

In this thesis we investigate different ways to enhance light absorption in very thin layers of weakly absorbing materials, such as light emitting layers and graphene. These materials play a crucial role in solid state lighting and in novel opto-electronic devices. The efficiency of such devices is limited by the small fraction of the incident light that is absorbed. In order to solve this problem, we designed, modeled and realized novel resonant photonic structures which are able to enhance the interaction of light with the weakly absorbing material. Along the thesis we use a single and a 2-beams illumination scheme. In both cases we explain the results in terms of coherent absorption.

The thesis is organized as follows: in chapter 2 we demonstrate a large light absorptance (80%) in a nanometric layer of quantum dots in rods. This behavior is explained in terms of the coherent absorption by interference of the light incident at a certain angle onto the very thin QR layer. We exploit this coherent light absorption to enhance the photoluminescent emission from the quantum dots in rods reaching up to a seven-fold enhancement of the photoluminescence. In a similar way we also demonstrate the enhanced absorption in a thin layer of Ce^{3+} doped yttrium aluminium garnet, $Y_3Al_5O_{12}$ (YAG:Ce). In this case the incident light couples to the fundamental waveguide mode in the YAG:Ce layer where it is eventually absorbed, resulting in an enhancement of absorption by a factor of 30. In correspondence, we observe a similar increase in emission intensity of photoluminescence caused by the enhanced absorption.

So far we have described how it is possible to control the absorption engineering the interference of scattered waves originating from the interaction of one beam with the sample. In chapter 3 we propose a multiple beam illumination scheme to experimentally demonstrate the possibility of external control and modulation of the intensity of the light emitted by a luminescent layer. The experiment is designed to get as close as possible to the condition for CPA at a wavelength longer than the wavelength at which the absorption coefficient of the YAG:Ce is maximum. This will allow for a reduction of 35% of the Stokes'

shift and, therefore, an increase in the efficiency of the system.

In chapter 4 we experimentally demonstrate a broadband enhancement of the light absorption in graphene over the whole visible spectrum. We reach an enhancement factor of almost an order of magnitude. This enhanced absorption is obtained in a multilayer structure by using an Attenuated Total Reflectance (ATR) configuration and it is explained in terms of coherent absorption arising from interference and dissipation. The interference mechanism leading to the phenomenon of coherent absorption allows for its precise control by varying the refractive index and/or thickness of the medium surrounding the graphene.

Metallic arrays of nanoparticles sustain optical modes which are able to spatially localize the electric field in certain regions. By combining such arrays with a monolayer of graphene it is possible to enhance the light-matter interaction in the graphene layer, thus boosting its absorption. In chapter 5 we design, simulate and optically characterize a device which should exhibit almost one order of magnitude wavelength-dependent enhanced absorption. The enhanced absorption should translate into an enhanced photocurrent. This strategy will allow to overcome some of the main problems of the applications involving graphene, namely, its low absolute absorption and its spectral insensitivity.

CHAPTER 2

COHERENT ABSORPTION IN THIN LIGHT-EMITTING LAYERS

Light-emitting layers are one of the fundamental building blocks of solid state lighting devices. They are typically used as light-converting elements because of their ability to absorb light of a certain wavelength and emit at a longer wavelength with high quantum efficiency. In order to optimize the efficiency of these devices, it is desirable to minimize the thickness of the light-emitting layers, while maintaining high the absorption . In this chapter we present two experiments in which, by using the same method, we boost the absorptance of a nanometric layer of quantum dots in rods (QRs) and of a thin layer of Ce^{3+} doped yttrium aluminium garnet, $Y_3Al_5O_{12}$ (YAG:Ce). These results are explained in terms of the coherent absorption by interference of the light incident at a certain angle onto the layers. Because of this effect, the absorption in the QRs and in the YAG:Ce are enhanced from 10% to 80% and from 1.5% to 44%, respectively. Consequently, a photoluminescence enhancement factor of 7 and 30 is measured for the two systems, respectively. A complementary explanation in terms of coupling of the incident light to guided modes is provided for both experiments.

2.1 Introduction

With the development of nanotechnologies it has become possible to scale down the dimensions of electro-optical devices. For certain applications, e.g., in solid state lighting, photovoltaics and photodetection, it is crucial to find new methods to enhance the optical absorption in very thin layers of different materials [33–35]. Consequently, enhanced optical absorption by nanostructures and metamaterials has been intensively investigated in recent years [7–9, 33, 36–38]. One promising possibility relies on engineering the far field scattering of such structures by tailoring phase and amplitudes of the scattered waves. By defining a destructive interference pattern in the far field, it is possible to confine the incident light in the nanostructure, thus enhancing absorption. Following this reasoning the concept of Coherent Perfect Absorption (CPA) has been recently introduced and described as the interplay between interference and dissipation [5]. CPA, and more in general the concept of coherent absorption, fully reveals its potential when multiple light beams are incident on the structure. However, even in its simplest realization, enhanced absorption can be achieved with a single incident light beam by properly tuning the geometrical structural parameters of the sample.

In this chapter we present two experiments in which we demonstrate coherent absorption in very thin absorbing layers. In the first experiment we choose colloidal quantum dots in rods (QRs) as the constituent material of a 23 nm-thick layer. Quantum dots are a class of materials with characteristic optical properties, such as the tunability of their emission spectrum, and their high quantum efficiency if their surface is passivated [39]. For the second experiment we choose Ce^{3+} doped yttrium aluminium garnet, $Y_3Al_5O_{12}$ (YAG:Ce). YAG:Ce is an important material because of its excellent luminescent properties, chemical durability, and thermal stability. One main application of this material is in white light emitting diodes (LEDs): when excited with a blue emitting InGaN LED, the combination of the yellow emission of YAG:Ce with the non-absorbed blue light generates white light [40]. Among various morphologies, transparent YAG:Ce thin films are of technological interest for many optical applications because of their superior thermal conductivity, high degree of uniformity and better adhesion. In particular the transparency of YAG:Ce is crucial because it is used in PET scanners, high-energy gamma radiation and charged particle detectors [41, 42]. The absorption length of YAG:Ce with a typical Ce^{3+} concentration less than 1 mol% is on the order of 100 μm for light with a wavelength around 450 nm [43, 44]. Increasing the absorption of YAG:Ce reduces the amount of material required for an efficient light conversion and therefore it would enable the use of thin-films of YAG:Ce for solid state lighting.

We have designed the sample and the experiment such that an efficient conversion of incident light into pholuminescence is achieved by means of enhanced absorption. For the QR layer we demonstrate a significant enhancement of the absorptance of the incident light at λ=457 nm which reaches 80% for *s*-polarized light and 70% for p-polarized light at a certain angle of incidence. These absorptances lead to a seven- and five-fold enhancement of the QR photoluminescence for *p*- and *s*-polarized excitation,

respectively. We also demonstrate an enhanced absorptance up to 44%, corresponding to a factor of 30, in the YAG:Ce layer, with a concomitant similar enhancement of its photoluminescence.

In this chapter we make use of the Attenuated Total Reflectance (ATR) technique. Our structures consist of (very) thin layers of absorbing material. ATR is an extended technique used to couple plane waves to evanescent modes in which a prism is used to enable this coupling. A typical ATR measurement is characterized by a minimum in the specular reflectance at an angle of incidence larger than the critical angle for total internal reflection at the prism-structure interface. An interpretation for the ATR resonance, based on quantum interference, has been provided in Refs. [45, 46]: when the momentum-matching condition between the incident wave and the evanescent mode is realized an additional photon path, besides the radiative scattering, opens. The relation between this interpretation and the coherent absorption is provided by the interference nature of the two phenomena. In the ATR experiment, the interference is due to the superposition of the probability amplitudes of two events: the photon scattered out because of the total internal reflection, and the same photon coupled first into an evanescent mode and coupled out into radiation. In the resonant condition the radiative damping of the evanescent mode equals the internal damping due to losses in the material, and all the light is absorbed. The quantum interpretation can be rephrased classically in terms of interference of electromagnetic waves, in which the first photon path corresponds to the reflected wave at the prism-structure interface and the second one to the leaky wave associated with the evanescent mode [6]. This classical interpretation is similar to the so-called critical coupling by which it is possible to perfectly transfer energy between two optical media [10, 11]. Similarly to ATR, also in the critical coupling theory, there is a relation between the internal and the out-coupling losses, namely, when they are equal it is possible to absorb 100% of the incident light [14].

CPA, ATR and critical coupling are phenomena characterized by a general scheme, i.e., in all of them optical interference and dissipation lead to an efficient electromagnetic energy transfer into a structures and an enhanced absorption. In our experiments the structure we want to transfer the energy to are the QR and YAG:Ce layer.

2.2 Sample description and experimental details

2.2.1 Quantum dots in rods

For the first experiment we use CdSe/CdS quantum dots-in-rods as the constituents of the nanometric layer. The QRs have been synthesized following the procedure described in Ref. [47]. They have an average length of 36 nm and an average diameter of 4 nm. The absorbance and normalized emission spectra of as grown CdSe/CdS nanorods in suspension in toluene is shown in Fig. 2.1(a). The weak absorption at the emission wavelengths of the CdSe/CdS QRs limits the self-absorption. The quantum efficiencies
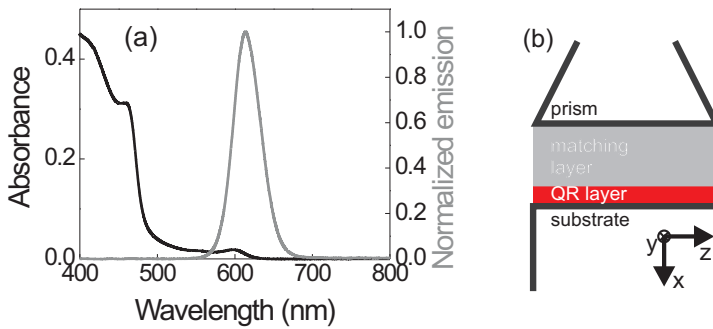
Figure 2.1: (a) Absorbance (black curve) and normalized emission spectra (gray curve) of CdSe/CdS quantum dot-in-rods. (b) Schematic representation of the sample, i.e., F2 glass prism, silica matching layer, QR layer and quartz substrate.

of the QRs suspended in toluene and forming a layer in air have been determined to be 70% and 40%, respectively. The reduction of photoluminescence quantum efficiency of the rods in the layer is explained by the increased probability for energy transfer between adjacent rods. In particular, an exciton in a close-packed QR layer has a higher probability to end up in a non-emitting rod, which leads to a decrease of the quantum efficiency of the ensemble of nanorods.

Since our goal is to exploit the principle of the coherent absorption in the ATR configuration, we have fabricated a sample with the structure schematically represented in Fig. 2.1(b). A suspension of quantum dots-in-rods in toluene is spin-coated on top of a silica substrate with a refractive index of 1.45. After baking the sample for 2 minutes at 80° C, a high-density layer of QRs with a thickness of 23 nm is formed on the substrate. Figure 2.2(a) displays a scanning electron microscope (SEM) image of the layer tilted in order to appreciate its thickness. A silica layer with refractive index 1.46 and a thickness of 350 nm, indicated as matching layer in Fig. 2.1(b), is evaporated on top of the QR layer. The thickness and refractive index of this layer are critical to achieve coherent absorption in the QR layer. The optical constants and the thicknesses of the QR and matching layers have been determined with spectroscopic ellipsometry. Figure 2.2(b) displays ellypsometry measurements of the real, n (black curve), and imaginary, κ (gray curve), components of the refractive index of the QR layer. Two peaks are visible at λ=460 nm and λ=600 nm in the curve of the imaginary component of the refractive index. These peaks correspond to absorption due to resonant excitation of excitons in CdS and CdSe respectively.

An F2 Schott optical glass prism, with refractive index 1.62 at $\lambda = 600$ nm, on top of the sample is used in the ATR configuration. In order to obtain a good optical contact between the prism and the matching layer and to avoid multiple reflections that will destroy the
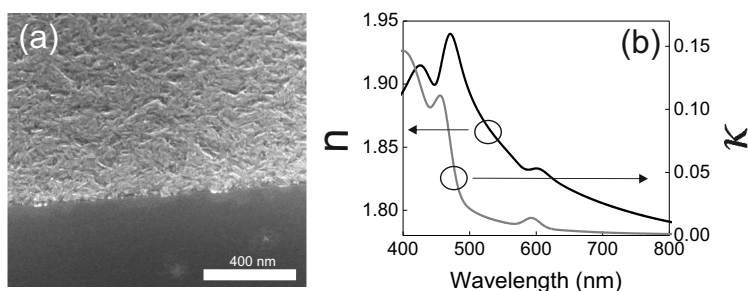
Figure 2.2: (a) Tilted scanning electron microscope image of the top surface of the QR layer spin-coated over a quartz substrate. (b) Real (black curve) and imaginary (gray curve) components of the refractive index of the QR layer as a function of the wavelength.

interference in the QR layer, we have used a refractive-index-matching liquid with the same refractive index as F2.

2.2.2 YAG:Ce

YAG-based films can be fabricated through several methods, such as sputtering [48, 49], spray-inductively coupled plasma technique [50], metal organic chemical vapor deposition (MOCVD) [51], and pulsed laser deposition [52]. Sol-gel approaches have

Figure 2.3: SEM images of the thin films of YAG:Ce prepared on fused silica glass (a) or sapphire substrates (b-d) heated at different temperatures: (a) 1000°C; (b) 1200°C; (c) 1400°C; (d) 1500°C. The top right insets in (a) and (b) show cross section images of the sample, and the bottom left inset in (a) shows an optical photograph of the film on a fused silica substrate (3 cm x 3 cm) heated at 1000°C.

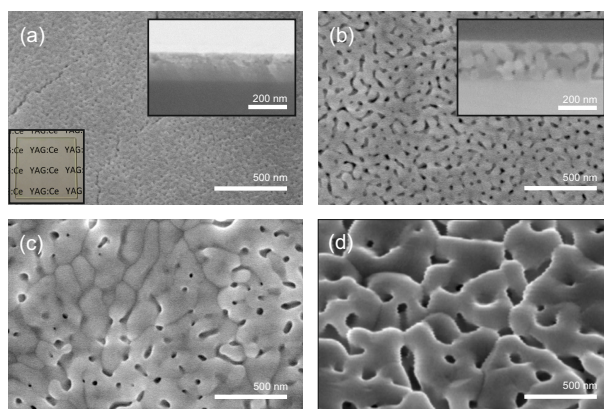also been exploited to produce thin films [52–54]. Although sol-gel approaches do not require complex equipment as in vapor-phase approaches, making transparent and uniform films with an optical thickness over 100 nm usually requires repeated deposition processes [52, 54]. We have developed a method for fabricating thin layers of YAG:Ce based on a sol-gel approach with propylene oxide as a gelation initiator. A single spin-coating process followed by a sequence of heat treatments allows the fabrication of polycrystalline YAG:Ce thin layers with a thickness of 200 nanometers. This epoxide-catalyzed sol-gel method has been originally reported by Gash et al. in Refs. [55, 56].

Thin transparent YAG:Ce layers are interesting for optical applications. In this paragraph we present a study of surface morphology, crystallite size, and quantum efficiency (QE) as a function of heat treatment temperature. Figure 2.3 shows SEM images of the films prepared using different heat treatment temperatures. The film heat-treated at 1000°C, shown in Fig. 2.3(a), is made on fused silica glass, while other films treated at 1200, 1400, and 1500°C, respectively, are processed on sapphire substrates. Fused silica cannot be used above 1100°C, corresponding to the glass transition temperature above which the
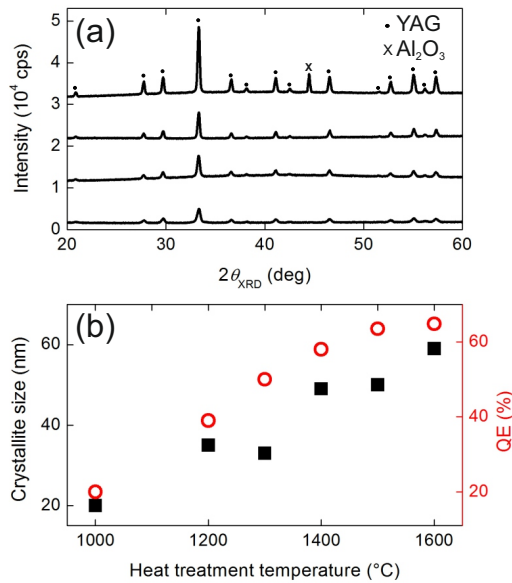
Figure 2.4: (a) X-ray diffraction patterns of the thin YAG:Ce films heated at different temperatures: 1000, 1200, 1400, and 1500°C from bottom to top. The measurements are shifted vertically in steps of 104 cps for the sake of clarity. The peaks observed in the patterns have been attributed to YAG(indicated by the dots) and Al_2O_3 (indicated by the cross). (b) Crystallite size (left ordinate, solid squares) derived from Scherrer relation and photoluminescence quantum efficiency (right, open circles) as a function of heat treatment temperature.
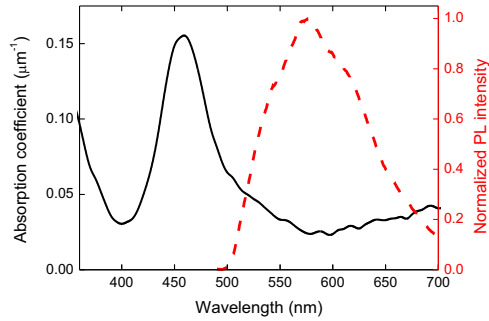
Figure 2.5: Absorption spectrum (left ordinate, black-solid curve) and emission spectrum (right, red-dashed curve) for a 200 nm thick YAG:Ce layer deposited on a SiO$_2$ glass heat-treated at 1000°C.

SiO$_2$ reacts with the YAG:Ce layer. SEM images show the porous structure of the YAG:Ce layer consisting of grains and voids, which become bigger with the increment of the heat treatment temperature. The bottom left inset of Fig. 2.3(a) shows an optical photograph of the sample, in which the uniformity and transparency of the layer heated at 1000°C can be appreciated. For the films heated at 1000°C [Fig. 2.3(a)] and 1200°C [Fig. 2.3(b)] the sizes of grains and pores are much smaller than that of the optical wavelength, and the films are transparent and non-scattering in the visible range. The top right insets of Figs. 2.3(a) and (b) show cross sections of the samples heat-treated at 1000°C and 1200°C, respectively. The thickness of the layers is around 200 nm and is uniform over long distances. As the heat-treatment temperature is increased up to 1400°C and higher, the grains and voids grow making the layer opaque due to light scattering.

Figuere 2.4(a) shows X-ray diffraction patterns for the films heated at different temperatures. Thin films heated at 1000°C and higher temperatures show diffraction lines that are assigned to the crystalline phase of YAG, meaning that the gel crystallized during the heat treatment. As the heat-treatment temperature increases, the diffraction peak intensities rise and the linewidths narrow, indicating the growth of YAG crystallites. Figure 2.4(b) shows the crystallite sizes estimated from the width of the diffraction line using the Scherrer relation [24], as a function of heat-treatment temperature. We also plot the photoluminescence QE in the same figure. With the increased heat-treatment temperature, both the crystallite size and QE increase. There is a trade-off relation between a high QE and good optical transparency. The QE gets higher as the heat-treatment temperature increases, the film becomes translucent due to scattering by the larger grains and voids in the layer as it can be seen by comparing the SEM images in Figs. 2.3(a) and (d).

Figure 2.5 shows a typical absorption (black solid curve) and emission (red-dashed curve)

spectrum of the film. The sample layer was prepared on a fused silica glass substrate and heat-treated at 1000°C. It shows an absorption band at 460 nm, which is assigned to the electron transitions from the 4f ground state to the 5d excited states of Ce ions in the YAG lattice. The absorption coefficient is about 0.1 μm^{-1} at a wavelength λ of 488 nm, which corresponds to an absorption length of 10 μm. The absorption length is shorter compared to the typical reported values of ~100 μm [43, 44] because of a higher concentration of Ce^{3+} (5 mol%) used in our sample. The emission spectrum shown in Fig. 2.5 (red-dashed curve) was taken by exciting the sample at λ = 488 nm with a continuous wave laser diode. The thin YAG:Ce layer (200 nm) fabricated on a fused silica substrate was coated by a SiO_2 layer (240 nm) deposited by sputtering. The sample was placed in contact with a prism (N-SF11, refractive index n = 1.79), with the SiO_2 thin layer facing to it, using a refractive index matching oil (n = 1.79) in between.

2.3   Absorption measurements

The ATR measurements were performed as follows: the prism was illuminated with a collimated s- or p-polarized beam from a halogen lamp and varying the angle of incidence, θ. The specular reflection was measured in steps of θ = 0.1° with a multimode optical fiber coupled to a spectrometer. The angle of incidence was varied by rotating the sample with a computer controlled rotational stage. In order to obtain the specular reflectance, R, of the QR layer, the reflection measurements were normalized by the reflection at an angle above the critical angle for total internal reflection at the prism-matching layer interface, i.e., an angle at which the reflectance is 1.

2.3.1   Quantum dots in rods

For angles larger than the critical angle for total internal reflection the transmission through the sample is negligible, so 1-R gives directly the measurement of the absorptance in the QRs layer. In Fig. 2.6 we display the measured (a) and the calculated (b) absorptance (color scale) for s-polarized light as a function of the angle of incidence (θ) and the wavelength. The calculation is performed using the transfer matrix method for a multilayer structure [57]. In these calculations we fix the thickness and refractive index of the QR and matching layer, as obtained from the ellipsometry measurements. Therefore, we do not use any free parameter to fit the measurements. Figure 2.6(c) displays the cut of the absorptance measurement (open circles) and calculation (solid curves) at λ = 457 nm. These wavelength correspond to the wavelength used to excite the QRs in the photoluminescence experiments shown in the next section. The absorptance in Fig. 2.6(a) is low for angles larger than $\theta \simeq 64°$ and for wavelengths larger than 550 nm. This is due to the total internal reflection at the prism-matching layer interface above the critical angle. The pronounced peak in absorptance around θ = 65.5° and λ = 450 nm is due to the coherent absorption. The excellent agreement between measurements and calculations confirms the validity of the transfer matrix method to describe the light scattering in this multilayer structure. This remarkable result, in view of the inhomogeneities in the QR
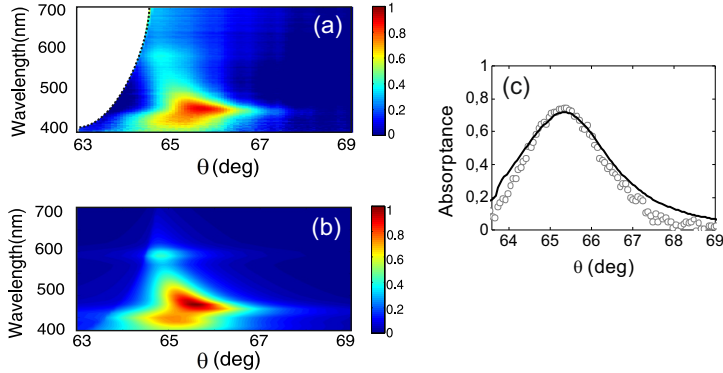
Figure 2.6: (a) Measured and (b) calculated absorptance from the sample represented in Fig. 2.1(b) of *s*-polarized light (color scale). The absorptance is displayed as a function of the wavelength and the angle of incidence. (c) is the experimental (open circles) and calculated (solid lines) absorptance at $\lambda = 457$ nm as a function of the angle of incidence.

layer [see Fig. 2.2(a)], can be explained from the fact that ellipsometry measurements include the effect of the roughness as an effective property of the layer.

We performed the same kind of measurements also for *p*-polarized incident light. Figure 2.7(a) displays with open circles the *s*- (black circles) and *p*-polarized (grey circles) absorptance for $\theta > \theta_c$ at $\lambda = 457$ nm. The dotted vertical line in this figure indicates the critical angle for total internal reflection. The maximum in absorptance reaches the extraordinarily large value of 80% at $\theta = 65.5°$ and 70% at $\theta = 64.2°$ for *s*- and *p*-polarized illumination, respectively. This is a remarkable result considering that absorption takes place only in the 23 nm-thick QR layer. The shift of the maximum in absorptance between *s*- and *p*-polarized light can be explained by the different phase shifts in the reflection at the interfaces for the two polarizations that modifies the interference condition for coherent absorption. We note that the absorption length, i.e., the length over which the intensity decreases by a factor $1/e$ under plane wave illumination, at $\lambda = 457$ nm in a thick layer of a material with the refractive index of the QR layer is on the order of 350 nm for both polarizations. Therefore, coherent absorption in the QR layer leads to a reduction of the absorption length by more than 1 order of magnitude.

In this system coherent absorption is achieved by matching the phases and the amplitudes of the reflected waves. These quantities depend on the reflection Fresnel coefficients of the system, which, in turn, depend on the thicknesses and refractive indices of the layers. Therefore, it is possible to calculate the value of the thickness of the matching layer which maximizes the absorptance. In Fig. 2.7(b), we plot the calculated absorptance at $\lambda = 457$ nm for *s*-polarization (gray curve) and *p*-polarization (black curve) using optimized values for the thicknesses of the matching layer to achieve total absorptance at a certain angle. This thickness corresponds to 480 nm for *p*-polarization and 230 nm for *s*-polarization. The difference in the two optimum thicknesses is due to the different amplitudes and
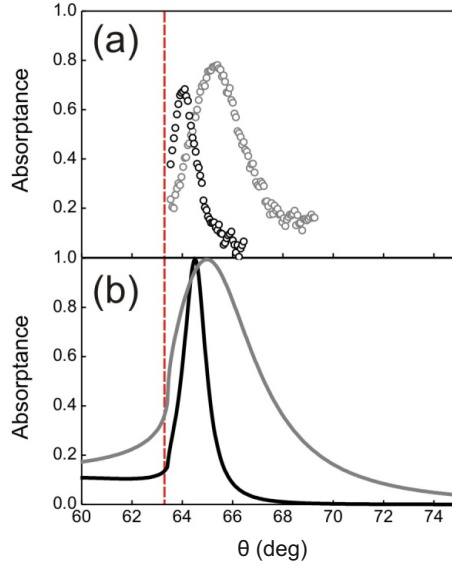
Figure 2.7: (a) Experimental absorptance of *p*-polarized (open black circles) and *s*-polarized (open gray circles) light with $\lambda = 457$ nm incident onto the sample schematically represented in Fig. 2.1(b), as a function of the angle of incidence.   (b) Calculated absorptance for *p*-polarized (black curve) and *s*-polarized (gray curve) incident light with an optimized thickness of the matching layer [see Fig. 2.1(b)] in order to obtain maximum absorptance. The red dashed line indicates the critical angle for total internal reflection at the interface between prism and matching layer.

phases of the fields reflected at each interface of the multilayer structure for *p*- and *s*-polarization.   This difference makes it impossible to achieve 100% absorption for unpolarized light in a single sample. Nevertheless, the sample used in our experiments, with a matching layer of 350 nm, exhibits a significant enhancement of the absorption for both polarizations.

The interference mechanism leading to the coherent absorption in the QR layer can be appreciated by calculating the field intensity in the multilayer structure. This calculation is displayed in Fig. 2.8 for *s*-polarized incident light with a wavelength of 457 nm at four different angles, namely, $\theta = 62°$ (a), $64.2°$ (b), $65.4°$ (c) and $66.5°$ (d). The color scale in these figures represents the spatial distribution of the field intensity normalized by the incident intensity. The absorbed electromagnetic power in a medium is given by $\int_V \frac{\omega}{2}\epsilon_0 \epsilon'' \overline{|E|^2} dV$ [3], where ω is the angular frequency of the wave, ϵ'' is the imaginary component of the permittivity of the medium, ϵ_0 is the vacuum permittivity and E is the total electric field where the overbar indicates the time average over a period. In our system the only absorbing material with $\epsilon'' \neq 0$ is the QR layer and the integral
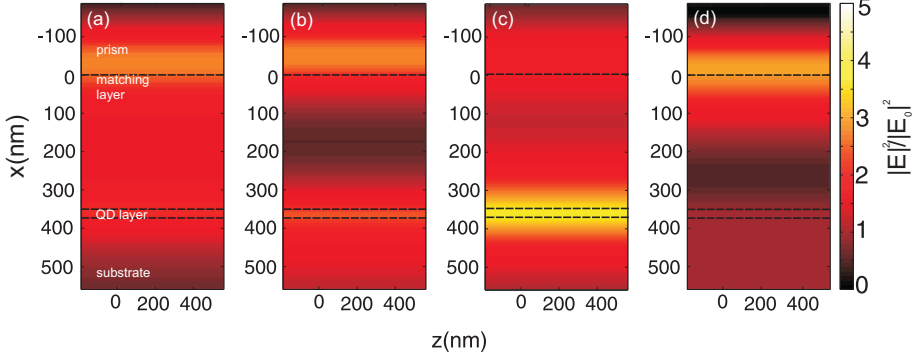
Figure 2.8: Calculated spatial distribution of the electric field intensity normalized by the incident electric field intensity along the cross section of the sample schematically represented in Fig. 1(b). In this calculation an incident plane wave of $\lambda = 457$ nm and s-polarization impinges at an angle of incidence of (a) $\theta = 62°$, (b) $64.2°$, (c) $65.4°$ and (d) $66.5°$.

needs to be evaluated in the volume occupied by this layer. At $\theta = 62°$ [Fig. 2.8(a)] the field intensity in the QR layer is low. Therefore, for this angle of incidence also the absorptance in the QR layer is low. At $64.2°$ [Fig. 2.8(b)] the angle of incidence approaches the angle for coherent absorption. Consequently, the field intensity in the QR layer is higher. The normalized field intensity is also high at the prism-matching layer interface due to total internal reflection. This situation changes drastically at $65.4°$ (Fig. 2.8(c)), where the coherent absorption condition is reached. For this angle of incidence the fields interfere constructively in the QR layer where the intensity increases. This field enhancement in the layer leads also to the enhancement of the absorbed power in the otherwise weakly absorbing QRs. For this angle of incidence, we observe a reduction of the intensity at all locations other than the QR layer. This reduction is the result of the concomitant destructive interference required by the conservation of energy. At $\theta = 66.5°$ the absorptance is low [Fig. 2.8(d)]. For this angle the normalized field intensity in the QR layer is also low, while at the prism-matching layer interface it is maximum due to total internal reflection.

As anticipated and explained in the introduction, a description of the mechanism leading to coherent absorption in our system, considers the coupling of the incident radiation into the quasi-bounded fundamental mode supported by a lossy waveguide. The waveguide is defined by the QR layer with an effective index of refraction larger than the surrounding media and the losses are given by absorption in the layer and through radiation into the prism. To illustrate this explanation, we have calculated the eigenfrequencies associated with the fundamental transverse electric field eigenmode (TE_0 mode) of a waveguide with a thickness of 23 nm and a permittivity equal to the effective permittivity of the QR layer obtained from ellipsometry. The effect of the roughness was taken into account in this calculation since the imaginary component of the effective refractive index, obtained from
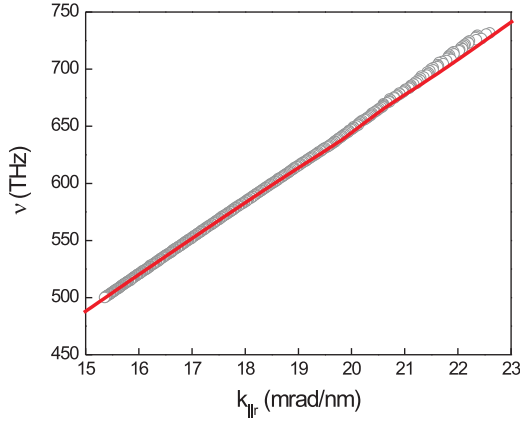
Figure 2.9: Dispersion relation of the TE_0 mode in a homogeneous layer with a thickness of 23 nm and a permittivity given in Fig. 2.2(b) (red line). Open circles are the experimental data extracted from the measurements of Fig. 2.6(a).

ellipsometry, includes a reduction in the intensity of the specular reflection due to both absorption and scattering in the QR layer. The waveguide frequencies are represented as a function of the wavenumber of the mode in the dispersion diagram shown in Fig. 2.9 with the solid line. In these calculations, we consider the layer embedded in a homogenous dielectric, i.e., we do not consider the prism. There is a good agreement with the measured data represented by the open circles in Fig. 2.8, which means that we are experimentally close to the condition for critical coupling to the TE_0 mode and the approximation of neglecting the prism is therefore valid. These measurements have been obtained from the attenuated total reflectance data (Fig. 2.6) by determining the wavelengths and angles of maximum absorptance and representing them as a function of the frequency, $\nu = c/\lambda$, and the in-plane wavevector, $k_\parallel = \frac{2\pi}{\lambda} \sin(\theta)$. The maxima in the absorptance measurements of Fig. 2.6(d), corresponding to the minima of the reflectance, can be described as the result of destructive interference between the leakage radiation of the TE_0 mode through the prism and the specular reflection of the incident beam at the prism-matching layer interface.

2.3.2 YAG:Ce

The interpretation of the coherent absorption in terms of coupling of light to quasi-bound modes supported by the absorbing layer can be applied to explain the enhanced absorption in the YAG:Ce. In general, one way for enhancing the absorption is to increase the amount of Ce^{3+} ions in the YAG crystals. However, if the concentration is higher than a certain value (typically > 5 mol%), the YAG:Ce slab exhibits concentration quenching,
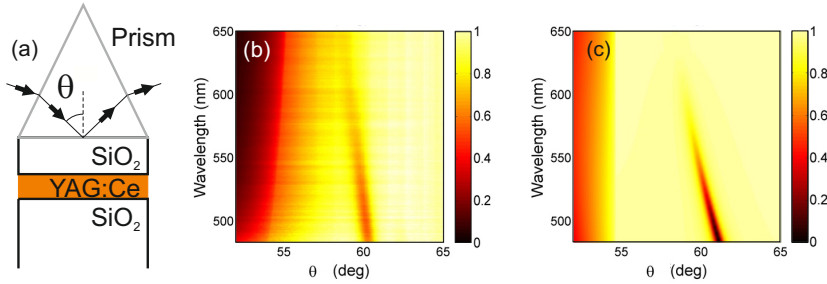
Figure 2.10: (a) Schematic illustration of the experimental setup used to couple incident light into the YAG:Ce thin layer. As a sample, we used the YAG:Ce layer (thickness = 200 nm) on the fused silica glass substrate heat treated at 1000°C with a SiO$_2$ layer (thickness = 240 nm) sputter-deposited on top. (b) and (c) Experimental and calculated specular reflectance spectra as a function of incident internal angle for p-polarized light.

resulting in a reduced quantum efficiency (QE) and decreased emission intensity. An alternative approach to increase the absorption in thin layers of YAG:Ce is to couple the blue light into waveguide modes that propagate inside the layer. In this case, the YAG:Ce layer acts as a slab waveguide and increases the effective length over which it interacts with the light. The coupled light is eventually absorbed as it travels through the layer, and the absorption is enhanced. Although the coupling of light into waveguide modes is a well-studied process, it has gained a renewed attention recently as a method to enhance light harvesting efficiency [58]. The coupling to these modes for certain wavelengths and angles of incidence, is revealed by a reduction of the specular reflection.

The experimental configuration is schematically shown in Fig. 2.10(a). For the measurement, a SiO$_2$ layer (240 nm) was sputtered on top of the YAG:Ce layer (200 nm) made on a fused silica substrate heat-treated at 1000°C. A fused silica substrate was used in these measurements because of its lower refractive index compared to the YAG:Ce layer, which has a refractive index of $n = 1.70$ at $\lambda = 488$ nm as extracted from variable angle spectroscopic ellipsometry. Waveguide modes cannot be supported in a YAG:Ce layer when it is surrounded by sapphire because of its high refractive index ($n = 1.78$ at $\lambda = 488$ nm). The sample was illuminated with a collimated white light beam through the prism with an internal angle of incidence θ and the specular reflectance was collected as a function of θ.

In Fig. 2.10(b), the specular reflectance of p-polarized light is plotted in a color map as a function of the angle and wavelength of incidence. One can see an abrupt change in reflection around $\theta \sim 55°$, corresponding to the critical angle for total internal reflection. Above this angle the incident light is totally internal reflected at the interface between the prism and the S$_i$O$_2$ layer. The critical angle shifts to lower values as the wavelength decreases due to the frequency dispersion of the prism. At angles above the critical angle, a sharp dip in reflectance is observed around 60°. This dip corresponds to the excitation

of the fundamental TM_0 guided mode in the YAG:Ce layer, similarly to the TE_0 mode excitation in the QR layer discussed in the previous section. Since the transmittance through the sample vanishes above the critical angle and the YAG:Ce layer has a weak but finite absorption in the visible, a dip in reflectance is a result of an increase in absorption.

In Fig. 2.10(c) we show calculations based on the transfer matrix method of the specular reflectance for p-polarized light. The calculated structure consists of a fused silica substrate (infinitely thick, with a dispersionless refractive index $n = 1.46$), a YAG:Ce layer (200 nm thick, with a dispersive refractive index extracted from variable angle spectroscopic ellipsometry), an upper S_iO_2 layer (240 nm thick and with $n = 1.46$), and a prism (infinitely thick and with $n = 1.79$). A plane wave is incident through the prism with an angle of incidence θ and the intensity of the reflected light is calculated as a function of θ. The dispersion of the experimental dip in reflectance is in good agreement with the calculation.

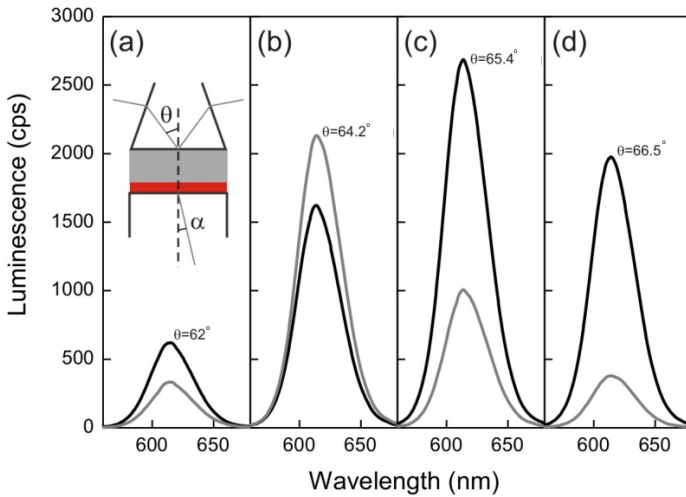**Figure 2.11:** Unpolarized photoluminescence spectra measured from the QR layer schematically represented in the inset. The QRs are excited using s-polarized (black curves) and p-polarized (gray curves) light of $\lambda = 457$ nm (1.6 mW) incident at (a) $\theta = 62°$, (b) $\theta = 64.2°$, (c) $\theta = 65.4°$ and (d) $\theta = 66.5°$. The collection angle (a) was fixed to 37° in all the experiments.

2.4 Photoluminescence

Coherent absorption can be exploited to enhance the photoluminescence from the light emitting layers. The inset of Fig. 2.11(a) shows a schematic representation of the experimental configuration used in the photoluminescence experiments. The angle of incidence θ is varied in these measurements, while the direction of detection, defined by the angle α between the normal to the layer and the detector, is kept fixed at 37° and 0° in the experiment with the QRs and YAG:Ce, respectively. The QR and the YAG:Ce layers were excited with a λ = 457 nm and λ = 488 nm laser, using both s- and p-polarizations. The emission was collected without polarization selection. From the measurements of Fig. 2.6(a), and fig. 2.10(b) we can conclude that the samples do not exhibit any strong resonant behavior at the emission wavelengths (both peaked around 600 nm). Therefore, the photoluminescence at these wavelengths follows a Lambertian curve as a function of the emission angle.
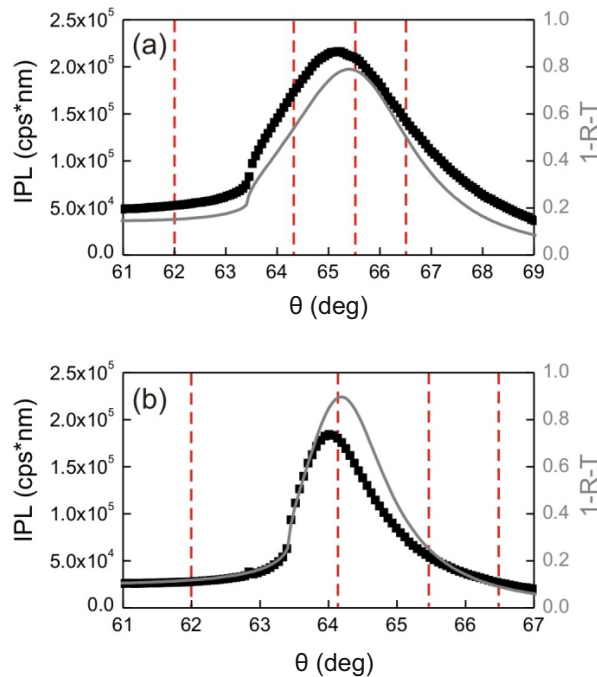

Figure 2.12: Measured photoluminescence intensity (black squares) and calculated absorptance (gray curves) of the QR layer schematically represented in Fig. 2.1(b), versus the angle of incidence of an (a) s-polarized and (b) p-polarized beam of λ = 457 nm. The vertical dashed lines indicate the angle of excitation of the photoluminescence spectra shown in Fig. 2.11.

2.4.1 Quantum dots in rods

In Fig. 2.11 are shown the spectra taken for different values of the angle of incidence and polarizations. Black curves correspond to *s*-polarized incidence and gray curves to *p*-polarized incidence. Figs. 2.11(a) shows the photoluminescence intensity for $\theta = 62°$, i.e., for an illumination angle below the critical angle. Figure 2.11(b) and (c) correspond to the angles of illumination at which maximum absorption at λ=457 nm is achieved in the QR layer for *p*- and *s*-polarization respectively, i.e., $\theta = 64.2°$ and $\theta = 65.4°$. An increased emission is achieved at the angles of incidence at which coherent absorption is observed. Figure 2.11(d) shows the photoluminescence emission due to evanescent excitation of the QR layer at $\theta = 66.5°$.

To directly correlate the absorptance to the photoluminescence enhancement, we have plotted in Figs. 2.12(a) and (b) the absorptance at $\lambda = 457$ nm (solid curves) and the photoluminescence intensity integrated from 550 nm to 670 nm (squares), as a function of the angle of incidence for *s*- and *p*- incident polarization, respectively. The dashed vertical lines correspond to the angles of Fig. 2.11(a-d). As expected, the enhancement of photoluminescence is directly related to the enhancement of the absorption at the excitation wavelength of the QRs. It is possible to evaluate an enhancement factor of the photoluminescence by dividing the value of the integrated intensity at the angle of maximum emission by the intensity at an angle lower than the angle of total internal reflection. Enhancement factors of 4.6 and 6.8 at $\lambda = 457$ nm are obtained for *s*- and *p*- polarization, respectively.

2.4.2 YAG:Ce

Figure 2.13 displays in a color map the emission spectra of the YAG:Ce layer as a function of the incident angle of the blue p-polarized laser ($\lambda = 488$ nm) through the prism. The
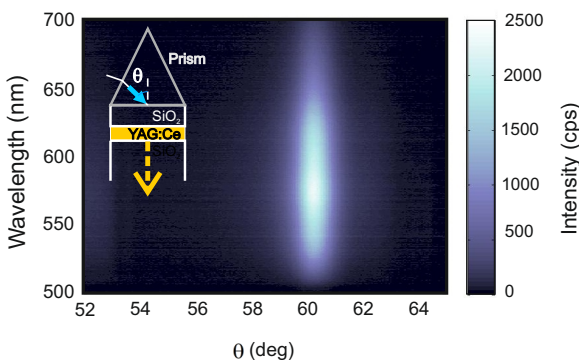

Figure 2.13: Emission spectra as a function of incident internal angle of the blue p-polarized laser ($\lambda = 488$ nm). The inset shows a sketch of the experimental setup. The incident angle is varied, while the emission is detected in the direction normal to the sample surface.

experimental configuration is illustrated in the inset of Fig. 2.13. A significant increase of the emission intensity is observed at the angle of incidence corresponding to the angle that shows a dip in reflectance [see Fig. 2.10]. The relation between reflectance and emission is further examined in Fig. 2.14. Figure 2.14(a) shows the reflectance as a function of θ at a wavelength of 488 nm, which corresponds to the wavelength of excitation in the photoluminescence measurement. With the increase of θ from 52°, which is below the critical angle for total internal reflection, the reflectance increases. At 60.3° the reflectance presents a local minimum due to the excitation of the TM_0 mode. In Fig. 2.14(b), the emission intensity, integrated from $\lambda = 500$ to 700 nm, is plotted as a function of θ. The emission intensity shows a maximum at θ that corresponds to the minimum in reflectance. The correspondence between the dips in reflectance and the peaks in the integrated emission intensity demonstrates that the enhanced emission is due to enhanced absorption. The minimum reflectance is as low as 0.56, meaning that the absorptance is 0.44 (no light is transmitted through the sample). The absorption length that corresponds to an absorptance of 0.44 at $\lambda = 488$ nm is 0.35 μm, as calculated considering the Lambert-Beer law. This value is far shorter than the value of 10 μm calculated from Fig. 2.5 for YAG:Ce, which means that by coupling the light into the waveguide modes, the absorption is effectively increased up to 30 times. We have also estimated the propagation length L_z of the guided modes along the YAG:Ce layer from the full width at half maximum of the reflection resonances shown in Figs. 2.10(b) [59]. The estimated value of L_z is ~10 μm at $\lambda = 488$ nm, which means that the coupled light propagates in the YAG:Ce layer over a distance of 10 μm before being absorbed and/or scattered to 1/e of its original intensity. This value of 10 μm agrees with the absorption length from the absorption spectrum presented in Fig. 2.5. Compared to the integrated intensity at $\theta = 53.4°$, which is below the critical angle, the integrated emission is enhanced by a factor of 30. The magnitude of the emission
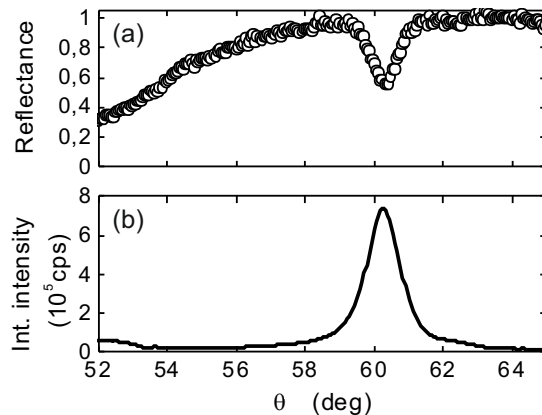

Figure 2.14: (a) Specular reflectance of a 200 nm thick layer of YAG:Ce at a wavelength of 488 nm for p-polarized light. (b) Integrated emission intensity between 500 and 700 nm as a function of incident angle of the p-polarized blue laser ($\lambda = 488$ nm).

intensity enhancement is on the same order of that of the absorption enhancement. These simple calculations of absorption and propagation lengths are consistent with the idea presented by Wan and coauthors to qualitatively describe the CPA [5]. Indeed, destructive interference in the far field confines the pump light in the absorbing layer and, in order to conserve its parallel momentum, also to propagate along the YAG:Ce layer.

Not only is the excitation blue light strongly influenced by the waveguide, but also the emission process. Indeed, the excited Ce^{3+} in the layer can emit either into guided modes or radiative modes with a branching ratio depending on the relative local density of states contributions. Using an exact formalism reported by Urbach and Rikken [60], we have calculated the total decay rate enhancement due to the waveguide, and the fraction of emission that is funneled into the waveguide modes, i.e., TM_0 mode, by considering a three-layer slab system consisting of 200 nm thick of YAG:Ce sandwiched by SiO_2 infinite layers. In Fig.2.15, the fraction of emission into waveguide modes is calculated as a function of the position of the emitter assuming that the Ce^{3+} presents an isotropic orientation. The YAG:Ce layer lies between z = -100 nm to 100 nm (indicated by the dashed lines). Inside the YAG:Ce layer, the coupling into the waveguide modes reaches a maximum value of 0.55 in the middle of the layer. This result is rather insensitive to the emission wavelength over the full range of emission in Fig. 2.13. This calculation indicates that roughly half of the emission stays inside the waveguide. The significant emission intensity enhancement reported in Fig. 2.14 can therefore be further enlarged by facilitating outcoupling of luminescence using a simple patterning of the surface. Since the absorption length of the emitted light and the excitation light are very different, an accurate design of the scattering strength of such texture will allow enhancing the outcoupling of the emission while maintaining the

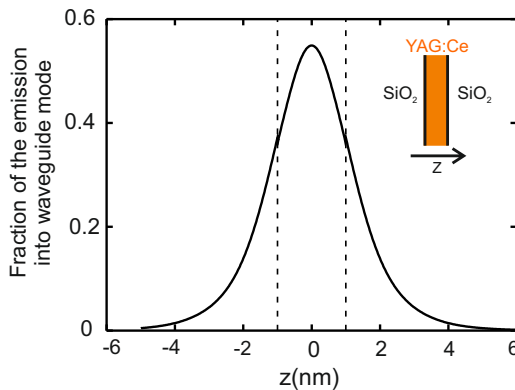**Figure 2.15:** Fraction of the emission ($\lambda = 580$ nm) that is funneled into the TM_0 waveguide mode as a function of the position of the emitter, averaged over all orientations of the emitter. The dashed lines indicate the position of the YAG:Ce layer. The inset shows a sketch of the three-layer system used in the calculation, which ignores the evanescently coupled prism but contains all layers of the sample.

high absorption of the excitation.

2.5   Conclusions

Enhanced optical absorption in very thin layers is relevant for applications in various fields such as lighting and sensitive photodetection. We have demonstrated experimentally an absorptance up to 80% for *s*-polarized light and 70% for *p*-polarized light at $\lambda = 457$ nm in a 23 nm-thick layer of quantum dots-in-rods. In a similar way, we have investigated also the enhanced absorption in a thin layer of YAG:Ce, obtaining an absorptance of 44% corresponding to an enhancement factor of 30. These extraordinary values are explained in terms of coherent absorption: the incident light is trapped in the layer due to the constructive interference of the fields scattered at different interfaces. The enhanced absorption is efficiently converted into photoluminescence from the QR and YAG:Ce layers. We have obtained up to a 7-fold enhancement of the QR emission for *p*-polarized incident light and a 30-fold emission enhancement for *s*-polarized incident light on the YAG:Ce layer, as a result of the coherent absorption in these layers. These enhancements can be further increased by optimizing the interference in the multilayer structure. The coherent absorption is also related to the critical coupling theory, which describes the efficient energy transfer between different media. The enhanced absorption can be associated also with the coupling of light into the fundamental guided mode supported by the layers. This analogy forces us to revisit the concept of "thickness" of the layer in which light is absorbed. For certain combinations of angles of incidence and wavelengths, the relevant dimension to understand absorption is not anymore the canonical thickness but it is the one along the surface of the layer.

CHAPTER 3

MODULATED LIGHT ABSORPTION AND EMISSION OF A LUMINESCENT LAYER BY PHASE-CONTROLLED MULTIPLE BEAMS

We propose a multiple illumination beam scheme to experimentally demonstrate the external control of the intensity of the light emitted by a thin layer of phosphor. This is realized through a tunable optical absorption of the incident light into the layer at a wavelength longer than the wavelength at which the absorption coefficient of the phosphor is maximum. The experiment is designed to get as close as possible to the condition of Coherent Perfect Absorption (CPA), realized by externally acting on the phase difference between the incident beams. When a destructive interference pattern is built outside the layer of luminescent material the incident light is efficiently absorbed.

3.1   Coherent Perfect Absorption (CPA)

The concept of Coherent Perfect Absorption (CPA) has been recently introduced by Chong and coauthors [5, 15]. CPA has been related to the time reversed process of lasing. In the lasing process, a cavity with gain produces outgoing optical fields with a definite frequency and phase relationship, without being illuminated by coherent incoming fields at that frequency. The laser is coupled to an energy source (the pump) that inverts the electron population of the gain medium, causing the onset of amplified spontaneous emission at a threshold value of the pump. Above threshold the laser is a nonlinear optical source, but at the threshold of the first lasing mode, the laser is described by the linear Maxwell equations with complex (amplifying) refractive index [61]. Because of the properties of these equations it follows that the same cavity, with the gain medium replaced by an equivalent absorbing medium, will perfectly absorb the same frequency of the laser light, if it is illuminated with incoming waves with the same field pattern of the laser light. The essence of the work of Chong and coauthors was the demonstration that the way a medium absorbs depends not only on its optical constants and the frequency of the incident radiation but also on the detailed spatial distribution of the incident fields. As a consequence, one can consider tuning the external field to either enhance or suppress absorption.

To determine the conditions for CPA in a medium of refractive index $\tilde{n} = n + i\kappa$ ($\kappa < 0$ for gain and $\kappa > 0$ for absorption) we consider the scalar wave equation

$$[\nabla^2 + \tilde{n}^2(\mathbf{r})k^2]\phi(\mathbf{r}) = 0, \tag{3.1}$$

where $k = \omega/c$, ω is the frequency, c is the speed of light, $\phi(\mathbf{r})$ is the electric field, $\mathbf{r}$ is the vector position. Outside the medium the refractive index is assumed to be a real constant, n_0 and the field is a combination of incoming waves ψ_m^{in} and outgoing waves ψ_m^{out}

$$\phi(\mathbf{r}) = \sum_m [\alpha_m \psi_m^{in}(\mathbf{r}) + \beta_m \psi_m^{out}(\mathbf{r})], \tag{3.2}$$

where α_m and β_m are the amplitudes of the incoming and outcoming waves, respectively, and m indicates the mode index. In essence the way to determine the CPA condition is to derive the relation between the frequency of the incident waves, their phases at the interface of the material, the refractive index and the relevant geometrical dimension of the object, such that the scattered field vanishes. The most convenient method to treat this problem is by introducing the scattering matrix of the system. Its advantage with respect to the transfer matrix method described in Appendix B, is that it separates the components of the incoming fields from the components of the outgoing ones, i.e., the scattering matrix, S, relates the incoming with the outgoing amplitudes

$$\sum_{m'} S_{mm'}(k)\alpha_{m'} = \beta_m. \tag{3.3}$$

The eigenvectors of the scattering matrix associated with infinite eigenvalues and with real k, describe the condition for lasing at threshold [16]. These eigenvectors are given by

$$\beta_m = \pm\infty\alpha_m. \tag{3.4}$$

The condition $k \in \mathbb{R}$ guarantees that the mode is radiative. By time-reversal, if it exists an eigenmode with k real and 0 eigenvalue, CPA is realized, i.e.

$$\beta_m = 0\alpha_m. \tag{3.5}$$

The scattering matrix is in general difficult to determine analytically. Nevertheless, there are certain geometries that because of their simplicity and symmetries allow us to write explicitly its elements. Let us consider the case of a slab of weakly absorbing material, described by a complex refractive index $\tilde{n}$, illuminated by two collinear and counterpropagating beams impinging at normal incidence and embedded in a uniform environment described by the refractive index n_0. The system is sketched in Fig. 3.1, where blue arrows represent the incident waves and the red arrows represent the scattered ones. The incoming and outgoing fields are written as

$$
\begin{aligned}
\psi^{in}(t,\mathbf{r}) &= \alpha_1 \psi_1^{in}(t,\mathbf{r}) + \alpha_2 \psi_2^{in}(t,\mathbf{r}), &\tag{3.6}\\
\psi^{out}(t,\mathbf{r}) &= \beta_1 \psi_1^{out}(t,\mathbf{r}) + \beta_2 \psi_2^{out}(t,\mathbf{r}), &\tag{3.7}
\end{aligned}
$$

where α_m and β_m are the amplitudes of the propagating modes $\psi_m^{in/out}$ and $m = 1,2$ represents the mode index. $\psi_m^{in/out}$ can be generally approximated by plane waves. The scattering matrix of the system, S, relates the amplitudes $\alpha_{1,2}$ of the incoming field with the amplitudes $\beta_{1,2}$ of the outgoing fields

$$\begin{pmatrix} \beta_2 \\ \beta_1 \end{pmatrix} = S \begin{pmatrix} \alpha_1 \\ \alpha_2 \end{pmatrix} = \begin{pmatrix} S_{11} & S_{12} \\ S_{21} & S_{22} \end{pmatrix} \begin{pmatrix} \alpha_1 \\ \alpha_2 \end{pmatrix}. \tag{3.8}$$

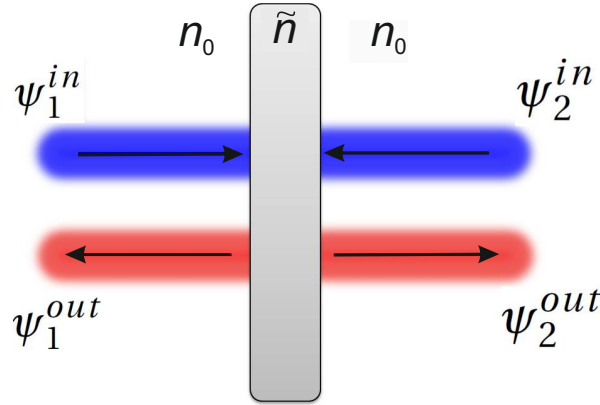**Figure 3.1:** Sketch of a slab of weakly absorbing material, described by a complex refractive index $\tilde{n}$ illuminated by two collinear and counterpropagating beams impinging at normal incidence (blue arrows) and embedded in a uniform environment described by the refractive index n_0. The incident and the scattered waves (red arrows) are described by $\psi_{1,2}^{in,out}$, respectively.

In this case S is a 2x2 matrix because there are two incoming and 2 outgoing beams, also termed as channels [15]. Since the system is symmetric with respect to the plane where the slab lyes $S_{12} = S_{21}$ and $S_{11} = S_{22}$. The elements S_{12} and S_{21} are the reflection coefficients, while S_{11} and S_{22} are the transmission coefficients. Since the system consists of planar and parallel interfaces, these coefficients correspond to the Fresnel reflection and transmission coefficients, r and t, respectively. CPA is realized when the amplitudes of the outgoing fields are zero

$$\begin{pmatrix} 0 \\ 0 \end{pmatrix} = S \begin{pmatrix} \alpha_1 \\ \alpha_2 \end{pmatrix}, \tag{3.9}$$

i.e.,

$$S \begin{pmatrix} \alpha_1 \\ \alpha_2 \end{pmatrix} = 0 \begin{pmatrix} \alpha_1 \\ \alpha_2 \end{pmatrix}. \tag{3.10}$$

Therefore the incident field has to be an eigenvector of the scattering matrix with eigenvalue 0. For the case of a slab in homogeneous environment the eigenvalues of S are $\lambda_{1,2} = S_{11} \pm S_{12} = t \pm r$ [57]. If the slab is embedded in air, the CPA condition can be written as

$$\lambda_{1,2} = t \pm r = 0 \longrightarrow \frac{\left[1 - \left(\frac{\tilde{n}-1}{\tilde{n}+1}\right)^2\right] e^{-ikd\tilde{n}}}{1 - \left(\frac{\tilde{n}-1}{\tilde{n}+1}\right)^2 e^{-2ikd\tilde{n}}} \pm \frac{\left(\frac{\tilde{n}-1}{\tilde{n}+1}\right) \left[e^{-2ikd\tilde{n}} - 1\right]}{1 - \left(\frac{\tilde{n}-1}{\tilde{n}+1}\right)^2 e^{-2ikd\tilde{n}}} = 0. \tag{3.11}$$

This leads to the equation

$$e^{ikd\tilde{n}} = \pm \frac{\tilde{n}-1}{\tilde{n}+1}. \tag{3.12}$$

The eigenvectors corresponding to these two eigenvalues are $(\alpha, \pm\alpha)$ where the plus and the minus sign describe the symmetric and the antisymmetric mode, respectively, and $\alpha = \alpha_1 = \alpha_2$ is a consequence of the mirror symmetry of the system. By substituting Eq. (3.12) into the definitions of r and t we can evaluate the reflection and the transmission coefficients when CPA is realized [62], namely,

$$r = -\frac{1}{2} \frac{\tilde{n}^2 - 1}{\tilde{n}^2 + 1} \qquad t = \pm \frac{1}{2} \frac{\tilde{n}^2 - 1}{\tilde{n}^2 + 1}, \tag{3.13}$$

which makes evident that the transmission of one wave cancels out exactly the reflection of the second wave, resulting in total absorption in the slab.

3.1.1   Example of CPA

If the input channels are eigenvectors of S, the intensity of the field scattered off a slab is given by the square of the absolute value of the eigenvalue of the scattering matrix, $|\lambda_{1,2}|^2$ and it depends on the thickness of the slab, the wavelength of the incident light, and the refractive index of the slab and of the environment [15]. With the definitions of the eigenvalues given in Eq. (3.11) we can calculate the intensity of the scattered field as a function of these quantities for the symmetric and antisymmetric mode. As an example, we consider a 1μm-thick slab embedded in air and illuminated with a wavelength of 450

nm. Figure 3.2 shows in logarithmic scale $|\lambda_{1,2}|^2$ as a function of the real and imaginary component of the refractive index of the slab. There are discrete regions in the plot
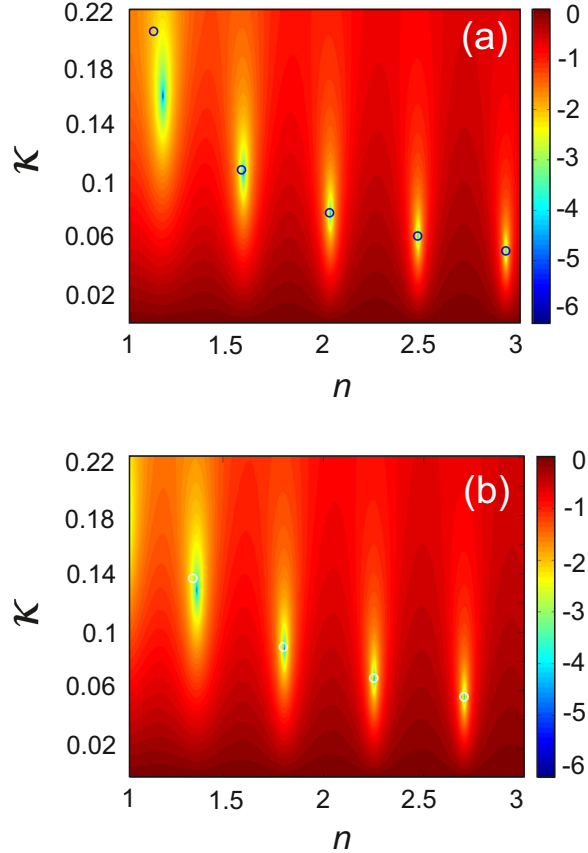
Figure 3.2: Logarithm of the normalized intensity of the scattered field for the (a) antisymmetric and (b) symmetric CPA as a function of the real and imaginary component of the refractive of a 1μm-thick slab embedded in air and illuminated at normal incidence by two counter-proapgating beams of wavelength of 450 nm. Symbols correspond to the approximated solution given by Eq. (3.15)

in which the intensity is dramatically reduced. We can qualitatively understand the distribution of these regions in the plot by considering that the closer the real part of the refractive index of the slab is to 1, the lower is the refractive index contrast with the surrounding (air) and the larger will be the difference between the amplitudes of the transmitted and reflected partial waves. Therefore, to compensate for this mismatch and achieve CPA, the imaginary component of the refractive index has to increase. CPA is realized for the values of $\bar{n}$ at which the intensity of the scattered waves vanishes, thus at the minima of Fig. 3.2.
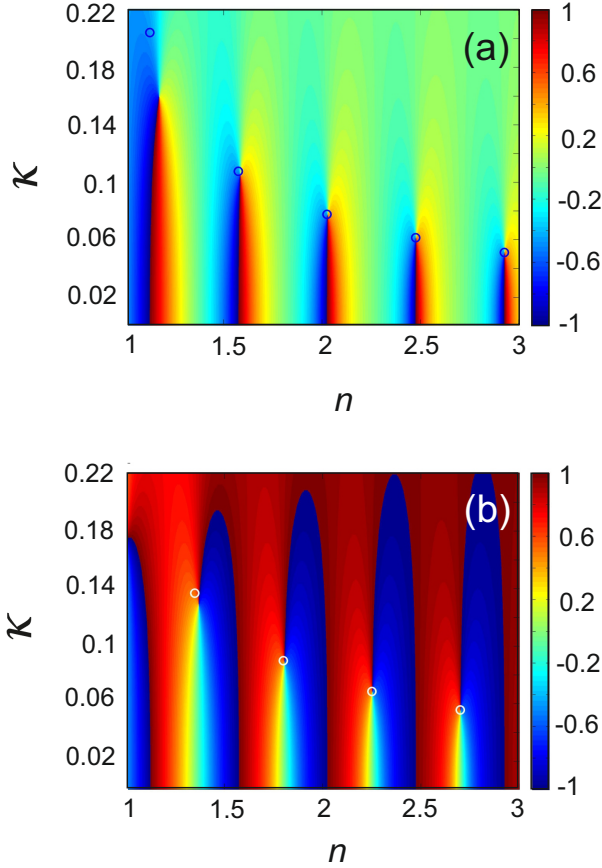
Figure 3.3: Phase in units of π of the scattered field for the (a) antisymmetric and (b) symmetric CPA as a function of the real and imaginary component of the refractive of a 1μm-thick slab embedded in air and illuminated at normal incidence by two counter-proapgating beams of wavelength of 450 nm. Symbols correspond to the approximated solution of Eq. (3.12)

To verify that for these specific combinations of real and imaginary components of the refractive index of the slab the intensity of the scattered field is exactly zero, in Fig. 3.3 we plot the phase of $\lambda_{1,2}$. In correspondence with the the locations of the minima of Fig. 3.2, we find a singularity of the phase, which indicates the complete vanishing of the scattered fields.

As we see from Eq. (3.12) the CPA condition depends on the ratio between the thickness of the slab and the wavelength of illumination. Let us consider one of the CPA points of Fig 3.2(b), for example the one given by $\tilde{n}=2.25+i0.068$. For this point we plot in Fig. 3.4 the intensity of the scattered field as a function of the thickness of the slab for the wavelength of illumination of 450 nm. As expected, we find a pronounced dip for the thickness of 1
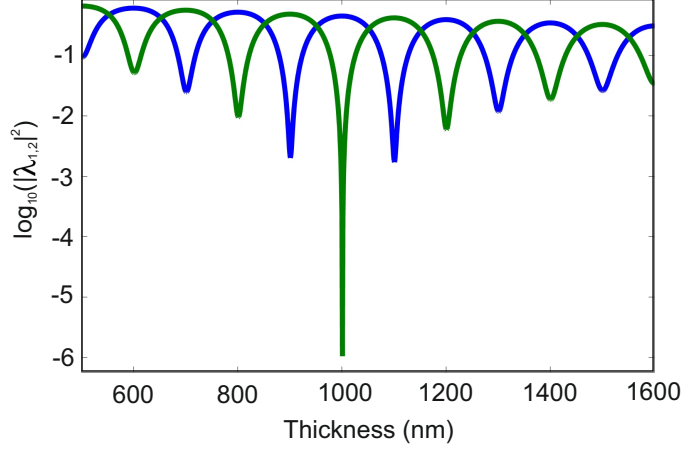
Figure 3.4: Logarithm of the normalized intensity of the scattered field as a function of the thickness of the slab for the refractive index $\bar{n}$=2.25+i0.068 and for the wavelength of illumination of 450 nm. The slab is embedded in air and the angle of incidence of the waves is 0. The green line corresponds to the symmetric modes, the violet line to the antisymmetric modes.

μm, which corresponds to the CPA condition previously found in Fig. 3.2. We notice that a difference of only 10 nm in the thickness of the slab, i.e., less than an order of magnitude of the incident wavelength, gives a difference in the intensity of the scattered field of 4 orders of magnitudes in CPA condition. This pronounced sharpness of the resonance represents a major limitation to achieve experimentally CPA and it will be further discussed in the next sections.

The CPA equations have an approximated solution which is useful in the case of $kd >> 1$, i.e., for very thick slabs compared to the incident wavelength and in the case of very weakly absorbing materials ($\kappa << n$). Indeed, if $\kappa << n$ we can neglect κ in the right term of Eq. (3.12) obtaining [15]

$$\begin{cases} e^{ikdn} \approx e^{iZ\pi}, & Z \in \mathbb{Z} \\ e^{-kd\kappa} \approx \frac{n-1}{n+1} \end{cases}$$ (3.14)

which gives

$$\begin{cases} n \approx \frac{Z\pi}{kd}, & Z \in \mathbb{Z} \\ \kappa \approx \frac{1}{kd} \ln\left[\frac{n+1}{n-1}\right] \end{cases}$$ (3.15)

Odd and even Z correspond to antisymmetric and symmetric CPA points, respectively. These approximated solution are plotted with open symbols in Figs. 3.2 and 3.3. White circles correspond to the symmetric mode while blue circles correspond to the antisymmetric mode. We see that the approximated solution describes well the system only for $\kappa > 0.1$, i.e., $n/\kappa > 20$.

3.1.2 Field distribution in CPA condition

Now that we know the values of complex refractive index of the slab, thickness and wavelength realizing the conditions for CPA in the 3-layer system, it is possible to calculate the spatial distribution of the electric field. This calculation is carried out by making use of the transfer matrix method described in Appendix B for each of the incident waves and the superposition principle. The electric field associated with the propagation of a single wave in the $x - z$ plane,is given by

$$
\begin{cases}
E(x,z,t) = \left[a_1 e^{-ik_x x} + a_2 e^{ik_x x} \right] e^{-ik_z z} e^{-i\omega t}, & x \in \text{substrate} \\
E(x,z,t) = \left[b_1 e^{-ik_x x} + b_2 e^{ik_x x} \right] e^{-ik_z z} e^{-i\omega t}, & x \in \text{slab} \\
E(x,z,t) = c_1 e^{-ik_x x} e^{-ik_z z} e^{-i\omega t}, & x \in \text{superstrate}
\end{cases}
\tag{3.16}
$$

where the axis normal to the slab is along z and the amplitudes of the partial fields, $a_{1,2}$, $b_{1,2}$ and $c_{1,2}$ are calculated with the transfer matrix method (see Appendix B). k_x and k_z are the $x-$ and z-component of the wavevector, ω is the angular frequency and t is the time. The total electric field is obtained by adding the complex values of the electric field for the two incident waves at each position (x,z) of the structure. Figure 3.5(a) shows in color scale the spatial distribution of the total electric field for illumination through the symmetric CPA eigenmode at normal incidence, i.e., $k_z = 0$. The dashed horizontal lines mark the boundaries of the slab. The field amplitude of this total electric field along the x-coordinate is shown in Fig. 3.5(b) with a red curve. In the same panel we also show the amplitude of the incident, reflected, transmitted and scattered field. These fields are all defined for $x < 0$ and $x > 1$ μm. The blue curve represents the incident field. The cyan curve and the black curve represent the reflected and the transmitted fields, respectively. The sum of these two fields gives rise to the scattered field. Since we are applying the superposition principle, all these calculations are phase sensitive. Panel (a) and (b) show the calculations for the phase $\omega t = 0$, which means that the two waves have the same phase when impinging on the slab. Panel (c) and (d) show the same calculations but for $\omega t = 1.5\pi$. We see that at each phase ωt the total electric field overlaps exactly with the incident field, meaning that the scattered field is zero and all the energy is absorbed by the slab. Indeed the co-propagating reflected and transmitted waves have the same amplitudes and are in antiphase for each ωt.

The simple expression for the CPA equation, Eq. (3.12) and its approximated solution Eq. (3.15), are valid only in the case of a slab embedded in a symmetric environment and illuminated at normal incidence. However, since the elements of the scattering matrix of a generic 3-layer system are known analytically, it is straightforward to calculate the CPA conditions also in the case that the weakly absorbing material is deposited on a substrate and illuminated at a certain angle θ_1. In Fig. 3.6 we plot in logarithmic scale the absolute values of the eigenvalues of the scattering matrix, $|\lambda_{1,2}|^2$, i.e. the intensities of the field scattered off a slab, as a function of the thickness in the case of a layer with refractive index $\tilde{n}$=2.25+i0.068, deposited on a substrate with refractive index $n_0 = 1.4$ and illuminated by two non-collinear s-polarized waves. In Fig. 3.6 we set $\theta_1 = 20°$ for the wave propagating from the air-side (see inset). The two incident waves has to be non-collinear in order
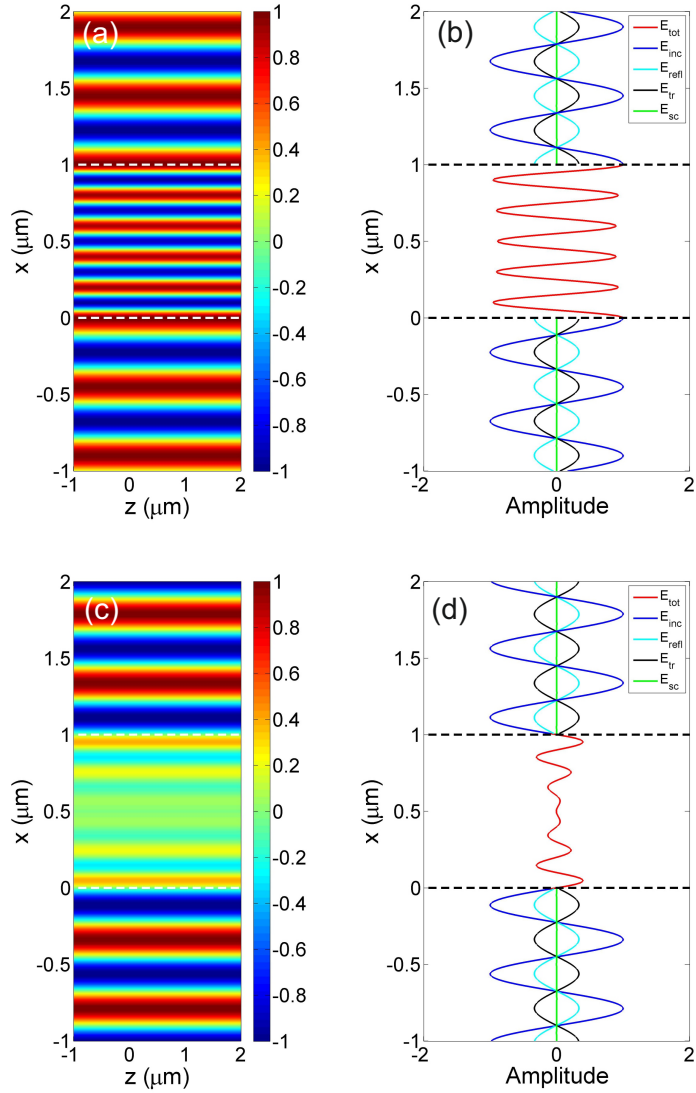
Figure 3.5: Spatial distribution of the total electric field and cuts along the *x*-coordinate of the total electric field (red line), of the incident field (blue line), of the reflected (cyan line) and transmitted (black line) fields giving rise to the scattered field (green line). The structure consists of a slab of refractive index *n*=2.25+i0.068 embedded in air and illuminated with the symmetric CPA eigenmode. All these quantities are calculated for the phase ωt of the two waves at the two interfaces of the slab (marked by dotted lines) equal to 0 [(a) and (b)] and equal to 1.5π [(c) and (d)]

for the transmitted and reflected waves to propagate collinearly and cancel out exactly. The angle of incidence of the wave propagating from the substrate-side (θ_2) has to match the angle of transmission of the first wave, which is given by Snell's law. As expected, the general trend of the intensity of the scattered field for the symmetric and antisymmetric modes as a function of the thickness is similar to the one in Fig. 3.4 but the thickness at which CPA occurs is different. Indeed, since the mismatch between r and t increases with the angle of incidence, the optimal thickness that allows the scattered field to vanish has to change.

In the following sections we investigate the implications that CPA has when applied to a slab of luminescent material of reference for solid state lighting applications.
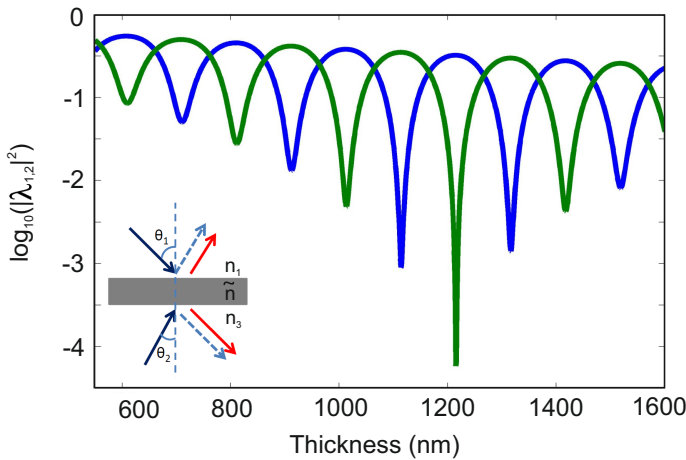
Figure 3.6: Logarithm of the intensity of the scattered field as a function of the thickness of the slab with refractive index $\tilde{n}$=2.25+i0.068 and for the wavelength of illumination of 450 nm. The slab is deposited on a substrate (n_3=1.4) and illuminated at angle θ_1=20° from a air (n_1=1). θ_2 is given by Snell's law. The green line corresponds to the symmetric modes, the violet line to the antisymmetric modes. Inset: schematic representation of the system. Incident waves are represetned by blue arrows, reflected waves by dashed light blue arrows and transmitted waves by red arrows.

3.2 CPA in luminescent materials

Coherent phenomena have been intensively studied in optics with the prospect of exploiting interference and resonant effects. In particular, the coherent control of light absorption has recently attracted considerable interest due to the possibility of building complex interference patters in and outside the structure under investigation, with the aim of modulating, enhancing or suppressing its optical response [15, 26–28]. Different methods have been introduced to achieve this, such as wavefront shaping [19–21, 23, 63] and multiple beam illumination schemes [24, 25, 29]. So far, research has focused only

on the coherent processes related to the absorption of light, without considering or even excluding the possibility of using light converting materials [15] and without addressing any efficiency related problem. Specifically, any down-conversion process is associated with a loss of energy determined by the characteristic Stokes' shift of the luminescent material, which is defined as the difference in energy between the maximum of the absorption spectrum and the maximum of the emission spectrum. This loss is generally considered unavoidable in conversion processes. The definition of the Stokes' shift is solely related to the material, and does not take into account the role played by the geometry of the light-converting material and by the illumination conditions. However, as pointed out in the previous section, the optical absorption depends not only on the optical constants of the material but also on the spatial distribution of the radiation. There can be conditions at which a precisely designed illumination of the luminescent weakly absorbing material gives a very high absorption. The unique set of conditions at which all the incident light is absorbed is provided by the CPA, which in the case of a luminescent material corresponds to placing the emitters in a perfect cavity. Exploiting cavity resonances to enhance the absorptance of emitters is a well-known technique, but if the cavity and the illumination are not tuned to achieve CPA, it is impossible to achieve total absorption.

A subtle point increases the interest and novelty of systems tuned to their CPA condition: Coherent Perfect Absorbers are open systems, i.e., energy can flow efficiently inward and outward the system. This opposes to a classical cavity experiment, in which, because of reciprocity, if light is easily coupled into the cavity, it is also easily coupled out, preventing high absorption. This is typically described by the Q-factor of the cavity: a high Q indicates a low rate of energy loss (by outcoupling) relative to the energy stored in the resonator. A high Q-factor cavity is therefore realized by using very good reflecting mirrors, which again makes it difficult to supply energy from outside into the cavity. On the contrary, a CPA cavity does not require a high Q-factor because light is trapped by the interference of the multiple incident beams. If the wavelength at which CPA takes place (λ_{CPA}) is longer than the wavelength at which the absorption coefficient of the material is maximum, the Stokes' shift needs to be redefined. In this case the Stokes' shift is given by the energy difference between the CPA frequency and the frequency of maximum emission.

In the next sections we theoretically demonstrate CPA as a mean to redefine the Stokes' shift. (see Fig. 3.1). We experimentally demonstrate that by properly setting the phase difference between the two beams the incident light is trapped in the luminescent layer, absorbed and converted into photoluminescence (PL). In this way it is possible to increase and modulate the emission from the luminescent layer. Since the quantum efficiency of luminescent materials is typically close to 1, CPA allows, at least in principle, obtaining full conversion of the pump light while maintaining the thickness of the layer small. However, this point is subject to experimental limitations and difficulties, which limit the realization of the CPA experiment with a material of fundamental importance for solid state lighting, such as YAG:Ce.

3.3 Sample characterization

In Chapter 2 we have introduced Ce^{3+} doped yttrium aluminum garnet, $Y_3Al_5O_{12}$ (YAG:Ce) as an important luminescent material for lighting applications because of its superb luminescent properties, chemical durability, and thermal stability. YAG:Ce has an absorption peak around 460 nm while its emission spectrum spans the range 500-750 nm (the broadest known emission spectrum). Due to this characteristic spectra, YAG:Ce is found in applications such as white light emitting diodes (LEDs) [40] and full down-conversion based devices(high-color-purity light, especially in the so-called "yellow gap" [64]).

The sample we have investigated is a 100 μm-thick layer of polycrystalline lumiramic YAG:Ce doped at 3.3% with Ce^+ ions and polished via a chemical-mechanical procedure on both sides. YAG:Ce has been produced following the procedure described in Refs. [65–67]. In order to reach the CPA conditions we need to fulfil three conditions on the quality of the layer: 1) the surface of the sample has to be optically flat; 2) the thickness of the slab has to be uniform over the dimension of the illumination spot; 3) there have to be
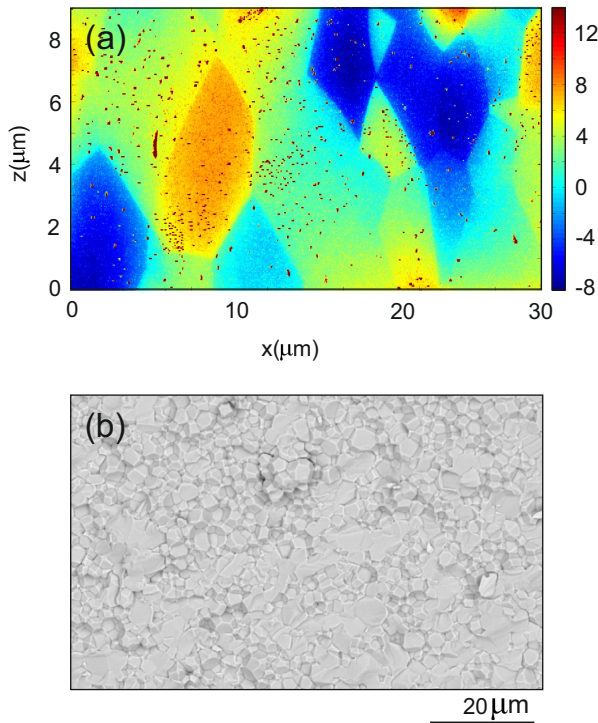

Figure 3.7: (a) 2D AFM scan of the surface of the YAG:Ce slab after polishing. The colorscale is in units of nanometers. (b) SEM image of the cross section of the YAG:Ce slab.

no scattering centers for the light throughout the slab. These three conditions ensure that the phase relation imposed at the interfaces of the slab is maintained throughout the sample. In Fig. 3.7(a) we show a 2D AFM image of the surface of the slab after the polishing procedure. The surface roughness is on the order of 10 nm, which makes the surface optically flat. In the previous sections we have argued that a uniform thickness of the slab 10 nm off respect to the thickness for CPA, leads to a strong decrease in the absorption. However, this uniform offset of the thickness should not be confused with a distribution of thicknesses given by a surface roughness. Indeed, in the case of surface roughness the value of absorption and its modulation are given by the average over the distribution of the thicknesses. For a surface roughness of 10 nm, as the one shown in Fig. 3.7(a), this average results in a very small difference with the CPA case. The regular geometrical structures visible are the edges of the crystals of the YAG:Ce emerging because of the slightly different polishing rates along the direction of the crystals. The dimensions of the crystals are around 5 μm. Figure 3.7(b) shows a SEM image of the cross section of the sample taken after breaking the sample into two parts. There are no inclusions, holes or imperfections that can be attributed to the fabrication and no formation of second
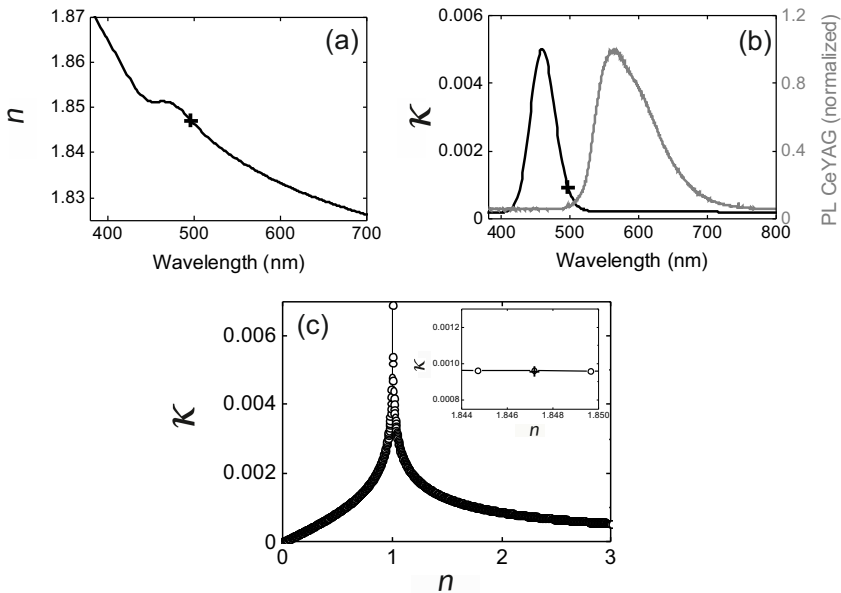
Figure 3.8: Black curves represent the real (a) and the imaginary (b) component of the refractive index of the YAG:Ce slab as a function of the wavelength. Grey line in (b) represents the normalized emission spectrum from the YAG:Ce. Crosses: value of the refractive index of the YAG:Ce at 496 nm. (c) shows the approximated solution of Eq. (3.12) for an ideal 100μm-thick slab illuminated at the wavelength of 495.9 nm. The inset is a zoom around the value of the complex refractive index of the YAG:Ce at this wavelength, which is indicated by the cross.

phase material, which might have a different refractive index. The only structures present are again the edges of the crystals. Therefore the refractive index of the material is uniform along the slab.

To reach the desired thickness and surface quality on both faces of the slab, we first grinded the row material mechanically with a rotating wheel and then we refined the quality with the combination of mechanical motion of the wheel and chemical etchers. The plane-parallelity of the surfaces was controlled by making use of several others samples of the same material that were polished simultaneously with the final sample and that avoided the off-axis motion of the polishing wheel. The thickness of the sample has been measured with a Heidenhain VRZ thickness gauge device. This procedure gave us an accuracy on the measurement of the uniformity of the thickness of ± 200 nm. This uncertainty in thickness is the main limitation that we have to take into account when interpreting the results.
The complex refractive index of the sample has been measured by ellipsometry. Black curves in Figs. 3.8(a) and (b) represent its real and imaginary components of the refractive index as a function of the wavelength, respectively. The maximum of the absorption is found at $\lambda_{max} = 460$ nm. The grey line in panel (b) represents the normalized emission spectrum from the YAG:Ce layer.

3.4 Redefinition of the Stokes' shift

As explained in section 3.1, if the complex refractive index and the thickness of the YAG:Ce slab are known, it is possible to calculate the wavelength at which the CPA condition is fulfilled. Since the imaginary component of the refractive index of the YAG:Ce is on the order of 10^{-3}, we can use the approximated solution given by Eq. (3.15). Figure 3.8(c) shows the result of this calculation when an ideal 100 μm-thick slab is illuminated by the

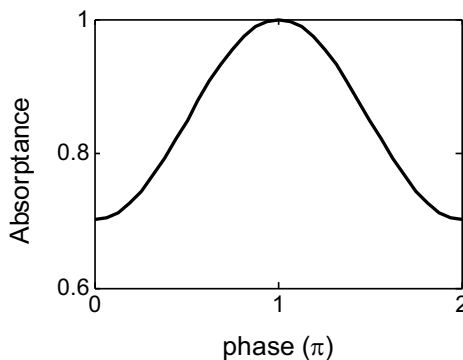**Figure 3.9:** Absorptance of a 100 μm-thick slab of YAG:Ce illuminated with the configuration shown in Fig. 3.1 with a wavelength of 495.9 nm, as a function of the phase difference between the two incident waves.
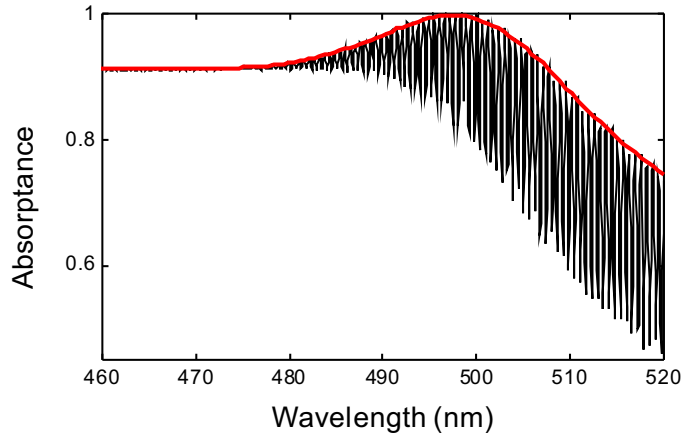
Figure 3.10: The black curve represents the maximum absorptance at each wavelength impinging on a 100 μm-thick slab of YAG:Ce illuminated at normal incidence by two counterproapgating and collinear beams.

wavelength of $\lambda_{\mathrm{CPA}} = 495.9$ nm. The inset is a zoom around the value of the complex refractive index of the YAG:Ce at this wavelength which is indicated by the black cross. We see that for this combination of parameters perfect absorption is achieved in the configuration schematically shown in Fig. 3.1. The crosses in panels (a) and (b) mark the value of the refractive index of the YAG:Ce at $\lambda_{\mathrm{CPA}} = 495.9$ nm. By knowing the complex refractive index of the slab and assuming a uniform thickness of 100 μm, we can calculate the absorptance as a function of the phase difference between the two incident waves. The phase is set at the first interface encountered by each incident wave. This calculation is performed in a similar way as that used to obtain the total electric field in Fig. 3.5. For each phase and for each incident wave we make use of the transfer matrix method described in Appendix B. Then we use the superposition principle to find the value of the total electric field in the slab. The absorptance is evaluated according to Eq.(1.4) and the result is plotted in Fig. 3.9, where we see that the absorptance depends on the relative phase between the two incident waves and it reaches 100% when the two waves are in antiphase, meaning that this absorption is caused by the antisymmetric CPA solution. Remarkably, we notice that $\lambda_{\mathrm{CPA}} > \lambda_{\mathrm{max}}$, i.e., perfect absorption is achieved at a wavelength longer than the wavelength of maximum absorption given by the optical constants of the material.

To demonstrate a modification of the Stokes' shift we first repeat the calculation in Fig. 3.9 for a broad range of wavelengths, then for each wavelength we extract the maximum value of absorptance. The result is shown in Fig. 3.10 with the black curve. We see a very fast oscillation of the absorptance, which is given by the combination of the two Fabry-Perot resonances associated with the two beams interfering in the slab. The contrast of the oscillations is reduced as the wavelength approaches λ_{max} because the transmittance
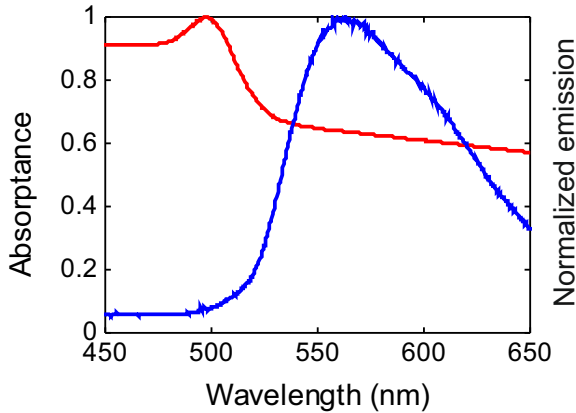
Figure 3.11: The red curve is the envelope of the black curve in Fig. 3.10. The blue curve represents the typical emission spectrum of YAG:Ce.

of the single wave through the slab is almost zero due to the absorption and no effective interference between the two waves occurs. Therefore the maximum absorption is limited by the reflectance at the first interface. Instead absorptance equals 1 at λ_{CPA}, as expected. The red curve is the envelope of the black curve. This envelope is plotted on a larger wavelength range in Fig. 3.11, together with the typical emission spectrum of the YAG:Ce (blue curve). By comparing the maximum of the envelope with the maximum of the emission spectrum, we can state that the Stokes' shift is reduced by 35% as a result of the CPA.

3.5   Experimental results and analysis

The results shown in Figs. 3.9 and 3.10 are valid only for an ideal slab. The approximated solutions plotted in Fig. 3.8(c) do not tell anything on the sensitivity of the system to variations in the parameters of Eq. (3.12). Experimentally, the parameter that could differ the most over the size of the illumination beam is the thickness of the layer. In Fig. 3.12 we show in logarithmic scale the intensity of the scattered field, evaluated as the square of the absolute value of the two eigenvalues of the scattering matrix of the system we are studying. These two eigenvalues correspond to (a) antisymmetric and (b) symmetric CPA resonances. The calculation is performed as a function of the thickness of the slab and of the wavelength of illumination. The bands of minimum intensity correspond to the CPA conditions. These bands are continuous because λ and d appear as a ratio in the dimensionless parameter kd in the exponent of the CPA equation [Eq. (3.12)]. This dependence is helpful because it potentially allows to continuously tune one of the two parameters in order to compensate for a variation of the other. Nevertheless, we also see that these bands are very narrow both in wavelength and in thickness. The sharpness of
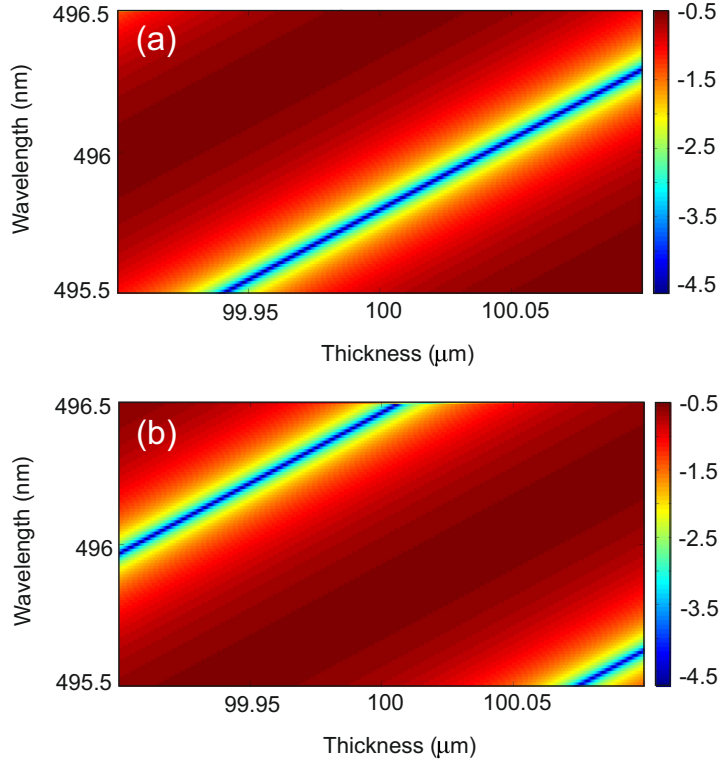
Figure 3.12: Intensity of the field scattered off a YAG:Ce slab illuminated at normal incidence by two counter-propagating beams, as a function of the wavelength of illumination and thickness of the slab. (a) antisymmetric and (b) symmetric CPA resonance.

the CPA resonance along the wavelength axis can be easily addressed by using as a source a gas laser which provides emission from an atomic transition and therefore it is much sharper than the linewidth of the CPA resonance. The system has been designed to show a CPA resonance at the wavelength of emission of an Ar-Kr laser, namely, $\lambda_{CPA} = 495.9$ nm. With regard to the thickness, we have an experimental uncertainty on its value of $\pm$ 200 nm. This means that in the experiment the absorptance averages over the different values assumed by the thickness, which leads to a non-zero scattered field and a non-perfect absorption.

Figure 3.13 displays the set-up that we have used to demonstrate the coherent control on the intensity of the emitted light. A beam splitter divides the laser beam into two beams of equal intensity indicated with (1) and (2) in the figure. Beam (1) is phase delayed with respect to beam (2) through a computer-controlled piezo electrical actuator with a nanometer precise motion. The two beams impinge normally on the YAG:Ce layer and get partially reflected and partially transmitted at the two interfaces. The transmitted
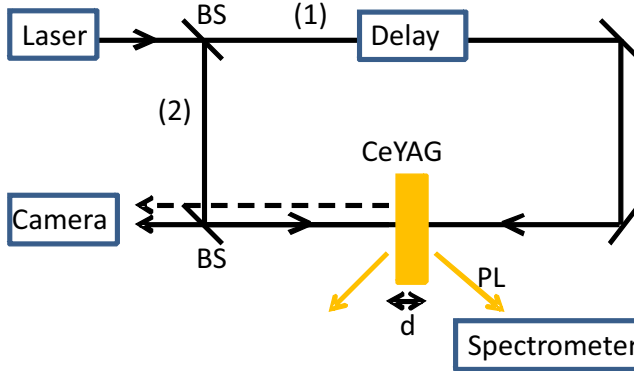
Figure 3.13: Schematic representation of the experimental set-up. A beam from a tunable continuous-wave Ar-Kr laser is splitted by the beam splitters (BS). The two beams (1) and (2) impinge normally to the sample, a YAG:Ce slab of thickness d. Beam (1) travels through a delay stage (mirror mounted on a computer-controlled piezo electrical stage) which controls the relative phase between the two beams. The scattered intensity from the left side, consisting of the interference between the backreflection of the beam (2) (continuous line) and of the transmission of beam (1) (dashed line) through the sample, is detected by a camera. The photoluminescence spectrum (PL) is measured by a spectrometer.

fraction of the beam (1) interferes with the reflected part of the beam (2) and the result of this is monitored by a camera. The absorbed light is converted by the YAG:Ce layer into photoluminescence, which is detected by a spectrometer placed at a fixed angle (30°) respect to the normal to the sample interface. The piezo electric mirror allows the control of the relative phase, ϕ, between the two incident beams [15]. This correspond to swap from the symmetric to the antisymmetric mode, therefore to modulate the absorption from a higher to a lower value. Since the absorbed power is efficiently converted into photoluminescence (PL) by the YAG:Ce, we expect that PL and absorption have the same amplitude modulation, which can be evaluated as

$$M = \frac{A(\lambda_{\mathrm{CPA}}, \phi = 0) - A(\lambda_{\mathrm{CPA}}, \phi = \pi)}{[A(\lambda_{\mathrm{CPA}}, \phi = 0) + A(\lambda_{\mathrm{CPA}}, \phi = \pi)]/2}, \tag{3.17}$$

where A is the absorptance. For the ideal slab with a thickness of 100 μm-thick, $M = 35\%$ (see Fig. 3.9).

We measure the PL spectrum of the YAG:Ce layer for each phase difference between the two incident beams ranging from π to 5π using the configuration shown in Fig. 3.13. Black circles in Fig. 3.14(a) represent the measurement of the modulation of the PL as a function of ϕ. The wavelength of the laser used to pump the YAG:Ce is λ_{CPA}. Each black circle corresponds to the maximum of the PL spectrum. The measurement follows a cosine square function which is the typical result of interference of plane waves. The grey dashed line indicates the sum of the maxima of the PL when the two beams impinge separately on the sample. This correspond to the incoherent sum of the two beams. We reach an experimental modulation of the PL equal to 2.3%. Simultaneously to the measurement of the spectra, the total scattering intensity from the left side has been recorded with a CCD

camera. These measurements are shown in Fig. 3.14(b) where each point is the result of the average over the full width at half maximum of the intensity of each beam spot in the camera. This total scattering is the result of the interference between the transmitted part of beam (1) and the reflected part of beam (2). It is therefore expected to be in antiphase with respect to the PL modulation: when the interference pattern built outside the layer is destructive (minima in Fig. 3.14(b)), the energy is trapped into the layer and converted into PL (maxima in the PL modulation in Fig. 3.14(a)). Figs. 3.14(e) and (f) display two images of the beam spot corresponding to the left-scattered intensity recorded by the camera for $\phi = 2\pi$ and for $\phi = 4.5\pi$, respectively. As expected, the intensity of the signal in panel (e) is higher.

As anticipated in section 3.3, our slab is not ideal due to the limitations in the fabrication and the thickness of the slab may not be constant over the size of the beam spot. To facilitate a direct comparison with what follows, the absorptance calculated for an ideal 100 μm-thick slab shown in Fig. 3.9 is plotted again with a continuous black line in
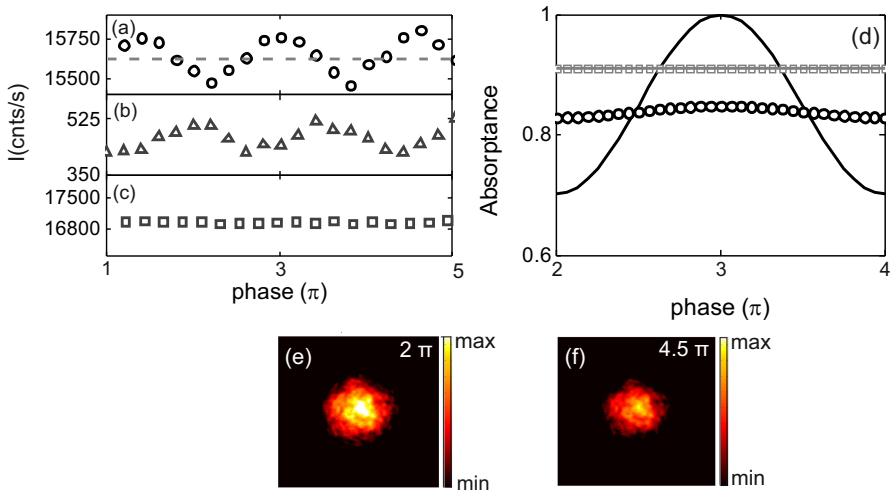
Figure 3.14: Modulation of the PL from a YAG:Ce layer. (a) Measurements of the modulation of the maximum of the PL as a function of the phase difference between beam (1) and beam (2), for an incident wavelength of 495.9 nm. Grey dashed line indicates the sum of the maxima of the measured PL with the two beams separately impinging on the sample. (b) Measurements of the far field scattering in the camera. (c) As in panel (a) but for an incident wavelength of 457 nm. (d) Continuous black line: calculation of the absorptance as a function of the phase difference between beams (1) and (2) for an incident wavelength of 495.9 nm. Black circle symbols: calculated absorptance averaged over a Δd = 200nm. Grey squares: calculated absorptance for the incident wavelength 457 nm. Grey continuous line: averaged absorptance calculated over a Δd = 200nm for the incident wavelength 457 nm. (e) and (f) Measured scattered intensity recorded by the camera for $\phi = \pi$ and for $\phi = 3.5\pi$, respectively.

Fig. 3.14(d). By averaging over the range of thicknesses, Δd = 200 nm, given by the non uniformity of the fabrication, we can reproduce the modulation measured for the PL. The black circles in Fig. 3.14(d) represent the calculated absorptance averaged over Δd, which modulation is now 2.5%. This reduction of the modulation can be understood by looking at Fig. 3.12, which shows that the range of thicknesses at which the scattered field is considerably suppressed is limited. Alternatively, it is in principle possible to mathematically reproduce the limited experimental modulation by considering the surfaces of the slab as perfectly plane-parallel, but with a surface roughness of roughly 10 nm, as measured with AFM [see Fig. 3.7(a)]. However, we consider this possibility very unlikely because it would imply a precision in the definition of the thickness on the order of 1 nm, which is not possible with the current set-up used.

As a comparison we have also measured the modulation of the PL when the sample is pumped at the maximum of the absorption coefficient of the YAG:Ce, λ_{max} = 457 nm, which is commonly the case to get the maximum absorption and the maximum emission. This is shown in Fig. 3.14(c) with dark grey squares. We have reproduced the response of the system through the transfer matrix method. In Fig. 3.14(d) the grey squares and the grey line represent the absorptance and the averaged absorptance for an ideal slab and for a Δd = 200 nm, respectively, for the wavelength 457 nm. The two overlap perfectly. For this wavelength the transmittance of beam (2) is almost 0, meaning that the transmitted light cannot modulate efficiently the reflected light of beam (1). This leads to $M \simeq 0$ and an absorptance which is two times the one of the single beam.

We finally notice that, in principle, the implementations of CPA in light-emitting structures offers the unique condition to reach the maximum amount of PL that a given sample can generate.

3.6 Conclusions

In this chapter we have analyzed the possibility of realizing Coherent Perfect Absorption (CPA) in a luminescent weakly absorbing material relevant for solid state lighting applications. We have highlighted the limitations that the imperfections due to the fabrication can rise and we have described which is the effect of those on the optical response of the system. Despite of these limitations, which prevented us from reaching the condition for CPA, we have experimentally demonstrated the possibility of external control and modulation of the intensity of the light emitted by a layer of YAG:Ce near the condition for CPA. The result is obtained with two counter-propagating beams illuminating the sample and creating a destructive interference pattern outside the layer. The pump light is trapped in the luminescent layer where it is eventually absorbed and efficiently converted. The CPA may allow for the total absorption of the incident light by weakly absorbing layers and therefore establishes the upper limit for the amount of light generated by a given emitting sample. The CPA applied to light emission may allow also for a reduction of losses in frequency down conversion processes due to the Stokes' shift reduction.

CHAPTER 4

COHERENT AND BROADBAND ENHANCED OPTICAL ABSORPTION IN GRAPHENE

We experimentally demonstrate a broadband enhancement of the light absorption in graphene over the whole visible spectrum. This enhanced absorption is obtained in a multilayer structure by using an Attenuated Total Reflectance (ATR) configuration and it is explained in terms of coherent absorption arising from interference and dissipation. The interference mechanism leading to the phenomenon of coherent absorption allows for its precise control by varying the refractive index and/or thickness of the medium surrounding the graphene. We demonstrate almost an order of magnitude improvement in the light absorption in our geometry with respect to the absorption of bare graphene.

4.1 Introduction

Graphene, a truly 2-dimensional gapless semiconductor, has been recognized as a revolutionary material for opto-electronic applications [68–70]. Several applications of graphene in various devices have been proposed, such as transparent electrodes [71, 72], ultrafast lasers [73], polarizers [74], and photodetectors [75]. The conductivity of graphene can be expressed as the sum of intraband and interband contributions. The first are dominant in the infrared and THz regions of the electromagnetic spectrum, while the second are dominant at optical frequencies, where graphene behaves as an absorbing dielectric. Indeed, at optical frequencies the onset of interband transitions leads to a negative imaginary component of its optical conductivity and a real component that approaches the universal conductivity value [76]. Photon absorption through interband transitions leads to the formation of electron-hole pairs, which are essential to build up an electric signal associated to the photodetection process. The low absolute value of the absorption of graphene (2.3% of the incident light is absorbed in a graphene layer [77]) constitutes the main limitation for the photocurrent efficiencies of graphene-based photodetectors [75, 78]. Therefore one of the challenges concerning this ultra-thin material is to enhance its optical absorption [68, 79].

4.1.1 Optics in graphene

One of the most remarkable properties of graphene is the universal value of its absorption at optical frequencies. This result comes directly from the universal value acquired by the optical conductivity due to interband transitions, which equals [80, 81]

$$\sigma = \frac{e^2}{4\hbar} \approx 6.08 \cdot 10^{-5} \Omega^{-1}. \tag{4.1}$$

The conductivity does not depend on any microscopic parameter that normally determine optical properties of materials. Absorption in graphene can be calculated by evaluating the reflectance and the transmittance of light through the graphene. Let us consider the geometry sketched in Fig. 4.1: an interface between two semi-infinite, isotropic and homogeneous media characterised by permittivities ϵ_1 and ϵ_2. A monolayer of graphene is placed at the interface corresponding to the plane $x = 0$. The graphene layer is seen by the incident field as a surface of free charges. In this chapter we will consider the case of the p-polarization, in which the field **E** is contained into the xz plane and the induced current has only the in-layer z component. For convenience, the amplitude of the incident field is set to 1. r and t are the amplitudes of the reflected and transmitted field, which correspond to the Fresnel reflection and transmission coefficients. These coefficients are obtained so that the magnetic **H** and electric **E** fields satisfy the boundary conditions [82, 83]:

$$E_{z,1}\big|_{x=0} = E_{z,2}\big|_{x=0}, \tag{4.2}$$

$$H_{y,1} - H_{y,2}\big|_{x=0} = \frac{4\pi}{c}\sigma(\omega)E_{z,2}\bigg|_{x=0}. \tag{4.3}$$
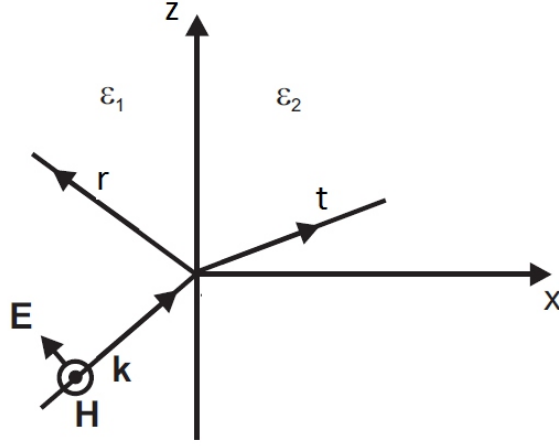
Figure 4.1: A schematic diagram of the incident, transmitted and reflected fields associated with a p-polarized electromagnetic wave incident on an interface bounded by two media characterized by complex permittivities ϵ_1 and ϵ_2.

Here c is the speed of light and $\sigma(\omega)$ is the frequency-dependent conductivity. In what follows, we will omit the dependence of σ on ω. By following the standard procedure of writing the plane wave solution of the Maxwell equations in medium 1 and 2 and by applying Eqs.(4.2) and(4.3), we obtain the amplitude, r, of the reflected field (see fig. 4.1) [57]:

$$r = \frac{1-C}{1+C},\tag{4.4}$$

with

$$C = k_{x,1}\left(\frac{\epsilon_2}{k_{x,2}\epsilon_1} + \frac{4\pi}{\omega}\sigma\right);\tag{4.5}$$

Where $k_{x,1}$ and $k_{x,2}$ are the normal components of the wavevector in medium 1 and 2, respectively. In the case of suspended graphene ($\epsilon_1 = \epsilon_2 = 1$) and for normal incidence, Eq. (4.5) simplifies to

$$C = 1 + \frac{4\pi\sigma}{c}.\tag{4.6}$$

At normal incidence the transmission coefficient equals [84]

$$t = 1 + r = \frac{2}{1+C}.\tag{4.7}$$

The absorption in graphene is given by

$$A = 1 - R - T = 1 - |r|^2 - |t|^2 = \tag{4.8}$$

$$= 1 - \left(-\frac{2\pi\sigma}{c}\right)^2\left(1 + \frac{2\pi\sigma}{c}\right)^{-2} - \left(1 + \frac{2\pi\sigma}{c}\right)^{-2}.\tag{4.9}$$

By using Eq. (4.1) and by introducing the fine-structure constant $\alpha = e^2/(c\hbar)$ we obtain

$$A = 1 - T\left(1 + \frac{\pi^2\alpha^2}{4}\right) = 1 - \left(1 + \frac{\pi\alpha}{2}\right)^{-2}\left(1 + \frac{\pi^2\alpha^2}{4}\right),\tag{4.10}$$

which, considering only the first order in α, can be approximated by [77]

$$A = 1 - (1 - \pi\alpha) = \pi\alpha \approx 2.3\%.\tag{4.11}$$

This results holds for the particular case of graphene.
By making use of Eq. (4.7), which for s-polarization is valid for any angle of incidence, it is possible to predict the maximum absorption of a thin layer embedded in a symmetric environment at normal incidence [84, 85]

$$A = 1 - |r|^2 - |t|^2 = 1 - |r|^2 - |1 + r|^2 = 50\%,\tag{4.12}$$

for r=-1/2, which is not the case for graphene.

This universal absorption of graphene, given by Eq. (4.11) is obtained in a very simple geometry. In the next section we describe a method to boost the absorption of graphene by embedding it in a complex photonic environment which leads to coherent absorption. As we described in Chapter 2 coherent absorption is realized through the interplay between interference and dissipation, which confines the light in the proximity of the absorbing material. One way to do that is to couple the incident light in guided modes supported by the thin absorbing layer. Guided modes correspond to the poles of the reflection coefficient. By introducing the renormalized quantities

$$\sigma_R = \frac{2\pi\sigma}{c} \qquad q_x = \frac{k_{x,1}}{\omega/c},\tag{4.13}$$

we can rewrite the reflection coefficient [Eq. (4.4)] of free-standing graphene for p-polarization as [86]

$$r = -\frac{q_x\sigma_R}{1 + q_x\sigma_R}.\tag{4.14}$$

Guided modes need to satisfy the equation

$$1 + q_x\sigma_R = 0 \quad \longrightarrow \quad q_x = -\frac{1}{\sigma_R} = -\frac{\sigma_R^*}{|\sigma_r|^2},\tag{4.15}$$

where σ_R^* indicates the complex conjugate of σ_R. Since the imaginary component of q_x has to be positive in order to satisfy the radiation condition, also the imaginary component of σ_R has to be positive, independently on the value of its real part. But in the optical region of the electromagnetic spectrum this imaginary component is negative, which means that graphene cannot support guided modes at these frequencies.

4.1.2 Enhanced absorption in graphene

In general, enhancing and controlling light absorption in optical devices is receiving significant attention due to the increasing interest in its fundamental and practical aspects [7, 8, 33, 36, 87–89]. Typical parameters to be optimized are the spectral and angular window of illumination over which the enhanced absorption takes place and its dependence on the polarization of the incident light. The optical absorption of graphene integrated in silicon waveguides has been recently demonstrated by Liu and coauthors [90] and by Li and coauthors [91]. A way to increase the photocurrent in graphene-based detectors has been demonstrated by M. Furchi and coauthors by integrating the graphene in a microcavity defined by a pair of Bragg mirrors [92]. Engel and coauthors [93] used the cavity defined by metallic mirrors to enhance the photocurrent of a graphene-based transistor. These approaches lead to a large enhancement of the optical absorption in a limited range of wavelengths (~ 50 nm) and angles of incidence. A detailed theoretical description of a graphene integrated microcavity has been accomplished by Ferreira and coauthors in Ref. [94]. A plasmonic-assisted enhancement of the electric field near the contacts of a graphene-based photodetector has been exploited by Echtermeyer and coauthors to enhance the photovoltage [95]. Also the possibility to achieve complete absorption in graphene at infrared frequencies making use of plasmonic resonances has been theoretically investigated in nanopatterned graphene by Thongrattanasiri and coauthors [85]. Experimetal works related to this prediction have been realized by Fang and coauthors who showed that an array of closely packed graphene nanodisks absorbs up to 30% in the infrared region of the spectrum [96]. The complementary structure, i.e. a periodic graphene antidot array, has been theoretically studied by Nikitin and coauthors in Ref. [97], showing a maximum absorption of 50% with the advantage of having an electrically continuous system.

In this chapter we demonstrate a simple, yet robust, configuration to achieve a remarkably large, broadband and polarization independent absorption of visible light in graphene. This enhanced absorption is achieved by interference and dissipation in a four layers structure. One of these layers is a graphene monolayer or multilayer (depending on the sample). The graphene is sandwiched between two non-absorbing dielectrics with slightly different refractive indexes. Light impinges onto this structure through a high refractive index prism at a large angle of incidence. Destructive wave interference builds up in reflection, while the optical transmission vanishes due to total internal reflection. The coherent suppression of reflection and transmission translates into an enhancement of the absorption of graphene. In contrast to previous works, this simple structure enables a broadband enhancement of the absorption in a narrow window of angles of incidence. We experimentally show an absorptance higher than 10% for a monolayer of graphene over a range of wavelengths spanning from 525 nm till 800 nm. This absorption increases to 70% and 80% for 5 and 10 layers of graphene, respectively. We also show how the absorption of the 10 graphene layers can be optimized to reach values as large as 91%. Moreover, the absorption can be precisely controlled by changing the difference in refractive indices of the dielectrics embedding the graphene.
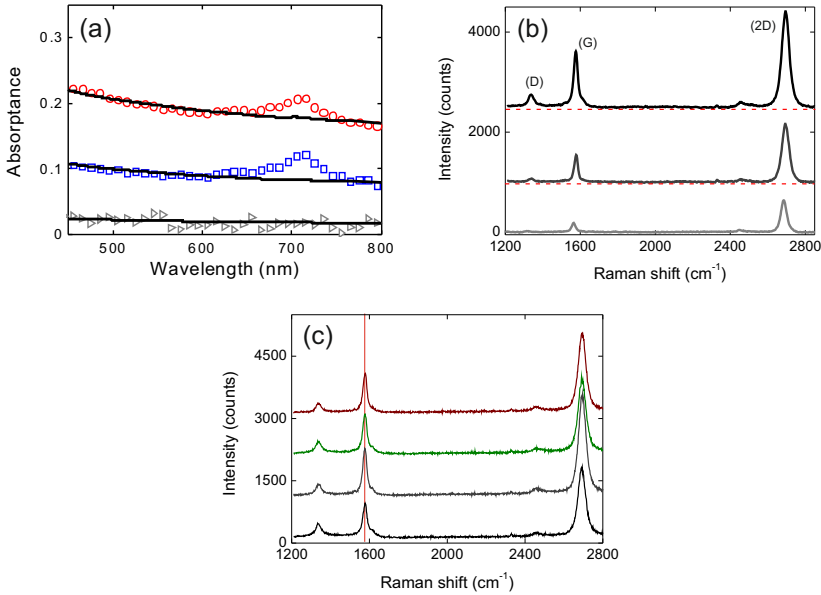
Figure 4.2: (a) Measured and calculated absorptance of graphene mono- and multi-layers. The measured absorptance is displayed with red open circles, blue squares and grey triangles for 10 layers, 5 layers and a monolayer of graphene, respectively. The curves correspond to the calculations of the absorptance using the transfer matrix method. (b) Raman spectra of a monolayer (light grey curve), 5 layers (dark grey curve) and 10 layers (black curve) of graphene on a quartz substrate. For clarity, the curves of the 5 and 10 layers have been vertically shifted. Red dashed lines indicate the baseline of the measurements. (c) Raman spectra of the sample with 10 layers of graphene on a quartz substrate taken from 4 different locations in the sample with a large separation (∼ 1 mm).

4.2   Sample characterization

Three samples were prepared in order to investigate the enhanced absorption in graphene: The first one is formed by 10 layers of graphene, the second by 5 layers of graphene and the third by a monolayer. The graphene was grown by the company GrapheneSupermarket [98], by chemical vapor deposition on copper foil and deposited, through PMMA transfer, onto a silica substrate. The PMMA was removed with acetone [99]. This process was repeated as many times as layers were deposited. The stacking of the multi-layer samples is turbostratic, which means that the layers are randomly aligned, thus preserving the graphene properties. Raman measurements show that these multilayers have a net graphene behavior and do not form graphite. An Ar$^+$ laser is used as a source operating at the wavelength of 514 nm providing a power on the sample of 20 mW. Figure 1(a) displays the optical characterization of the three samples through absorptance measurements in an integrating sphere at normal incidence. The absorptance is defined as 1-R_T-T_T,

with R_T and T_T the total reflectance and total transmittance, respectively. The red open circles, blue squares and grey triangles correspond to the measurements of 10, 5 and 1 graphene layers, respectively. The small bump at $\lambda = 700$ nm is due to residual absorption from impurity iron particles involved in the deposition process of the graphene. The solid curves in Fig. 1(a) are fits to the measurements using the transfer matrix method. For these fits, we model the samples as a 3 layers system, consisting of a substrate, the graphene and air. The absorption band of the iron particles is not included in the model and we consider the silica substrate to be non-dispersive with a permittivity $\epsilon_{\text{sub}} = 2.08$. The graphene (multi-)layer can be described as a uniaxial material, characterized by an ordinary in-plane permittivity and by an extraordinary out-of-plane permittivity [100]. Since the absorptance measurements in Fig. 4.2(a) are performed near normal incidence, the graphene layers are described only by the ordinary permittivity. The birefringence will be later taken into account when measurements at an inclined angle of incidence are discussed. The ordinary refractive index is related to the optical conductivity, σ, by $\epsilon_o = 4\pi i \sigma / \omega h$, where ω is the frequency of the incident wave and h is the thickness of the graphene layer. The permittivities of the graphene layers at 540 nm are obtained from the fits to the transmission and reflection measurements are $\epsilon_o = (5.9 \pm 0.8) + i(10.2 \pm 0.6)$, $(7.8 \pm 0.8) + i(8.5 \pm 0.4)$ and $(7.1 \pm 3.2) + i(7.9 \pm 1.4)$ for 10, 5 and 1 graphene layers. These values are in reasonable agreement with $\epsilon_o = 5.6 + i7.0$ reported by Kravets *et al.* [100] and the absorptance is consistent with the well known value of 2.3% per graphene layer predicted by Kuzmenko *et al.* [77]. The discrepancy in the permittivity between measurements and reported values, which in the worst case is around 30%, can be attributed to differences in the fabrication process and the aforementioned impurities present in our samples.

To confirm the behavior of the graphene multilayers as a stack of monolayers (instead of thin graphite sheet), we have performed Raman spectroscopy. It is known that the frequency of the G-Raman line, the intensity of the D-Raman line, the relative intensity of the G- to 2D-Raman lines, and the line shape of the 2D-line give a valuable indication of the quality of graphene [101]. The black, dark grey and light grey curves in Fig. 4.2(b) are Raman spectra obtained under a 514 nm illumination of 10, 5 layers and the monolayer of graphene, respectively, where the first two have been vertically displaced for clarity. We see the following features as a function of the number of graphene layers: i) the intensity of the 2D-line is always larger than the intensity of the G-line, ii) the intensity of the D-line remains low, and (iii) the 2D-line maintains a lorentzian-like shape. These observations provide an excellent indication that all the samples have a net graphene-like behavior and do not form graphite. As expected the intensity of the Raman signal increases with the number of graphene layers [102]. The fact that a graphene behavior is found even for the 10 layer sample can be explained by considering the random relative alignment of the stacked layers resulting from the deposition. The frequency shift of the G-line is known to provide information about the number of graphene layers stacked together [102–104]. In Fig. 4.2(c) we display 4 spectra taken from different locations in the sample with 10 layers of graphene for which imperfections due to the layer by layer deposition could be more important. The identical Raman frequency of the G-line confirms that the sample is

homogeneous.

4.3 Coherent absorption measurements

In order to demonstrate the coherent and enhanced absorption in graphene multilayers, we have built the structure schematically represented in Fig. 4.3(a). A silica layer with a defined thickness on the order of the wavelength of the incident light and permittivity $\epsilon_{silica} = 2.12$ is sputtered on top of the graphene. The layer is grown in steps, i.e., alternating two minutes of deposition with two minutes of cooling, in order to keep the temperature of the sample around 70°C. The deposition rate is 3.6 nm/min. The permittivity of the silica layer has been chosen to be very close but slightly larger than the one of the quartz substrate ($\epsilon_{sub} = 2.08$). A prism made of F2 glass with a permittivity $\epsilon_p \sim 2.59$ and slightly dispersive in the visible, is in optical contact with the silica layer by means of an optical grade liquid and it is used to couple the incident light into the multilayer structure. This is the standard Attenuated Total Reflectance (ATR) configuration in which the refractive index of the prism has to be higher than the refractive index of the substrate in order to allow for total internal reflection of the incident light. A similar configuration has been theoretically modeled by Bludov and coauthors to enhance the absorption of THz (far-infrared) by graphene [105, 106]. In that work the authors exploit an evanescent coupling through a prism to excite graphene surface plasmon polaritons. Note that our work focuses on the visible part of the spectrum where graphene exhibits a dielectric behaviour and do not support surface plasmons. The total internal reflection prevents the light to be scattered in the transmission far-field for angles of incidence θ larger than the critical angle. The critical angle angle for total internal reflection at the prism-silica interface is $\theta_{c,1} = \arcsin(\sqrt{\epsilon_{silica}}/\sqrt{\epsilon_p})$, while the critical angle for total internal reflection at the silica-substrate interface is $\theta_{c,2} = \arcsin(\sqrt{\epsilon_{sub}}/\sqrt{\epsilon_{silica}})$. These interfaces are labeled with 1 and 2, respectively, in Fig. 4.3(a). The angle of incidence θ^* on the prism-silica interface corresponding to $\theta_{c,2}$ can be evaluated applying Snell's law, i.e., $\sqrt{\epsilon_p} \cdot \sin(\theta^*) = \sqrt{\epsilon_{silica}} \cdot \sin(\theta_{c,2})$. If $\theta < \theta^*$ the incident wave propagates through the multilayer structure and a fraction of the amplitude is transmitted. When $\theta^* < \theta < \theta_{c,1}$ the incident wave is transmitted through the prism-silica layer interface and undergoes total internal reflection at the silica-substrate interface. If $\theta > \theta_{c,1}$ the wave undergoes total internal reflection at the prism-silica interface. Therefore, the last two conditions result in a transmittance equal to 0.

Specular reflectance (R) measurements have been performed for the three samples. The measurements are normalized to the specular reflection at an angle of incidence of $\theta = 65.3° > \theta_{c,1}$, at which a reflectance of 1 is expected due to total internal reflection at the prism-silica interface. For $\theta > \theta^*$ the absorptance is defined as $A = 1 - R$. Figure 4.3(b) displays the experimental absorptance of the 5 layers of graphene as a function of the wavelength and the angle of incidence for p-polarized incident light at $\theta > \theta^*$. The red and pink dashed lines in Fig. 4.3(b) represent the dispersion of θ^* and $\theta_{c,1}$, respectively. Following the dispersion of θ^* we see a band in which the absorptance reaches values
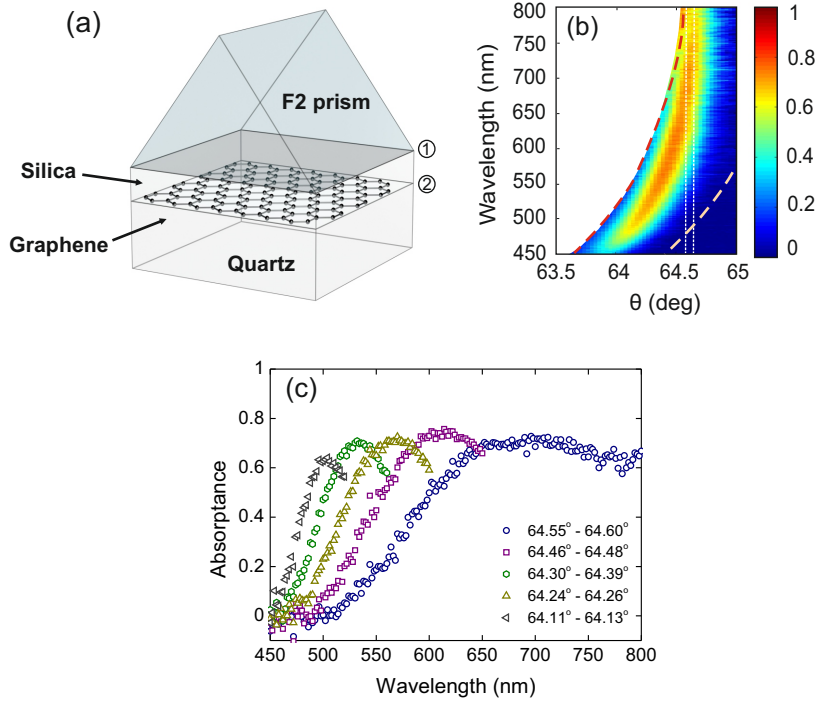
Figure 4.3: (a) Schematic representation of the multilayer structure formed by a quartz substrate, a graphene layer, a silica layer and a F2 prism. (b) Measured absorptance spectra (color scale) from the structure shown in (a) in which the graphene layer is formed by 5 monolayers randomly stacked. The incident light is p-polarized. The absorptance, evaluated as 1-Reflectance, is displayed as a function of the wavelength and the angle of incidence on the prism-silica interface. (c) Integrated absorptance over the angular ranges $\Delta\theta$ indicated in the legend. The blue dots correspond to the absorptance evaluated in the angular range identified by the dashed white lines in (b).

as large as 0.75. This band of enhanced absorptance covers the whole visible spectrum from 460 nm to 800 nm. To better visualize the absorption enhancement, the averaged absorptance over a narrow range of angles of incidence ($\Delta\theta \simeq 0.05°$) is plotted in Fig. 4.3(c) as a function of the wavelength. The blue circles correspond to the angular window identified by the dashed vertical lines in Fig. 4.3(b). The other absorptance spectra are obtained in a similar way for different angular ranges. We see over the whole visible spectrum an experimental absorptance at certain angles of incidence larger than 60%, i.e., pronouncedly larger than the 11.5% expected for 5 layers of graphene and measured in Fig. 4.2(a). The steep dispersion of the absorption band of Fig. 4.3(b) gives rise to a broadband enhanced absorption mainly in the red and near infrared part of the spectrum around 64.5°.

Similar measurements of the absorptance for the 10 layers of graphene and for the

Figure 4.4: Measured absorptance as a function of wavelength and angle of incidence for p-polarized light of the multilayer system depicted in Fig. 4.3(a), with (a) 10 and (b) 1 layers of graphene.

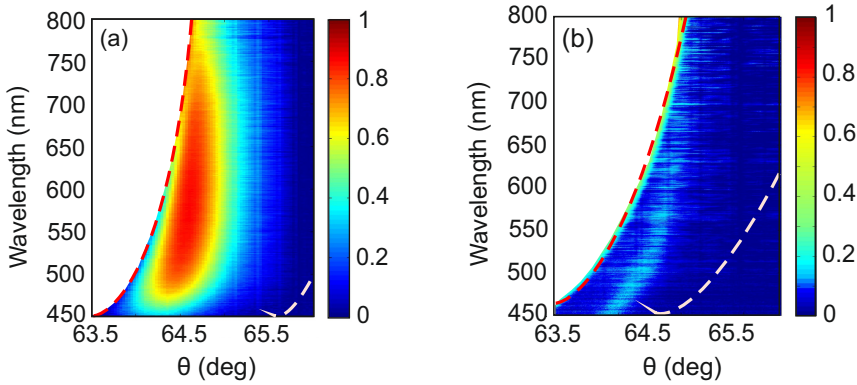monolayer of graphene are shown in Fig. 4.4. The bandwidth of enhanced absorption is further improved for the 10 graphene layers sample where an absorptance larger than 70% is measured from 525 nm until 800 nm at $\theta = 64.7°$. For the monolayer of graphene we reach and enhanced absorption of 15% which corresponds to an improvement by a factor 7. As we demonstrated in section 4.1.1, it is worth noting that a thin layer of an absorbing material in a symmetric environment cannot absorb more than 50% of the incident light [85]. Therefore, the presence of the asymmetry in the permittivity of the surrounding media is crucial to boost the absorption of the graphene.

Fig. 4.5(a) displays the measured absorptance as a function of the incident angle for a p-polarized illumination wavelength of 540 nm and for the 10 graphene layers (open circles), the 5 graphene layers (open squares), and the monolayer (open triangles) of graphene, respectively. In Fig. 4.5(b) is plotted the calculated absorptance evaluated by means of the transfer matrix method for the same layers, polarization and illumination wavelength of the measurements, i.e., for 10 (solid black curve), 5 (dashed dark-grey curve), and 1 layer (dot-dashed light-grey curve) and p-polarized light of $\lambda = 540$ nm. The calculations model the layers through their thicknesses and permittivities assuming them as perfectly flat. The thicknesses and the permittivity of the silica layer have been determined by ellipsometry measurements. These thicknesses of the silica layers are 590 nm, 1200 nm and 1300 nm for the 10 layers, 5 layers and monolayer of graphene samples, respectively. We model the graphene as a uniaxial material with a complex permittivity $\epsilon_g(\lambda, \theta) = \epsilon_o(\lambda) + \frac{\epsilon_o(\lambda) - \epsilon_e(\lambda)}{\epsilon_e(\lambda)} \sin^2\theta$, where $\epsilon_o(\lambda)$ is the complex ordinary permittivity, and $\epsilon_e(\lambda)$ is the complex extraordinary permittivity, fixed to the value of $3.9 + i0.7$ as determined in Ref. [100]. The complex ordinary permittivity of graphene is taken from the fits shown in Fig 4.2(a). Therefore, no fitting parameter is used in the calculations shown in Fig. 4.5(b). The discrepancy between the measurements and the calculations in the strength of the absorption can be

attributed to the presence of the aforementioned impurity particles on the surface of the graphene and to a possible small modification of the optical constants of the graphene layers caused by the deposition of the silica layer. Nevertheless, these calculations reproduce perfectly the shape and the angular position of the absorption resonances of the three samples.
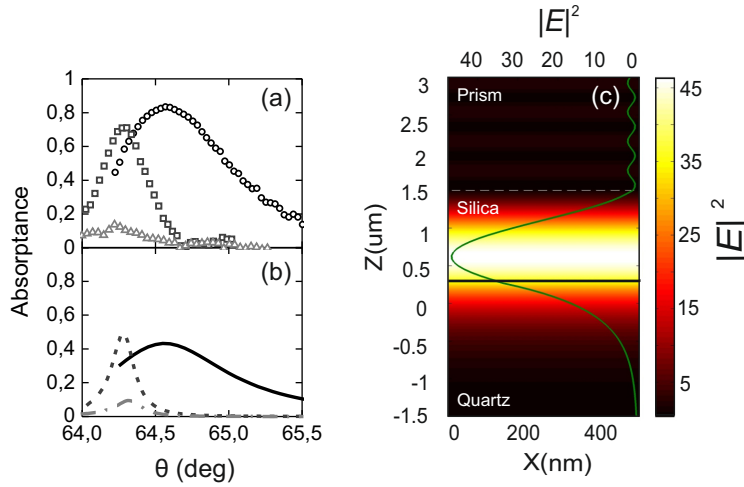
Figure 4.5: Measured (a) and calculated (b) absorptance spectra as a function of the angle of incidence of a plane wave with a wavelength of 540 nm and for the multilayer system represented in Fig. 4.3(a). Open circles and black solid curve correspond to 10 layers of graphene, open squares and dark-grey dotted curve correspond to 5 layers of graphene, and open triangles and grey dash-dotted curve correspond to a monolayer of graphene. (c) Spatial distribution of the total electric field intensity $|E|^2$, normalized by the incident intensity, for the 5-layers graphene sample at $\lambda = 540$ nm and $\theta = 64.3°$. From top to bottom: prism (semi-infinite), silica layer (1200 nm), graphene (solid line) and substrate (semi-infinite). Green curve: $|E|^2$ as a function of z (scale on the upper horizontal axis).

4.4   Interpretation in terms of the S-matrix

The enhanced absorptance observed in the measurements, and qualitatively reproduced by the transfer matrix calculations, is associated with the excitation of a resonance in the multilayer structure. To gain physical insight, the experiment can be described as a scattering problem, i.e., as an incident beam traveling in a medium with permittivity ϵ_p and scattered (transmitted and reflected) by the multilayer. The scattering matrix, S, relates the asymptotic incoming and outgoing amplitudes of the reflected and transmitted waves. The scattering matrix can be obtained by solving Maxwell equations in each medium and applying the continuity of the tangential components of the fields at each interface. This

results in

$$S = \begin{pmatrix} S_{11} & S_{12} \\ S_{21} & S_{22} \end{pmatrix} = \begin{pmatrix} t^p_{1234} & r^p_{4321} \\ r^p_{1234} & t^p_{4321} \end{pmatrix}, \tag{4.16}$$

where r^p_{1234}, t^p_{1234}, r^p_{4321}, t^p_{4321} are the reflection and transmission Fresnel coefficients for p-polarization for the 4-layer system and the subindices 1, 2, 3 and 4, label the prism, the silica layer, the graphene (multi-) layer and the substrate, respectively. The Fresnel coefficients are given by [107]

$$r^p_{ijkl} = \frac{r^p_{ij} + r^p_{jkl}e^{-2\alpha_j d_j}}{1 + r^p_{ij}r^p_{jkl}e^{-2\alpha_j d_j}}; \qquad t^p_{ijkl} = \frac{t^p_{ij} t^p_{jkl}e^{-\alpha_j d_j}}{1 + r^p_{ij}r^p_{jkl}e^{-2\alpha_j d_j}}. \tag{4.17}$$

Where d_j is the thickness of the j-th layer, r^p_{ij} and t^p_{ij} are the Fresnel reflection and transmission coefficients for the single interfaces, which are given by

$$r^p_{ij} = \frac{\epsilon_j \alpha_i - \epsilon_i \alpha_j}{\epsilon_j \alpha_i + \epsilon_i \alpha_j}, \qquad t^p_{ij} = \frac{2\sqrt{\epsilon_i \epsilon_j}\alpha_i}{\epsilon_j \alpha_i + \epsilon_i \alpha_j}, \tag{4.18}$$

with ϵ_i the permittivity of the medium i, and α_i is the component of the wavevector perpendicular to the interfaces, *i.e.*,

$$\alpha_i = \frac{2\pi}{\lambda}\sqrt{\epsilon_1 sin^2\theta - \epsilon_i}. \tag{4.19}$$

r^p_{jkl} and t^p_{jkl} in Eq. (4.17) are the Fresnel coefficients of the system composed of layers j, k, l, given by

$$r^p_{jkl} = \frac{r^p_{jk} + r^p_{kl}e^{-2\alpha_k d_k}}{1 + r^p_{jk}r^p_{kl}e^{-2\alpha_k d_k}}; \qquad t^p_{jkl} = \frac{t^p_{jk} t^p_{kl}e^{-\alpha_k d_k}}{1 + r^p_{jk}r^p_{kl}e^{-2\alpha_k d_k}}. \tag{4.20}$$

With these definitions, S_{21} relates the reflected amplitude, H_r, with the incident amplitude, H_i, of the magnetic field. Therefore, $|S_{21}|^2$ is the specular reflectance (R) that we measure. In particular for $\theta > \theta^*$ for which the transmittance vanishes, a minimum in $|S_{21}|^2$ corresponds to a maximum in the graphene absorptance. The zeros of S_{21} correspond to the condition of perfect antireflection resulting from Fabry-Pérot modes at which the phases and the amplitudes of the scattered waves at each interface are such that R approaches 0. In order to achieve antireflection, the reflected wave at the prism-silica interface needs to have a phase difference of 180° with the scattered wave from the other interfaces. This condition is necessary to obtain destructive interference in reflection. Assuming an amplitude of 1 for the incident wave, the amplitude and phase of the aforementioned scattered wave are given by $r_{scatt} = r^p_{1234} - r^p_{12}$. This out-of-phase condition can be controlled by a proper choice of the thickness of the silica layer over which the scattered wave accumulates a phase. Therefore, the optimum thickness of the silica layer can be evaluated by finding the minimum of $|S_{21}|^2$ as a function of the thickness of the silica layer and of the angle of incidence. For the sample with 10 layers of

graphene and using the values for the permittivity of graphene obtained from the fits of Fig. 4.2, we find $d_{\text{silica,opt}} = 1.7 \ \mu m$, for $\lambda = 540$ nm and $\theta = 65.6°$. With this thickness we find $r_{\text{scatt}} = 0.9 e^{-i173°}$, which is almost perfectly out-of-phase with $r_{12}^p = 0.7 e^{i0°}$.

It is important to note that a perfect destructive interference pattern, i.e. perfect antireflection, is only possible if the absolute value of the amplitudes of r_{scatt} and r_{12}^p are equal. The role of the graphene (multi-) layer is to account for this amplitude condition by removing energy from the wave scattered by the multilayer. In the optimized case the absorptance in the 10 layers of graphene is 91%. However, it was not possible in the experiments to reach the optimum thickness of the silica layer with the method used for the growth. Regarding the samples with 5 layers and the monolayer of graphene, a similar analysis leads to a maximum absorptance in the graphene of 76% and 15%, respectively. This means that the 5 graphene layers and the monolayer do not absorb enough energy and the matching condition for the amplitudes is not satisfied in order to achieve full absorption. At this point it is worth mentioning that another way to exploit Fabry-Pérot resonances has been demonstrated by Blake *et al.* for making graphene more easily visible under a microscope [108].

The analysis of the optical absorption in terms of the scattering matrix has been recently exploited to describe the concept of Coherent Perfect Absorption (CPA) [5, 15, 26]. In Chapter 1 we saw that according to this description a proper combination of interference and dissipation in a weakly absorbing slab, giving rise to eigenvalues of S equal to zero, lead to complete absorption of the incident light. This perfect absorption has been interpreted as the time reversal of a lasing mode. In Chapter 3 we have described thoroughly the theory behind CPA and we have further developed the concept of enhanced absorption by CPA. We saw that the CPA process is associated to the superposition of two Fabry-Pérot of counter propagating beams [15]. Following this description, the ATR configuration described here could potentially represent a route towards the realization of one input channel CPA [109]. As already discussed in Chapter 1, the ATR configuration in combination with lossy very thin films has been investigated by Driessen and de Dood [7] in the context of perfect absorption. In that work the authors attached the thin film directly to the prism and achieved absorption of 94% for s-polarized incident light. The energy was dissipated in the film at the critical angle for total internal reflection and the absorption was due to the presence of evanescent waves. In this Chapter we achieve remarkably high enhanced absorption in a graphene layer spatially displaced with respect to the prism and for p-polarized incident light. The enhanced absorption takes place for angles larger than the angle for total internal reflection at the silica-substrate interface, but smaller than the angle for total internal reflection at the prism-silica interface. Therefore the enhanced absorption originates from a combination of evanescent waves excited at the position of the graphene layer, and multiple reflections in the silica layer.

As discussed in Chapter 2, another way to increase the absorptance in graphene could be to exploit the coupling of the incident light to guided modes supported by the multilayer

structure. The scattering matrix formalism can be used to obtain the dispersion relation of such modes by evaluating the poles of the S_{21}. The only guided modes supported by a graphene layer in the visible are the TE surface plasmon polaritons [86, 110], while guided modes in the silica layer are not allowed because $\epsilon_p > \epsilon_{silica}$. Consequently, this approach can not be used in our system to enhance the absorption of p-polarized light.

Figure 4.5(c) displays the spatial distribution of the intensity of the total electric field $|E|^2$, normalized by the incident intensity, in the multilayer system formed by the 5 layers of graphene for an incident wavelength and angle of $\lambda = 540$ nm and $\theta = 64.3°$, i.e., for the wavelength and angle of incidence of maximum absorptance shown in Figs. 4.5(a) and (b). From top to bottom, Fig. 4.5(c) shows the prism (semi-infinite), the silica layer (1200 nm), the graphene multilayer (solid line) and the substrate (semi-infinite). The largest intensities are found in the silica and in the graphene layers. In Fig. 4.5(c) we also plot a cut of $|E|^2$ (green curve), showing the different behavior of the field in reflection and in transmission. Since the angle of incidence is such that $\theta^* < \theta < \theta_{c,1}$ (see Fig. 4.3(b)), the electromagnetic field is evanescent in the substrate but propagating in the silica layer and in the prism. The large intensity enhancement in the absorbing layer of graphene and the aforementioned destructive interference in reflection, explain why a resonance in a simple multilayer can boost the absorption of graphene.

4.5 Control over the absorption

The interference nature of the resonance giving rise to the enhanced absorption offers the opportunity to modulate this absorption. By tuning the permittivity of the media embedding the graphene layer is possible to modify the interference conditions, allowing part of the light to be reflected, and reducing the absorption. This tunability of the absorption is illustrated in Fig. 4.6. Figure 4.6(a) shows the calculated absorptance for the 5 graphene layers sample. The transmittance and specular reflectance are evaluated with the transfer matrix method using the permittivities as in Fig. 4.5.

Figure 4.6(b) shows the calculated absorptance for the same set of permittivities as in Fig. 4.6(a) but with $\epsilon_{silica} = 2.15$ (instead of 2.12). The resonance shifts to larger angles and the absorptance decreases. Figures 4.6(c) and (d) further illustrate how tuning the permittivities of the media surrounding the graphene allows for the control of the fraction of absorbed light at specific angles. These figures show the averaged absorptance obtained from Figs. 4.6(a) and (b), respectively, over the same angular ranges as in Fig. 4.3(c). The shift in the resonance as the permittivity of the silica layer is varied leads to a strong reduction of the absorptance at fixed wavelengths (see Fig. 4.6(d)).

4.6 Conclusions

In conclusion, we have experimentally demonstrated a broadband enhancement of light absorption by graphene at optical frequencies by using an attenuated total reflection

configuration in a simple multilayer structure. This broadband enhanced absorption is explained in terms of coherent absorption, which arises from the interference and dissipation in the multilayer structure. The engineered optical interference gives rise to a large electric field intensity in the proximity to the graphene layer, which is thereby dissipated. Almost an order of magnitude enhanced absorption is achieved.
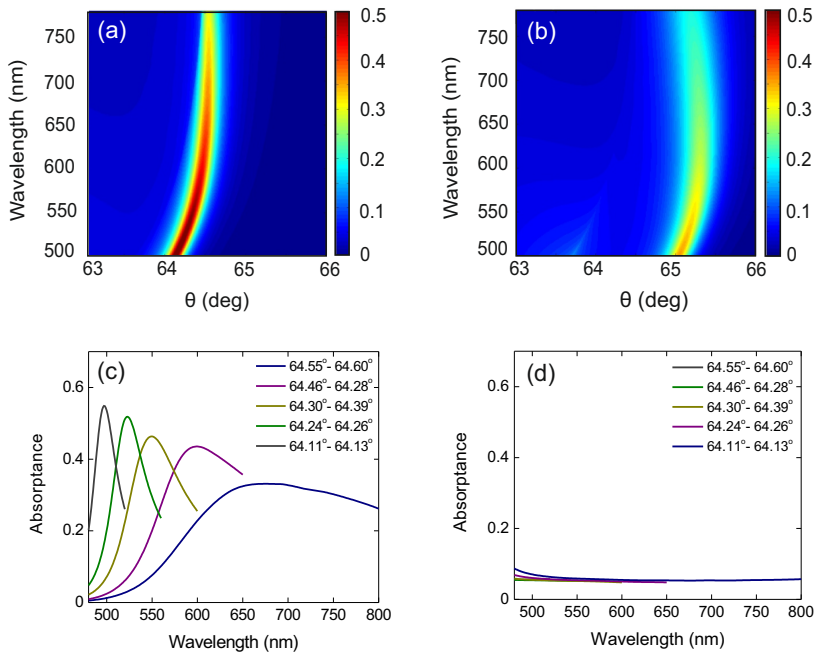
Figure 4.6: (a) Calculated absorptance as a function of the wavelength and angle of incidence for the 5-layers graphene sample described in Fig. 4.3(a). (b) Calculated absorptance as a function of wavelength and angle of incidence for the same sample but with $\epsilon_{\text{silica}} = 2.15$ instead of 2.12. (c) and (d) Integrated absorptance calculated from (a) and (b), respectively, over the angular windows indicated in the figure legends.

CHAPTER 5

ENHANCED LIGHT ABSORPTION IN GRAPHENE BY ARRAYS OF NANOANTENNAS.

We present a novel design for a graphene-based photodetector which combines a metallic array of nanoparticles with a monolayer of graphene. The metallic array sustains collective resonances arising from the radiative coupling of localized plasmon resonances. We design the system in order to maximize the interaction between the graphene layer and the light distributed in the structure. We calculate that one of these modes allows for an enhancement of the optical absorption of graphene by a factor 7. A proportional photocurrent enhancement factor is predicted.

5.1   Graphene-based photodetectors

Photodetectors are used in a wide range of applications such as imaging devices and sensitive optical detectors for broadband or single wavelength detection [111, 112]. Different technologically important wavelength regimes are detected by separate photoactive semiconductors with appropriate bandgaps. For example, GaN, silicon and InGaAs are typically exploited for sensing in the ultraviolet, visible and near-infrared, respectively, whereas the detection of mid-infrared photons generally relies on small-bandgap semiconductors such as HgCdTe, PbS or PbSe. Thermal sensing techniques are used for detection in the far-infrared regime.

In contrast to these bulk semiconductors, two dimensional materials, such as graphene, have been shown to be very promising for optical detection [75]. Electron-hole pairs are generated upon light absorption, and if an external DC electric field is applied, the pairs can be separated and a photocurrent is generated. There are two main advantages that graphene offers with respect to other materials: it can be used in a wide range of wavelength because of its broadband absorption from the THz to the UV and the high carrier mobility of graphene opens up possibilities for ultra-fast detection [113]. Using these characteristics, Xia and coauthors have demonstrated ultrafast transistor-based photodetectors made from single- and few-layer graphene [78]. Mueller and coauthors reported the first use of a photodetector based on graphene in an optical datalink [75]. However, as we discussed in Chapter 3, the photocurrent efficiency of graphene-based photodetectors is limited by the low absolute value of the absorption (only 2.3% is absorbed in the visible for a single graphene layer [77, 114]). Therefore, one of the challenges concerning this ultra-thin material is to enhance its optical absorption [68, 79].

Several approaches to achieve enhanced absorption in graphene have been recently proposed. Integrating graphene in microcavities can enhance its interaction with light and improve the responsivity [92, 93, 115]. Combining graphene and quantum dots in a hybrid system can dramatically increase the photoresponsivity [116]. However, the enhancement of the absorption can be only achieved at the designed resonant frequencies, restricting their applications for broadband photodetection. With this in mind, the concept of silicon waveguide-integrated graphene photodetectors was recently proposed, demonstrating broadband photodetection with enhanced responsivity [90, 91]. An alternative approach to achieve broadband enhanced absorption is the multilayer stack that we propose in Chapter 4 [117]. Another configuration able to maintain the broadband absorption of graphene has been proposed by Zhang and coauthors who create a bandgap in graphene through band structure engineering [118]. They measured a photoresponsivity three orders of magnitude higher than those reported so far. A potential drawback of this approach stems from the difficulty in the careful creation of quantum dot-like structures in the graphene layer. Instead of structuring the graphene layer, Liu and coauthors fabricated a photodetector based on a graphene double-layer heterostructure showing ultra-broadband room temperature photodetection from the visible to the mid infrared range [119].

A different strategy to enhance the optical absorption of graphene envisages the combination of graphene with metallic nanostructures. Strong light-graphene interactions enhanced by surface plasmons, the collective electron oscillations supported by metals, is currently being explored [70]. Metallic nanoantennas have been shown to be highly efficient harvesters of visible and near infrared light at wavelengths chosen by tailoring the size and shape of the antenna structure. Surface plasmons provide the dominant mechanism for the antenna response in this wavelength range resulting in a great enhancement of the electromagnetic field. Fang and coauthors demonstrated an integrated plasmonic antenna-graphene photodetector consisting of plasmonic clusters sandwiched between two layers of graphene [120]. In Ref. [121], Liu and coauthors deposited a metallic array of nanoparticles on a graphene layer exploiting localized surface plasmons to enhance the absorption of different colors.

The disadvantage of the experiments dealing with metallic nanoantennas proposed so far is that they exploit localized resonances in which the electromagnetic field is very much confined around the metallic particles, therefore limiting the area of interaction with graphene. In this chapter we propose the use of delocalized hybrid photonic-plasmonic modes, which allow for an improved overlap of the enhanced electric field and the graphene layer.

5.2 Collective resonances sustained by a metallic array of nanoparticles

All the devices mentioned in the previous section are either limited in wavelength, show limited angular acceptance, do not make optimal use of the whole area of the absorbing material or are difficult to implement in production scale devices. In this chapter we propose a different approach to enhance the optical absorption in graphene, which relies on collective resonances of a metallic array of nanoparticles placed at a finite distance from the graphene layer. In Section 5.3.1 we will show an efficient use of the area covered by the graphene layer, while the option of an angular-spectral tunability will be addressed in Section 5.4.

While single metallic nanoparticles can sustain localized surface plasmon resonances (LSPRs), a periodic array of these nanostructures may exhibit collective resonances resulting from the radiative coupling of LSPRs. There are two distinct mechanisms able to enhance this radiative coupling. The first mechanism relies on Rayleigh anomalies (RAs) or diffracted orders in the plane of the array, which leads to the hybridized resonances known as surface lattice resonances (SLRs) [122]. The first studies on SLRs were made by Carron and coworkers [123] and later by Schatz and coworkers [124, 125], but only recently experimental observation of such resonances was obtained [126]. On the other hand, if a thin dielectric waveguide structure is placed in close proximity to the array of nanoparticles, LSPRs can also allow the coupling of the incident light to quasi-guided

modes [127–129]. As a consequence of the coupling, SLRs and quasi-guided modes are characterized by a mixture of the properties of the two bare states: they show high field enhancement while being delocalized, i.e. the energy distribution can extend several hundreds of nanometers in the direction perpendicular to the plane of the array. The signature of the coupling is an anticrossing in extinction measurements, giving rise to the so-called Rabi splitting. The resulting mixed mode can exist in different coupling strengths: the coupling is strong when the Rabi splitting is larger than the linewidth of the individual resonances, while it is weak in the opposite case. In either case, the degree of hybridization depends on the relative contribution of the resonances that are coupled. This contribution can be evaluated by considering the wavelength detuning between the two resonances: if it is large the coupled mode resembles one or the other of the bare modes. The strength of the coupling is also related to the spatial overlap of the fields of the two bare states: the larger the overlap, the stronger the coupling. The strong coupling regime between LSPR and guided modes has been termed as waveguide-plasmon polariton [127–129], while the weak coupling regime is termed as quasi-guided modes. The term quasi means that the mode is leaking to the far field.

We should mention that quasi-guided modes have been successfully employed to enhance the absorption of thin film solar cells [130–132]. Coupling the incident solar light to guided modes in amorphous silicon enhances the optical path length in the solar cell ed increases the cell efficiency.

5.2.1 Approximated dispersion relations for quasi-guided modes and surface lattice resonances

Let us consider the general case of a 2D array of nanoparticles in proximity of a waveguide layer. Light is incident from a medium described by the refractive index n_1, while the waveguide layer is described by the refractive index n_2. The diffraction of light by such an array is described by the conservation of the parallel momentum of the light to the surface of the array

$$\mathbf{k_{out,||}} = \mathbf{k_{in,||}} + \mathbf{G}, \tag{5.1}$$

where $\mathbf{k_{in,||}}$ and $\mathbf{k_{out,||}}$ are the projections on the plane of the array of the incident and diffracted wave vector, respectively. $\mathbf{G} = \frac{2\pi}{a}(m_1, m_2)$ is the reciprocal lattice vector with a the lattice constant for a square array and $m_1, m_2 = 0, \pm 1, \pm 2, ...$ represent a particular diffracted order corresponding to the two dimensions of the reciprocal space. From Eq. (5.1) we obtain the angle of diffraction of the light, θ_d, as

$$\sin^2 \theta_d = \left(\frac{\lambda_0}{n_2 a} m_1 \right)^2 + \left(\frac{n_1}{n_2} \sin\theta + \frac{\lambda_0}{n_2 a} m_2 \right)^2, \tag{5.2}$$

where θ is the angle of incidence and λ_0 is the incident wavelength. In the geometrical optics treatment, the condition for the excitation of a waveguide mode can be written

as [57]

$$2\frac{2\pi}{\lambda_0}n_2 L\cos\theta_d - \phi_{tot}(n_1,n_2,n_3,\theta_\mathrm{d}) = 2Z\pi, \tag{5.3}$$

where L is the thickness of the layer, Z is an integer, n_3 is the refractive index of the substrate and $\phi_{tot}(n_1,n_2,n_3,\theta_\mathrm{d})$ is the phase shift upon total internal reflection in the waveguide layer. Equations (5.2) and (5.3) tell us that it is possible to excite quasi-guided modes propagating in the direction parallel and perpendicular to the polarization vector of the incident light by properly setting (m_1,m_2).

In the case in which the array of nanoparticles is homogeneously surrounded, i.e., $n_1 = n_2 = n$, $\theta_\mathrm{d} = 90°$ and the polarization of the incident light is along the periodicity axis associated with m_1, Eq. (5.1) gives the conditions for RAs (diffracted orders in the plane of the array)

$$k_{\mathrm{out},||}^2 = k_{\mathrm{in},||}^2 + m_1^2\left(\frac{2\pi}{a}\right)^2 + m_2^2\left(\frac{2\pi}{a}\right)^2 + 2k_{\mathrm{in},||}m_1\frac{2\pi}{a}, \tag{5.4}$$

with $k_{\mathrm{in},||} = \frac{2\pi}{\lambda_0}n\sin\theta$. Equation (5.4) describes the angular and spectral dispersion of the SLRs in the case of weak coupling between the LSPR and the RAs. The dispersion and linewidth of the SLRs can be tuned by geometrical design of the particle and lattice [133, 134].

The simultaneous excitation of quasi-guided modes and SLRs in the same device has been observed for the first time by Murai and coauthors in Ref. [135]. This coexistence is non-trivial since quasi-guided modes and SLRs require different photonic environments: quasi-guided modes need a waveguide with a higher refractive index than the surrounding, while SLRs are favored when the medium surrounding the array is homogeneous [136].

In the next sections we will analyse the role of hybrid plasmonic-photonic modes in enhancing the absorption in a plasmonic graphene-based photodetector.

5.3 Plasmonic photodetector design

We design our graphene-based photodetector such that the spatial distribution of the enhanced electric field overlaps with the photoactive layer of graphene. The design of the device is schematically shown in Fig. 5.1 and consists of a substrate, an array of nanoparticles and a layer with a designed thickness and refractive index, which serves as a waveguide and as a spacer to position the photoactive material in proximity of the maximum electric field enhancement. A monolayer of graphene is placed on top of the waveguide. The graphene is capped with a transparent upperlayer made of a material with a refractive index similar to the one of the substrate. Upon light absorption electron-hole pairs are created in the graphene layer which can be separated through a voltage applied across the metallic contacts.
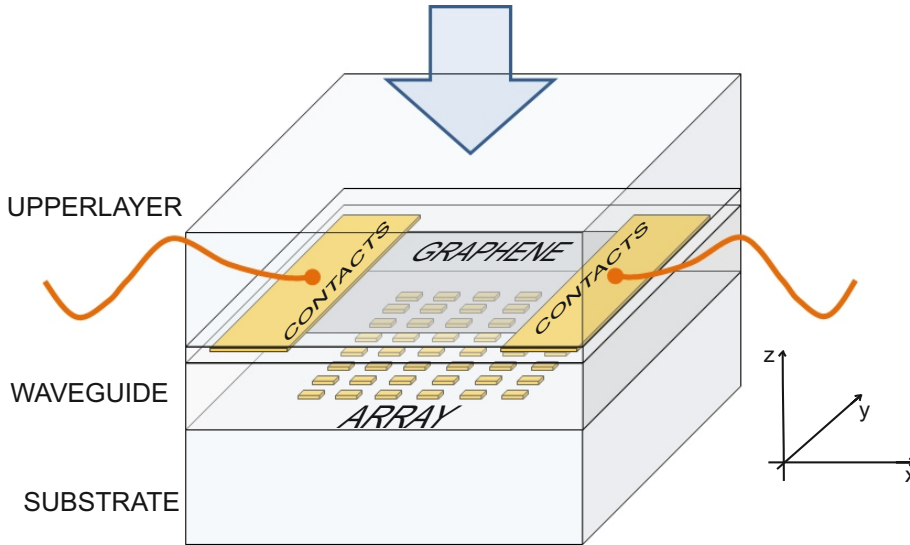
Figure 5.1: Schematic representation of the device. An array of nanoparticles is embedded between a substrate and a waveguide layer. A graphene layer is placed on top of the waveguide layer and the stack is capped with an upperlayer. Metal contacts are used to extract the photocurrent. Light is impinging from the top.

In the rest of the chapter we will simulate and measure the extinction of this device, which represents the first optical characterization of our plasmonic graphane-based photodetector.

5.3.1 Simulations

In this section we present simulations of the optical extinction of the multilayer stack described previously. We also show the spatial distribution of the electric field corresponding to the hybrid plasmonic-photonic modes, which determines the enhanced absorption in the graphene layer.

Three-dimensional electromagnetic simulations were performed with the finite-difference in time-domain method (FDTD). The refractive index of the substrate, spacing layer and upperlayer are $n_1 = 1.46$, $n_2 = 1.52$ and $n_3 = 1.41$ respectively. As we will see in the next section, these values correspond to the materials that we will use in the realization of the device, i.e. quartz, a UV-curable polymer and PDMS, respectively. A plane wave is impinging at normal incidence from the upperlayer side. The graphene layer is modeled using the permittivity derived from the expression for the AC conductivity reported in Ref. [137]. We use a temperature $T = 300$ K, a relaxation time τ=100 fs and a Fermi energy of 300 meV, as commonly accepted in literature [137]. We propose a square array of aluminum particles with a base of 100 nm x 100 nm, a height of 40 nm and lattice constant

of 400 nm. The particles are modeled using the dispersive permittivity of aluminum. A small height of the particles has been chosen to minimize retardation effects that can arise from a phase difference of the excitation wave between the top and the bottom of the particle.
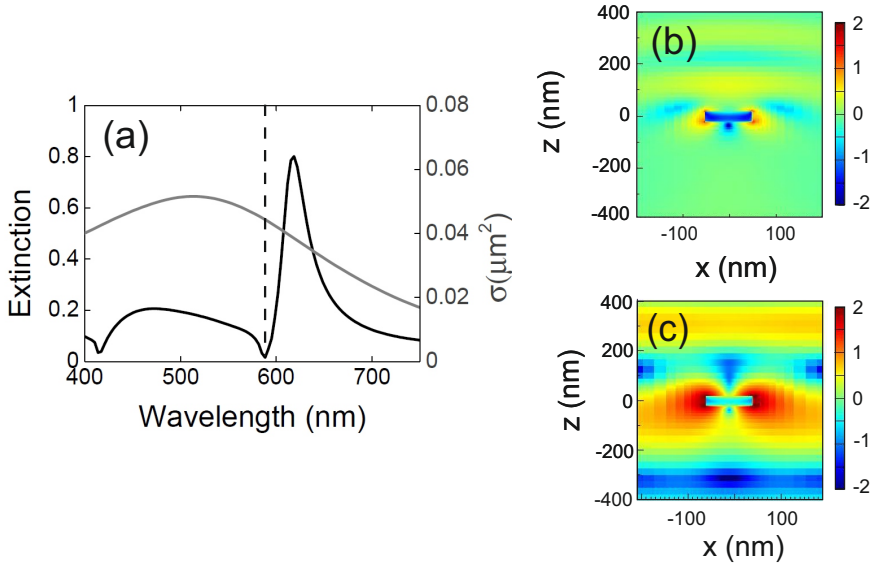

Figure 5.2: (a) FDTD simulations of the scattering cross section spectrum (σ, right axes) of an aluminum particle (100x100x40 nm^3) embedded in a homogeneous medium with a refractive index of 1.46 (grey curve). FDTD simulated extinction spectrum at normal incidence of the same nanoparticle ordered in a square array with a lattice constant of 400 nm (black curve). The dashed line corresponds to the Rayleigh anomaly calculated for the ($\pm$ 1, 0) and (0, $\pm$ 1) beams diffracted in a medium with a refractive index of 1.46. (b) FDTD simulations of the spatial distribution of the total electric field intensity enhancement in logarithmic scale of the isolated nanoparticle at the wavelength of 541 nm and (c) of the square array of nanoparticle at a wavelength of 618 nm. In (b) and (c) the field is calculated at the plane intersecting the nanoparticles in its center (i.e., at y = 0).

We start investigating the optical response of an individual aluminum particle and of an array of them embedded in a homogenous environment. These simulations are performed using two different techniques. For the individual particle we calculate the scattering cross section using the total field-scattered field source [138]. A simulation box size of 1x1x1 μm^3 with perfectly matched layer conditions on every boundary was used. Frequency-domain transmission monitors were positioned in the scattered field region. The mesh grid was set to 5 nm over the entire simulation volume, with a refinement of 1 nm over the volume occupied by the nanoparticle. The nanoparticle is considered to be embedded in a homogeneous medium with a refractive index of 1.46. In contrast, to calculate the transmittance of the periodic array, the simulation box size was equal to a x a x 1 μm^3 and periodic boundary conditions were used in the directions of the plane containing the array. The transmittance spectrum at normal incidence was calculated

with a frequency-domain transmission monitor using the same excitation wave as in the case of the single particle. In both cases the light source is a broadband (450-750 nm) short pulse x-polarized planar wavefront, illuminating at normal incidence the plane of the particle.

Figure 5.2(a) shows the scattering cross section, σ, as a function of the free-space wavelength for an isolated aluminum particle (grey curve), which displays a broad LSPR centered at 541 nm. The black curve represents the extinction spectrum of the array of nanoparticles, defined as one minus transmittance (T). When the nanoparticles are arranged in a periodic lattice a sharp and intense peak at 618 nm emerges in the extinction spectrum, redshifted with respect to the RA of the degenerated $(m_1, m_2) = (\pm 1, 0)$ and $(0, \pm 1)$ diffracted orders (calculated using Eq. (5.4) and indicated by a vertical dashed line in Fig. 5.2(a)). This peak is associated with the coupling of the LSPR of the single particles with the RAs. The small feature in extinction at 413 nm corresponds to the RA associated with the diffracted order $(1, -1)$.

To explore better the nature of the plasmonic resonances we show in Fig. 5.2(b) and (c) the spatial distribution of the total electric field intensity enhancement in logarithmic scale for the case of the isolated particle illuminated with a wavelength of 541 nm and for the case of the array illuminated with a wavelength of 618 nm, respectively. For these simulation a three dimensional frequency-domain field monitor containing the unit cell was used. The field is plotted along the plane cross-cutting the nanoparticle in its center (i.e., at y=0). In Fig. 5.2(b) the field is confined at the edges of the nanoparticle as expected for a LSPR. In Figure 5.2(c) the field intensity extends away from the nanoparticle in the surrounding medium, in agreement with the interpretation that the associated peak originates from the coupling of LSPRs supported by the individual nanoparticles to diffracted orders propagating in the plane of the array (SLRs).

As shown in Fig. 5.1, the graphene layer is placed at a finite distance in the vertical direction respect to the plane of the array. In order to maximize the interaction of light with graphene we need a distribution of the electric field which resembles the 2D geometry of the graphene. Therefore the distribution of the electric field intensity associated with the peak at 618 nm is not suitable for our purposes, as it is not spatially homogenous neither in the x nor in the y direction and it does not extend in the z direction.

To enhance the electric field intensity above the plane of the particles we can make use of the quasi-guided modes resonances introduced in the Section 5.2. A waveguide mode allows the light to propagate in the direction parallel to the plane of the array and therefore appears as a convenient choice to enhance light absorption in graphene in our device.

To allow the excitation of quasi-guided modes, we add a layer with refractive index equal to 1.52 (larger than the refractive index of the substrate) on top of the particle array. To complete the waveguide structure we add on top of the graphene layer a semi-infinite medium with a refractive equal to 1.41, lower than the one of the waveguide layer.
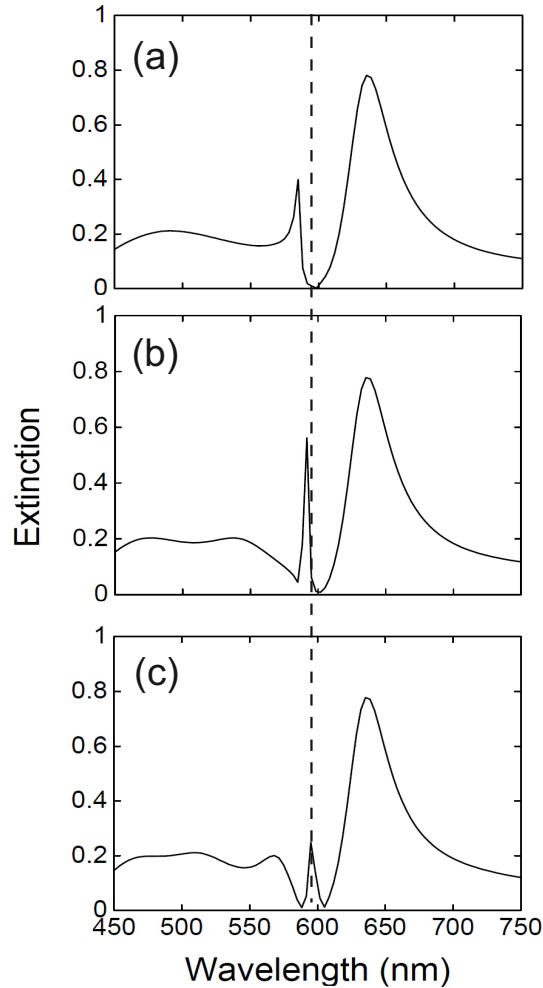
Figure 5.3: (a) FDTD simulated extinction spectra at normal incidence of the system formed by the substrate, the array of nanoparticles, the waveguide layer and the upperlayer for different thicknesses of the waveguide layer: (a) 400 nm, (b) 600 nm, (c) 800 nm. The dashed line highlights the redshift of the sharp peak centered around 580 nm.

Figure 5.3 displays the simulated extinction for different thicknesses of the waveguide layer. An additional sharp peak appears around λ_0=580 nm, with respect to the case without guiding layer. We see that there is a value of the thickness which maximizes the extinction peak and that the peak redshifts as the thickness increases. We associate this sharp peak to a quasi-guided mode. The influence of the thickness of the waveguide layer on the excitation efficiency of the quasi-guided mode can be qualitatively understood in
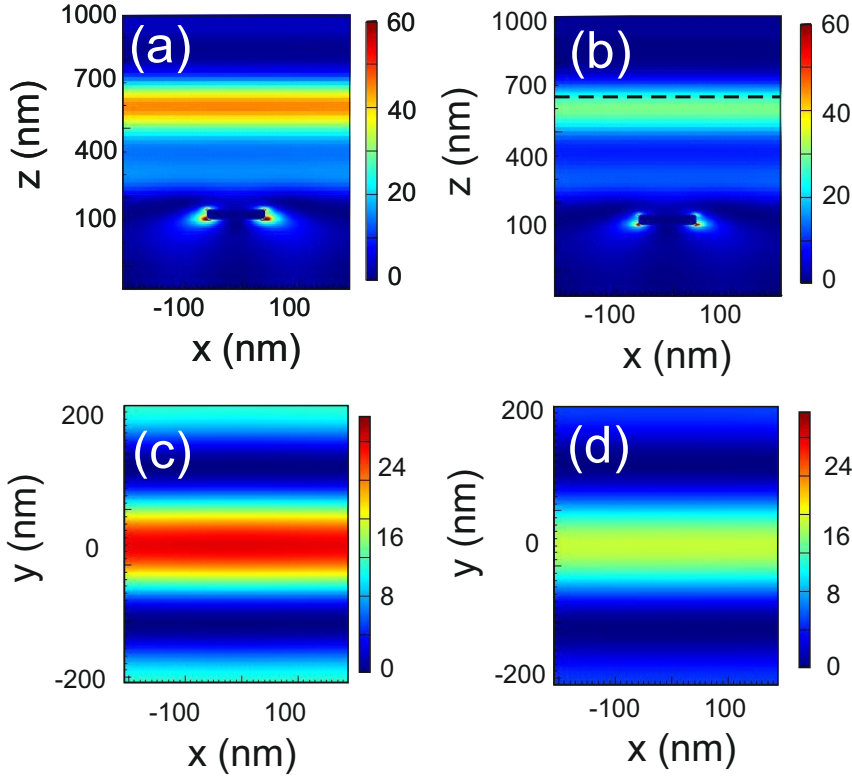
Figure 5.4: (a) FDTD simulated spatial distribution of the total electric field intensity enhancement for the system simulated in Fig. 5.3(b). The simulation considers a plane wave incident normal to the array with a wavelength of 584 nm. The color plot indicates the intensity enhancement in the plane intersecting the nanoparticle along its center, i.e., at $y = 0$, in a unit cell of the array. (b) As in (a) but with a layer of graphene positioned between the waveguide layer and the upperlayer (black dashed line). (c) and (d) display the cut along the x - y plane of the total electric field intensity in the structure without and with graphene, respectively.

terms of field overlap between the two bare states, i.e., LSPR and waveguide mode. For small values of the thickness of the layer the field of the guided mode is poorly confined and a significant fraction of its energy lies outside the waveguide, making the coupling with the LSPR weak. On the other hand when the layer is very thick, the field of the guided mode is well confined in the middle of the layer, relatively far from the nanoparticles, again making the coupling weak. The redshift of the peak as we increase the thickness can be explained by noticing that the thickness and the wavelength appear as a ratio in Eq. (5.3).

In Fig. 5.4 we show the spatial field distribution in the multilayer structure in the case in which one layer of graphene is present on top of the waveguide layer with respect to the

case in which the structure lacks graphene. In Fig. 5.4(a) we plot the spatial distribution of the intensity enhancement (with respect to the structure without particles) of the total electric field in the $x - z$ plane intersecting the nanoparticle along its center, at the wavelength of 584 nm. The thickness of the waveguide layer is 600 nm and the graphene layer is not present in the multilayer structure. We see that a homogeneous band of high field intensity appears in the high refractive index layer along the x-direction. The maximum of the intensity of the electric field is displaced respect to the middle plane of the waveguide layer as a result of the asymmetric structure of the waveguide and the presence of the metallic particles. The simulation in Fig. 5.4(b) is equivalent to (a) in the case in which a layer of graphene is present on top of the waveguide. Adding the graphene layer introduces a perturbation in the system which reduces the intensity of the enhancement from 40 to 30. The spatial distribution of the intensity enhancement of the total electric field in the $x - y$ plane at value of the z-coordinate corresponding to the position of the graphene layer, is plotted in Figs. 5.4(c) and (d) for the multilayer structure without and with graphene, respectively. We see that the intensity of the electric field is modulated along the y-direction: when the incident x-polarized light is scattered by the array of nanoparticles it couples to the quasi-guided modes propagating along the positive and the negative y-direction, which form a standing wave. These propagation directions are described by $(m_1, m_2) = (0, \pm 1)$ in Eq. 5.2. Since the array of nanoparticles is the coupling element for the incident light to these quasi-guided modes, we also find an enhancement of the field at the corners of the nanoparticle. The maximum enhancement factor, calculated with respect to the incident intensity, is around 40. This suggests that by placing the graphene layer in that position, the graphene will benefit from the aforementioned field intensity enhancement and its absorption will increase. Moreover, since the graphene is a 2D material, it will experience the enhancement over its full length along x.

We can calculate the absorbed power by the graphene as a function of the wavelength normalized by the incident power by integrating the electric field intensity in the graphene layer. The result is shown in Fig. 5.5. As expected, we see that the peaks correlate with the position of the resonances in Fig. 5.3(b). In particular, for the resonance of interest (584 nm) we calculate an enhancement factor of the absorption up to 7, which should translate into a similar enhancement factor of the photocurrent extracted from the device. However, this proportionality can be limited by scattering. A way to circumvent this problem is to reduce the dimensions of the device and in particular the distance between the metal contacts.

5.4 Problems overcome with the suggested design

In this section we summarize the problems of a typical graphene-based photodetector that our design contributes to solve.

1. The interaction of light with 2D materials is limited due to their atomic thickness. For example a single layer of graphene absorbs only 2.3% of the light. Increasing the thickness of these materials by stacking them, leads to an increased interaction, e.g. bilayer graphene absorbs 4.6%, but moving away from the 2D character towards the bulk 3D material also removes the unique properties of the 2D phase. Graphene loses its high mobility (high frequency operation), when going from 1 to more layers, unless turbostratic deposition is employed (see Chapter 3). Our proposed device enhances the field at a position displaced from the particle array leaving complete freedom for the design of the 2D crystal heterostructure layout at the region of enhanced field intensity. Similarly, other thin layers, e.g. containing quantum dots, can benefit from the increased field interaction.

2. Typically, plasmonic metallic nanoparticles are used to locally enhance the electric field at the location of the nanoparticle. Although this leads to a strong enhancement of the field, it is only very local to the particle and a large area around the particle does not benefit from the enhancement. In our scheme we homogeneously enhance the electric field intensity by a factor of 20 (see Fig. 5.4(b)), several hundreds of nanometers above the particles.

Besides the waveguiding effect described in the previous section, the waveguide layer also helps in planarizing the surface on top of which the graphene is deposited. In other works the graphene layer is deposited directly on top of the particle array [120, 139]. This introduces many defects because the graphene follows conformally the surface on top of which it is deposited.
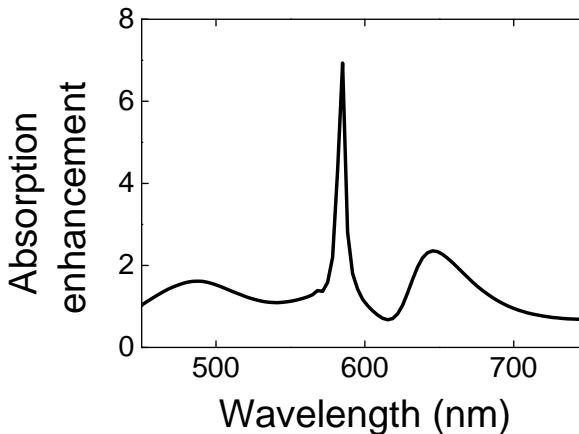

Figure 5.5: Absorption enhancement in the graphene layer positioned as in Fig. 5.4(c) as a function of the wavelength.

3. Graphene is a broadband absorber that lacks spectral specificity. An additional advantage of the nanoparticle array is that the materials used allow to select the range of interest of the electromagnetic spectrum (aluminium particles can be used for the visible spectrum and gold particles for the IR spectrum), while its design can be tuned to select specific wavelengths.

4. The particle array allows also for a potentially further tunability, which stems from the angular dispersion of the optical resonances supported by the array. Because of this angular dispersion it could be possible to reconfigure the application of the same device by only varying an external parameter such as the angle of incidence of the light on the device. However, in this way the spatial field distribution will also be affected and its homogeneity at the location of the graphene layer might change. Therefore, further investigation on the dependence of the spectrum of the absorption enhancement as a function of the angle of incidence is needed.

The layout described above is not limited to graphene and can be applied to other nanometer thin materials such as 2D crystals (e.g. transition metal dichalcogenides), quantum dots and stacks thereof to increase their interaction with light for photodetection or other optoelectronic application.

Our proposed device can be seen as a microcavity defined by the interfaces of the waveguide layer, in which a graphene layer is embedded. We could therefore wonder which advantages our configuration presents with respect to a canonical microcavity in which a graphene layer is placed in a location of maximum electric field. Such devices have been realized by Engel and coauthor using two silver mirrors [93] and by Furchi and coauthors using Bragg reflectors [92]. These cavities support Fabry-Perot modes which allow enhancing the light-matter interaction and achieving experimental values of absorption up to 50%. The Q-factors achieved are 20 and 80, respectively. The Q-factor of our device at the resonant wavelength is around 100 (see Fig. 5.3 and Section 5.5). Theoretically a microcavity defined by two Bragg mirrors can be tuned to achieve 100% absorption in the graphene layer at a very specific wavelength and angle of illumination if the reflectivity of the two mirrors is very high [140]. However, this requires a very high quality in the fabrication of the multistack which can be formed by over twenty pairs of layers of very well defined thickness and refractive index. Any small deviation from the ideal case will lead to a decrease in the optical absorption in the graphene because it pronouncedly affects the reflectivity of the mirrors. Besides, there is also a trade-off between the amount of absorption and the width of the resonance [140]. On the contrary, our device, exploits a waveguide mode which requires only one layer, i.e. the waveguide layer, and a coupling element (the particle array) to couple the incident light in. As we will see in the next section, the array can be fabricated with conformal imprint lithography with nanometer resolution and on a large scale, while the thickness of the waveguide layer can be controlled very easily during the spin-coating. Total absorption in the graphene layer is prevented by the absorption in the metallic particles, however this should not be seen only as a limitation, but also as a technological advantage because it implies a

broadening of the resonances and therefore an ease incoupling. With regard to the angular sensitivity, both the conventional microcavity-enhanced photodetector and our approach are sufficiently insensitive to small misalignments. Typically a range of 5 degrees does not affect significantly the performances of the detector [140].

The most striking difference between a two-dimensional cavity and our structure relies on the tunability of the angular-spectral dispersion relation of the resonances. In the first case, the dispersion is a parabola which can be hardly tuned by acting on the refractive index of the medium in which the graphene is embedded. Our approach provides far more degrees of freedom to control the dispersion relation of the resonances. For instance, control can be achieved by designing the geometrical parameters of the nanoparticles, the pitch of the array, the thickness and the refractive index of the waveguide layer.

5.5 Preliminary experimental results

In the previous sections we have described the design of a plasmonic graphene-based photodetector and we have simulated the hybrid photonic-plasmonic modes supported by the multilayer structure. Here, we present the first experimental steps towards the realization of this device.

A square array of aluminum nanoparticles with a base of 100 nm x 100 nm, a height of 40 nm and a lattice constant of 400 nm is fabricated on a quartz substrate by nanoimprint lithography in combination with reactive ion etching (RIE). On top of the array a waveguide layer of UV-curable polymer (NOA 61) has been spin-coated. Its thickness, measured by profilometer, equals 570 nm. On top of the polymer layer we deposit a monolayer of graphene. The waveguide layer minimizes the presence of the defects in the deposition of the graphene layer, since the surface of operation is flat
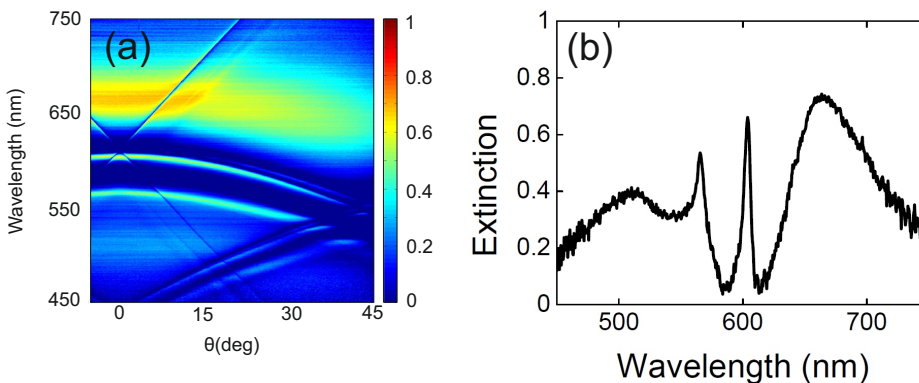

Figure 5.6: (a) Extinction measurements as a function of the wavelength and of the angle of incidence of the device schematically shown in Fig. 5.1 illuminated with p-polarized light. (b) Cut at normal incidence of the extinction in shown in (a).
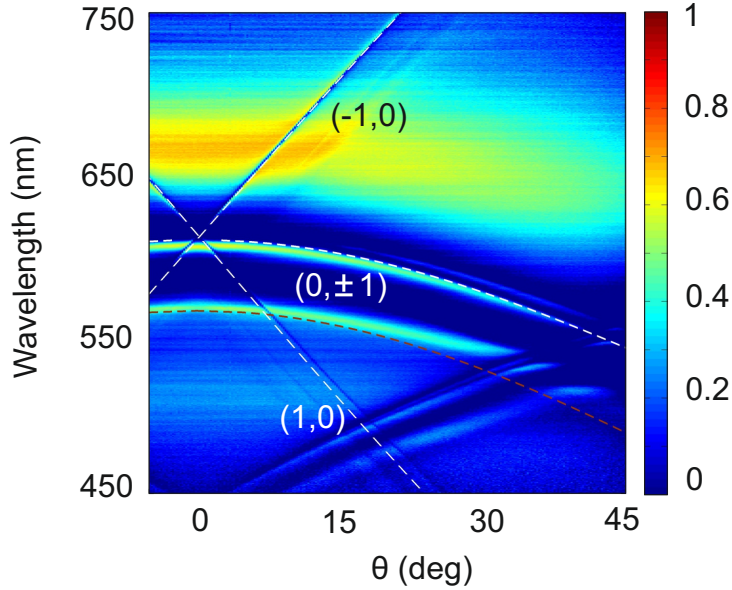
Figure 5.7: Extinction measurements shown in Fig. 5.6(a) plotted as a function of the wavelength and of the angle of incidence. Red dashed lines correspond to the $(0,\pm1)$ RAs calculated using the refractive index of the PDMS, i.e., 1.41. White dashed lines represent the eigenmode calculation for the dispersion relation of the TM_0 guided mode calculated assuming a three layer system formed by two semi-infinite layers with refractive index 1.46 (quartz substrate) and 1.41 (PDMS) and a 570 nm-thick layer characterized by a refractive index of 1.56 (UV-curable polymer).

instead of being corrugated by the presence of the particles. Graphene has been grown by CVD deposition on copper by the company Graphenea [141]. The graphene layer (1 cm x 1 cm) has been transferred to the UV-curable polymer. The transfer is conducted by spin-coating a thin (200 nm) polymeric layer of poly(methylmethacrylate) (PMMA) on top of the graphene. This polymer provides a supportive framework for graphene before the transfer. The underneath copper substrate is then etched away by iron chloride ($FeCl_3$) solution [99] and the graphene is deposited on the device and positioned in such a way that it covers the whole array of nanoparticles. Gold contacts (30 nm thick) are evaporated on 5 nm of titanium, which is used to facilitate the bond of the gold to the graphene layer. The stack is capped by a thick PDMS layer, which adheres by van der Waals interactions and follows the surface conformally. This layer can be easily removed without affecting the graphene layer.

Figure 5.6(a) shows extinction measurements of the device as a function of the wavelength and of the angle of incidence when illuminated with p-polarized light. Figure 5.6(b) shows a cut at normal incidence of the extinction. By comparing this figure with Fig. 5.3(b) we see that the peaks are qualitatevely well predicted by the simulation. Figure 5.6(a) shows

a broad slightly angular dependent resonance and few angular dispersive sharp lines. To correlate these features with the resonances described so far, in Fig. 5.7 we plot the Rayleigh anomalies associated to the light propagating in the upperlayer and the dispersion relation of the fundamental TM guided modes supported by the layer of UV-curable polymer. The red dashed line corresponds to the $(0,\pm1)$ RAs calculated using the refractive index of the PDMS, i.e., 1.41. The white dashed lines represent the eigenmode calculation [see Eq. (5.3)] of the TM_0 guided mode. This calcualtion is performed assuming a three layer system formed by two semi-infinite layers with refractive index 1.46 (quartz substrate) and 1.41 (PDMS) and a 570 nm-thick layer characterized by a refractive index of 1.56 (UV-curable polymer). The refractive index for the waveguide layer used in the calculation is slightly higher than the nominal one (1.52). This modification can be qualitatively explained by considering the presence of the metallic particles in the layer. As described in Section 5.2.1 we find guided modes propagating along the direction described by the diffracted orders $(\pm1,0)$, and $(0,\pm1)$.

We notice that the dispersion of the $(0,\pm1)$ order quasi-guided mode does not depend strongly on the angle of incidence for angles smaller than 10 degrees (see Fig. 5.7). From the technological point of view this means that our photodetector will not be extremely sensitive to the alignment. On the other hand for angles larger than 10 degrees, we can consider the dispersion of the resonance as an advantage for our device, because it allows the photodetector to be reconfigurable, i.e. sensitive to different wavelengths depending on how we align the system.

The feature around 530 nm in Fig. 5.6(b), associated with the $(0,\pm1)$ RA propagating in the PDMS layer, is more pronounced in the measurement with respect to the simulation. This can be due to a small deviation of the experimental optical constants with respect to the one used in the simulation.

5.6 Conclusions and outlook

In this chapter we have presented a design for a graphene-based photodetector which combines a metallic array of nanoparticles with a monolayer of graphene. The novelty of our design lies in the use of collective resonances arising from the radiative coupling of localized plasmon resonances. The layer of graphene is deposited on top of an intermediate layer acting as a waveguide and as a spacer. The coupling of the aforementioned resonances leads to hybrid plasmonic-photonic modes. We calculate that one of these modes allows for an enhancement of the optical absorption of the graphene up to a factor of 7, which should translate into a proportional enhancement factor of the photocurrent. The photocurrent can be measured by standard IC circuitry. The advantage of the device stems from an improved spatial homogeneity of the electric field intensity along a specific direction, which is beneficial for the interaction with a 2D material.

The absorption enhancement we predict in this chapter is comparable to the one we measured in Chapter 4. In that chapter the enhanced light absorption was caused by the destructive interference in the far field of the scattered waves, which results in waveguiding in the proximity of the graphene layers. In this chapter we excite a guided mode weakly coupled to localized plasmon resonances, again propagating in the proximity of the graphene layer. The potential of the approach presented in this chapter lies in the possibility of achieving the strong coupling regime by properly designing the detuning and the field overlap of the localized plasmon resonance of the single nanoparticle with the guided modes sustained by the spacing layer [129]. This regime is interesting because it enables to significantly modify the optical properties of the participant modes, thus creating a system with intermediate properties of those of its bare states. Moreover, the transparency window in extinction, consequence of the strong coupling regime, minimizes the absorption loss of the incident light in the metallic particles, while allowing a strong near field interaction [129].

By replacing the PDMS with a quartz (or another material with the same refractive index) it is possible to enhance even further the electric field intensity at the location of the graphene layer. The calculated enhancement that we can achieve with this configuration is 13. To simplify the fabrication process of the device described in this chapter, the graphene layer is positioned on top of the waveguide, therefore not at the location of the maximum of the electric field intensity. By depositing the UV-curable polymer in multiple steps, it is possible to position the graphene layer in the middle of the waveguide layer and profit even more from the region of the enhanced electric field. By microstructuring the graphene and the contacts it is possible to reduce the path that the photogenerated carriers travel before reaching the contacts. In this way it is possible to reduce the scattering and the recombination of the electron-hole pairs giving rise to the photocurrent and, therefore, increase the signal. Typical dimensions of the graphene layer are on the order of few hundreds microns squared.

Additional tunability of the device can be created by adding a gate to tune the Fermi energy in the graphene layer. A possible layout, with minor influence to the operation of the stack, would consist in using as a gate another graphene layer located few hundreds nanometer away from the first one. A bias voltage on this layer can modify the Fermi energy in the detection layer thereby tuning it to the most interesting range.

APPENDIX A

THIN YAG:CE FILM FABRICATION

Gel films were prepared by an epoxide-catalyzed sol-gel process [142–145], modified by the addition of a water-soluble polymer to obtain a homogeneous and continuous layer [146]. $YCl_3 \cdot 6H_2O$, $AlCl_3 \cdot 6H_2O$, and $CeCl_3 \cdot 7H_2O$ were utilized as sources of yttrium, aluminum, and cerium, respectively, in a mixture of distilled water and ethanol as a solvent. Propylene oxide (PO) was added to initiate the condensation reaction, and poly(vinyl pirroridone) (PVP), having viscosity-averaged molecular weight of 40.000, was used as a water-soluble polymer.

Nominal composition of the gel was $(Y_{0.95}Ce_{0.05})_3Al_5O_{12}$, i.e., 5 mol% of Y^{3+} was replaced by Ce^{3+}. The gel preparation is as follows: First, $AlCl_3 \cdot 6H_2O$ (0.56 g), $YCl_3 \cdot 6H_2O$ (0.40 g), $CeCl_3 \cdot 7H_2O$ (0.026 g), and PVP (0.10 g) were dissolved in a mixture of water (2.71 g) and ethanol (1.69 g). PO (0.70 g) was then added to the transparent solution under ambient conditions (25°C). After stirring for 2 min, the resultant homogeneous solution reacted during 30 min. Next, several drops of the transparent sol were dispensed on the substrate (fused silica glass or sapphire) and spin-coated at 2000 rpm during 60 sec. The coated substrates were baked stepwise at 80°C for 30 min, 200°C for 30 min, and 300°C for 30 min. After that, the films were heated at temperatures 600-1600°C in air for 1 h, and then further heated at the same temperature in a gas mixture of 5% H2/ 95%N2 for 1 h.

TRANSFER MATRIX METHOD

A transfer-matrix method for isotropic layered media is used for modeling the reflectance and transmittance of planar structures. In this Appendix we explain this method, following the description of Ref. [57]. We use this technique to calculate the reflectance and the transmittance of a multilayer structure formed by dispersive media (QDs, YAG:Ce, graphene).
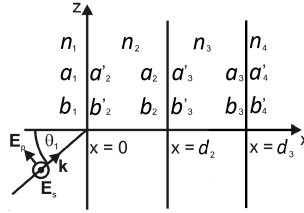
Figure B.1: A four-layer system consisting of four materials with refractive indices n_1, n_2, n_3, and n_4, respectively. The field amplitudes at the interfaces are given by a_1, a'_2, a_2, a'_3, a_3, a'_4 for the right traveling waves and b$_1$, b'$_2$, b$_2$, b'$_3$, b$_3$, b'$_4$ for the left traveling wave. The incident light beam with the wavevector **k** and the angle of incidence θ_1 is defined in medium 1.

Let us consider a four-layer system as the one in Figure B.1. The electric field of an electromagnetic plane wave of angular frequency ω propagating with the z-component of the wave vector k_z in the xz plane is given by

$$\mathbf{E} = \mathbf{E}(x)e^{i(\omega t - k_z z)}. \tag{B.1}$$

For a detailed derivation of each component of the field see Ref. [147]. We assume that the light is linearly polarized, either $s-$polarized, i.e., **E** parallel to y or $E_x = E_z = 0$, or $p-$polarized, i.e., **H** parallel to **y** or $E_y = 0$. If we assume that light is only incident on the

four-layer system from the left, i.e., medium 1, the electric field in layer 1, 2 and 3 consists of a right- and left-traveling wave and can be written as

$$E(x) = a\mathrm{e}^{-ik_\mathrm{x}x} + b\mathrm{e}^{ik_\mathrm{x}x} \equiv a(\mathrm{x}) + b(\mathrm{x}), \tag{B.2}$$

where $\pm k_\mathrm{x}$ are the x-components of the wave vector given by $k_\mathrm{x} = n_\alpha \frac{2\pi}{\lambda} \cos\theta'_\alpha$ in medium α with refractive index n_α and angle inside the medium θ'_α. The amplitudes a and b are constant in each homogeneous layer. The amplitude of the wave traveling to the right is represented by $a(\mathrm{x})$, while the left traveling component is described by $b(\mathrm{x})$. We define the various amplitudes at the interfaces between the different media as

$$
\begin{aligned}
a_1 &= a(0^-), \\
b_1 &= b(0^-), \\
a'_2 &= a(0^+), \\
b'_2 &= b(0^+), \\
a_2 &= a(d_2^-), \\
b_2 &= b(d_2^-), \\
a'_3 &= a(d_2^+), \\
b'_3 &= b(d_2^+), \\
a_4 &= a(d_3^-), \\
b_4 &= b(d_3^-) \\
a'_4 &= a(d_3^+), \\
b'_4 &= b(d_3^+) = 0,
\end{aligned}
\tag{B.3}
$$

where 0^- represents the left side and 0^+ the right side of the interface at $\mathrm{x} = 0$. Similarly, d^- and d^+ represent the left and right side of the interface at $\mathrm{x} = d$ (see Fig. B.1). If we represent the left and right traveling components of the electric field as column vectors, the vectors at each side of the interface are related by

$$\begin{pmatrix} a_1 \\ b_1 \end{pmatrix} = \mathbf{D}_{1,2} \begin{pmatrix} a'_2 \\ b'_2 \end{pmatrix}, \tag{B.4}$$

$$\begin{pmatrix} a'_2 \\ b'_2 \end{pmatrix} = \mathbf{P}_2 \begin{pmatrix} a_2 \\ b_2 \end{pmatrix}, \tag{B.5}$$

$$\begin{pmatrix} a_2 \\ b_2 \end{pmatrix} = \mathbf{D}_{2,3} \begin{pmatrix} a'_3 \\ b'_3 \end{pmatrix}, \tag{B.6}$$

$$\begin{pmatrix} a'_3 \\ b'_3 \end{pmatrix} = \mathbf{P}_3 \begin{pmatrix} a_3 \\ b_3 \end{pmatrix}, \tag{B.7}$$

$$\begin{pmatrix} a_3 \\ b_3 \end{pmatrix} = \mathbf{D}_{3,4} \begin{pmatrix} a'_4 \\ b'_4 \end{pmatrix}, \tag{B.8}$$

where $\mathbf{D}_{1,2}$, $\mathbf{D}_{2,3}$ and $\mathbf{D}_{3,4}$ are the so-called transmission matrices and $\mathbf{P}_2$ and $\mathbf{P}_3$ are the propagation matrices that accounts for the propagation in the layers. The matrices are defined for layer α as follows

$$\mathbf{D}_{\alpha,\alpha+1} = \frac{1}{t_{\alpha,\alpha+1}} \begin{pmatrix} 1 & r_{\alpha,\alpha+1} \\ r_{\alpha,\alpha+1} & 1 \end{pmatrix}, \tag{B.9}$$

and

$$\mathbf{P}_\alpha = \begin{pmatrix} e^{i\phi_\alpha} & 0 \\ 0 & e^{-i\phi_\alpha} \end{pmatrix}, \tag{B.10}$$

where $t_{\alpha,\alpha+1}$ and $r_{\alpha,\alpha+1}$ are the Fresnel amplitude reflection and transmission coefficients for the interface and $\phi_\alpha = \frac{2\pi}{\lambda} n_\alpha \cos\theta'_\alpha L_\alpha$ is the phase change of light traveling through the layer, with L_α the thickness of the layer, λ the vacuum wavelength, and n_α and θ'_α the refractive index of the layer and the angle inside the layer, respectively.
From Eqs. (B.4)-(B.8), the amplitudes a_1, b_1, and a'_4 and b'_4 are related by the multiplication of the transmission and the propagation matrices

$$\begin{aligned} \begin{pmatrix} a_1 \\ b_1 \end{pmatrix} &= \mathbf{D}_{1,2}\mathbf{P}_2\mathbf{D}_{2,3}\mathbf{P}_3\mathbf{D}_{3,4} \begin{pmatrix} a'_4 \\ b'_4 \end{pmatrix} \\ &= \begin{pmatrix} M_{11} & M_{12} \\ M_{21} & M_{22} \end{pmatrix} \begin{pmatrix} a'_4 \\ b'_4 \end{pmatrix} \\ &= \mathbf{M} \begin{pmatrix} a'_4 \\ b'_4 \end{pmatrix}. \end{aligned} \tag{B.11}$$

The multiplication of the matrices can be represented by the matrix $\mathbf{M}$ consisting of the four elements M_{11}, M_{12}, M_{21}, and M_{22}.
The reflection and transmission of a plane wave through the four-layer structure for light coming from layer 1 are defined as

$$r = \left(\frac{b_1}{a_1} \right)_{b'_4=0}, \tag{B.12}$$

and

$$t = \left(\frac{a'_4}{a_1} \right)_{b'_4=0}, \tag{B.13}$$

respectively. Using Equation (B.11), the amplitude reflection and transmission coefficients of the layered system are given by

$$r = \frac{M_{21}}{M_{11}}, \tag{B.14}$$

and

$$t = \frac{1}{M_{11}}. \tag{B.15}$$

The reflectance R for the case that the medium of layer 1 is lossless is defined as

$$R = |r|^2 = \left| \frac{M_{21}}{M_{11}} \right|^2 . \tag{B.16}$$

If the bounding layers, 1 and 4, are both dielectrics, with real n_1 and n_4, the transmission T for a wave incident with an angle θ_1 is given by

$$T = \frac{n_4 \cos\theta_4'}{n_1 \cos\theta_1} |t|^2 = \frac{n_4 \cos\theta_4'}{n_1 \cos\theta_1} \left| \frac{1}{M_{11}} \right|^2 , \tag{B.17}$$

with θ_4' the angle the light forms with the x axis in the third layer related to θ_1 by Snell's law.

The transfer-matrix method explained above is not limited for four-layer systems. This formalism can be easily expanded for multi-layer structures by multiplying the transmission and propagation matrices for each layer. For any layer it is possible to input the refractive index as a function of wavelength, angle of incidence and polarization.

REFERENCES

[1] J. Strutt, *On the transmission of light through an atmosphere containing small particles in suspension, and on the origin of the blue of the sky,* Philos. Mag. **47**, 375 (1899).

[2] C. F. Bohren and D. R. Huffman, *Absorption and scattering of light by small particles,* John Wiley and Sons, Inc., 1983.

[3] L. D. Landau, *Electrodynamics of Continuous Media,* Pergamon Press, Oxford, 1984.

[4] J. Kim, K. Kim, and S. Kim, *Universal Expression of the Optical Power Dissipation in Multilayer Structures with Complex Permittivity and Permeability,* Jpn. J. Appl, Phys. **51**, 022001 (2012).

[5] W. Wan, Y. Chong, L. Ge, H. Noh, and A. D. Stone, *Time-Reversed Lasing and Interferometric Control of Absorption,* Science **331**, 889 (2011).

[6] H. Raether, *Surface Plasmons on smooth and rough surfaces and on gratings,* Springer-Verlag, Berlin, 1988.

[7] E. Driessen and M. de Dood, *The perfect absorber,* Appl. Phys. Lett. **94**, 171109 (2009).

[8] S. Bandiera, D. Jacob, T. Muller, F. Marquier, M. Laroche, and J.-J. Greffet, *Enhanced absorption by nanostructured silicon,* Appl. Phys. Lett. **93**, 193103 (2008).

[9] N. I. Landy, S. Sajuyigbe, J. Mock, D. Smith, and W. Padilla, *Perfect Metamaterial Absorber,* Phys. Rev. Lett. **100**, 207402 (2008).

[10] A. Yariv, *Universal relations for coupling of optical power between microresonators and dielectric waveguides,* Electron. Lett. **36**, 4 (2000).

[11] A. Yariv, *Critical Coupling and Its Control in Optical Waveguide-Ring Resonator Systems,* IEEE Photon. Technol. Lett. **14**, 4 (2002).

[12] J. Slater, *Microwave electronics,* D. Van Nostrand, Inc., 1950.

[13] B. E. Little, *Ultra compact Si-SiO2 microring resonator optical channel dropping filters*, Opt. Lett. **23**, 1570 (1998).

[14] J. M. Choi, R. K. Lee, and A. Yariv, *Control of critical coupling in a ring resonator–fiber configuration: application to wavelength-selective switching, modulation, amplification, and oscillation*, Opt. Expr. **26**, 1236 (2001).

[15] Y. D. Chong, L. Ge, H. Cao, and A. Stone, *Coherent Perfect Absorbers: Time-Reversed Lasers*, Phys. Rev. Lett. **105**, 053901 (2010).

[16] K. M. Frahm, H. Schomerus, M. Patra, and C. W. J. Beenakker, *Large petermann factor in chaotic cavities with many scattering channels*, Europhys. Lett. **49(1)**, 48 (2000).

[17] D. S. Wiersma, *The physics and applications of random lasers.*, Nat. Phys. **4**, 359 (2008).

[18] F. van Beijnum, P. J. van Veldhoven, E. J. Geluk, M. de Dood, W. Gert, and M. P. van Exter, *Surface plasmon lasing observed in metal hole arrays.*, Phys. Rev. Lett. **110**, 206802 (2013).

[19] I. M. Vellekoop and A. P. Mosk, *Focusing coherent light through opaque strongly scattering media*, Opt. Lett. **32**, 2309 (2007).

[20] I. M. Vellekoop, E. G. van Putten, A. Lagendijk, and A. P. Mosk, *Demixing light paths inside disordered metamaterials*, Opt. Expr. **16**, 67 (2008).

[21] O. Katz, E. Small, and Y. Silberberg, *Looking around corners and through thin turbid layers in real time with scattered incoherent light*, Nat. Photon. **6**, 549 (2012).

[22] J. Bertolotti, E. G. van Putten, C. Blum, A. Lagendijk, W. L. Vos, and A. P. Mosk, *Non-invasive imaging through opaque scattering layers*, Nature **491**, 232–234 (2012).

[23] A. P. Mosk, A. Lagendijk, G. Lerosey, and M. Fink, *Controlling waves in space and time for imaging and focusing in complex media*, Nat. Photon. **6**, 283 (2012).

[24] J. Yoon, K. H. Seol, S. H. Song, and R. Magnusson, *Critical coupling in dissipative surface-plasmon resonators with multiple ports*, Opt. Expr. **18**, 25702 (2010).

[25] J. W. Yoon, G. M. Koh, S. H. Song, and R. Magnusson, *Measurement and Modeling of a Complete Optical Absorption and Scattering by Coherent Surface Plasmon-Polariton Excitation Using a Silver Thin-Film Grating*, Phys. Rev. Lett. **109**, 257402 (2012).

[26] H. Noh, Y. Chong, A. D. Stone, and H. Cao, *Perfect coupling of light to surface plasmons by coherent absorption*, Phys. Rev. Lett. **108**, 186805 (2012).

[27] T. S. Kao, S. D. Jenkis, J. Ruostekoski, and N. I. Zheludev, *Coherent control of nanoscale light localization in metamaterial: creating and positioning isolated subwavelength energy hot spots*, Phys. Rev. Lett. **106**, 085501 (2011).

[28] J. Zhang, K. F. MacDonald, and N. I. Zheludev, *Controlling light-with-light without non-linearity*, Light Sci. Appl. **1**, e18 (2012).

[29] S. Dutta-Gupta, R. Deshmukh, A. V. Gopal, O. J. F. Martin, and S. Dutta Gupta, *Coherent perfect absorption mediated anomalous reflection and refraction*, opt. Lett. **37**, 4452 (2012).

[30] M. Fink, *Time reversal of ultrasonic fields. Part I: Basic principles*, IEEE Trans. Ultrason. Ferroelectr. Freq. Control **39**, 555–566 (1992).

[31] A. Derode, P. Roux, and M. Fink, *Robust acoustic time reversal with high-order multiple scattering*, Phys. Rev. Lett. **75**, 4206–4209 (1995).

[32] S. T. C. Pengjiang Wei, Charles Croënne and J. Li, *Symmetrical and anti-symmetrical coherent perfect absorption for acoustic waves*, Appl. Phys. Lett. **104**, 121902 (2014).

[33] H. Stuart and D. Hall, *Absorption enhancement in silicon-on-insulator waveguides using metal island films*, Appl. Phys. Lett. **69**, 2327 (1996).

[34] H. Atwater and A. Polman, *Plasmonics for improved photovoltaic devices*, Nat. Mat. **9**, 205 (2010).

[35] G. Lozano, T. Barten, G. Grzela, and J. Gomez Rivas, *Directional absorption by phased arrays of plasmonic nanoantennae probed with time-reversed Fourier microscopy*, New J. Phys. **16**, 013040 (2014).

[36] D. M. Schaadt, B. Feng, and E. T. Yu, *Enhanced Semiconductor Optical Absorption via Surface Plasmon Excitation in Metal Nanoparticles*, Appl. Phys. Lett. **86**, 063106 (2005).

[37] N. C. Panoiu and R. M. Osgood, *Enhanced optical absorption for photovoltaics via excitation of waveguide and plasmon-polariton modes.*, Opt. Lett. **32**, 2825 (2007).

[38] A. Aubry, D. Lei, A. Fernandez-Dominguez, Y. Sonnefraud, S. Maier, and J. Pendry, *Plasmonic light-harvesting devices over the whole visible spectrum.*, Nano Lett. **10**, 2574 (2010).

[39] P. Reiss, M. Protire, and L. Li, *Core/Shell Semiconductor Nanocrystals*, Small **5**, 154 (2009).

[40] P. Schlotter, R. Schmidt, and J. Schneider, *Luminescence conversion of blue light emitting diodes*, Appl. Phys. A Mater. Sci. Process. **64**, 417 (1997).

[41] T. Yanagida and *et al*, *Improvement of ceramic YAG(Ce) scintillators to $(YGd)_3Al_5O_{12}(Ce)$ for gamma-ray detectors*, Nucl. Instr. Meth. Phys. Res. A **579**, 23–26 (2007).

[42] W. Chewpraditkul and L. Swiderski, *Scintillation Properties of LuAG:Ce, YAG:Ce and LYSO:Ce Crystals for Gamma-Ray Detection*, IEEE Trans. Nucl. Sci. **56**, 3800 (2009).

[43] M. Kučera, P. Hasa, and J. Hakenová, *Optical and magneto-optical properties of CeYAG*, J. Alloy. Comp. **451(1-2)**, 146–148 (2008).

[44] E. Mihóková, M. Nikl, J. A. Mareš, A. Beitlerová, A. Vedda, K. Nejezchleb, K. Blažek, and C. D'Ambrosio, *Luminescence and scintillation properties of YAG:Ce single crystal and optical ceramics*, J. Lumin. **126(1)**, 77–80 (2007).

[45] S. Herminghaus, M. Klopfleisch, and H. Schmidt, *Attenuated total reflectance as a quantum interference phenomenon*, Opt. Lett. **19**, 4 (1994).

[46] A. Boardman, *Electromagnetic Surface Waves*, Wiley, New York, 1982.

[47] L. Carbone and *et al.*, *Synthesis and micrometer-scale assembly of colloidal CdSe/CdS nanorods prepared by a seeded growth approach*, Nano Lett. **7**, 2942 (2007).

[48] J. W. Kim and Y. J. Kim, *The effects of substrates and deposition parameters on the growing and luminescent properties of $Y_3Al_5O_{12}:Ce$ thin films*, Opt. Mater. **28**, 698 (2006).

[49] W. H. Chao, R. J. Wu, and T. B. Wu, *Structural and luminescent properties of YAG:Ce thin film phosphor*, J. Alloy. Comp. **506**, 98 (2010).

[50] Y. Mizoguchi, M. Kagawa, Y. Syono, and T. Hirai, *Film synthesis of $Y_3Al_5O_{12}$ and $Y_3Fe_5O_{12}$ by the spray–inductively coupled plasma techniqueLuminescence conversion of blue light emitting diodes*, J. Am. Ceram. Soc. **84**, 651 (2001).

[51] G. R. Bai, H. L. M. Chang, and C. M. Foster, *Preparation of single-crystal Y3A15O12 thin film by metalorganic chemical vapor deposition*, Appl. Phys. Lett. **64**, 1777 (1994).

[52] Y. C. Wu, S. Parola, O. Marty, M. Villanueva-Ibanez, and J. Mugnier, *Structural characterizations and waveguiding properties of YAG thin films obtained by different sol-gel processes*, Opt. Mater. **27**, 1471 (2005).

[53] P. Y. Jia, J. Lin, X. M. Han, and M. Yu, *Pechini sol–gel deposition and luminescence properties of Y_3Al_5-xGaxO$_{12}$:Ln^{3+} (Ln3+=Eu^{3+}, Ce3+, Tb^{3+}; 0 = x = 5) thin films*, Thin Solid Films **483**, 122 (2005).

[54] E. Garskaite, M. Lindgren, M. A. Einarsrud, and T. Grande, *Luminescent properties of rare earth (Er, Yb) doped yttrium aluminium garnet thin films and bulk samples synthesised by an aqueous sol-gel technique*, J. Eur.Ceram. Soc. **30**, 1707 (2010).

[55] A. E. Gash, T. M. Tillotson, J. H. Satcher, J. F. Poco, L. W. Hrubesh, and R. L. Simpson, *Use of epoxides in the sol-gel synthesis of porous iron(III) oxide monoliths from Fe(III) salts*, Chem. Mater. **13**, 999 (2001).

[56] A. E. Gash, J. H. Satcher, and R. L. Simpson, *Strong akaganeite aerogel monoliths using epoxides: Synthesis and characterization*, Chem. Mater. **15**, 3268–3275 (2003).

[57] Pochi-Yeh, *Optical waves in layered media*, John Wiley and Sons, New York, 1998.

[58] P. N. Saeta, V. E. Ferry, D. Pacifici, J. N. Munday, and H. A. Atwater, *How much can guided modes enhance absorption in thin solar cells?*, Opt. Express **17(23)**, 20975–20990 (2009).

[59] V. Giannini, Y. Zhang, M. Forcales, and J. Gómez Rivas, *Long-range surface polaritons in ultra-thin films of silicon*, Opt. Express **16**, 19674–19685 (2008).

[60] H. P. Urbach and G. L. J. A. Rikken, *Spontaneous emission from a dielectric slab*, Phys. Rev. A **57**, 3913–3930 (1998).

[61] H. Haken, *Laser light dynamics*, North Holland, Amsterdam, 1986.

[62] M. Pu, Q. Feng, M. Wang, C. Hu, C. Huang, X. Ma, Z. Zhao, C. Wang, and X. Luo, *Ultrathin broadband nearly perfect absorber with symmetrical coherent illumination*, Opt. Expr. **20**, 2246 (2012).

[63] B. Gjonaj, J. Aulbach, P. M. Johnson, A. P. Mosk, L. Kuipers, and A. Lagendijk, *Active spatial control of plasmonic fields*, Nat. Photon. **5**, 360 (2011).

[64] R. Mueller-Mach, G. O. Mueller, M. R. Krames, O. B. Schehin, P. J. Schimdt, H. Bechtel, C. Chen, and O. Steigelmann, *All-nitride monochromatic amber-emitting phosphor-converted light-emitting diodes.*, Phys. Status Solidi RRL **3**, 215 (2009).

[65] A. Ikesue and I. Furusato, *Fabrication of polycrystalline, transparent YAG ceramics*, J. Am. Ceram. Soc. **78[1]**, 225 (1995).

[66] S. Chen, L. Zhang, K. Kisslinger, and Y. Wu, *Transparent $Y_3 Al_5 O_{12}$: Li, Ce Ceramics for Thermal Neutron Detection*, J. Am. Ceram. Soc. **96[4]**, 1067–1069 (2013).

[67] R. Boulesteix, A. Maitre, L. Chraetien, Y. Rabinovitch, and C. Salla, *Microstructural Evolution During Vacuum Sintering of Yttrium Aluminum Garnet Transparent Ceramics: Toward the Origin of Residual Porosity Affecting the Transparency*, J. Am. Ceram. Soc. **9**, 1724–1731 (2013).

[68] F. Bonaccorso, Z. Sun, T. Hasan, and A. C. Ferrari, *Graphene Photonics and Optoelectronics*, Nat. Photon. **4**, 611 (2010).

[69] K. S. Novoselov, *Nobel Lecture: Graphene: Materials in the Flatland*, Rev. Mod. Phys. **83**, 837 (2011).

[70] A. N. Grigorenko, M. Polini, and K. S. Novoselov, *Graphene plasmonics*, Nat. Photon. **6**, 749 (2012).

[71] S. Gilje, S. Han, M. Wang, K. L. Wang, and R. B. Kaner, *A Chemical Route to Graphene for Device Applications*, Nano Lett. **7**, 3394 (2007).

[72] S. Bae, H. Kim, Y. Lee, X. Xu, Y. Park, Y. Zheng, J. Balakrishnan, T. Lei, H. R. Kim, and Y. I. t. Song, *Roll-to-roll Production of 30-inch Graphene Films for Transparent Electrodes*, Nat. Nanotech. **5**, 574 (2010).

[73] W. D. C. Tan, Y. Su, R. J. Knize, G. Q. Xie, L. J. Li, and D. Y. Tang, *Mode Locking of Ceramic Nd:Yttrium Aluminum Garnet with Graphene as a Saturable Absorber*, Appl. Phys. Lett. **96**, 031106 (2010).

[74] Q. Bao, H. Zhang, B. Wang, Z. Ni, C. H. Y. Xuan Lim, Y. Wang, D. Y. Tang, and K. P. Loh, *Broadband Graphene Polarizer*, Nat. Photon. **5**, 411 (2011).

[75] T. Mueller, F. Xia, and P. Avouris, *Graphene Photodetectors for High-Speed Optical Communications*, Nat. Photon. **4**, 297 (2010).

[76] T. Stauber, N. M. R. Peres, and A. K. Geim, *Optical Conductivity of Graphene in the Visible Region of the Spectrum*, Phys. Rev. B **78**, 085432 (2008).

[77] A. B. Kuzmenko, E. van Heumen, F. Carbone, and D. van der Marel, *Universal Optical Conductance of Graphite*, Phys. Rev. Lett. **100**, 117401 (2008).

[78] F. Xia, T. Mueller, Y.-M. Lin, A. Valdes-Garcia, and P. Avouris, *Ultrafast Graphene Photodetector*, Nat. Nanotech. **4**, 839 (2009).

[79] K. Kim, J. Choi, T. Kim, C. S., and H. Chung, *A Role for Graphene in Silicon-Based Semiconductor Devices*, Nature **479**, 338 (2011).

[80] T. Ando, Y. Zheng, and H. Suzuura, *Dynamical Conductivity and Zero-Mode Anomaly in Honeycomb Lattices*, J. Phys. Soc. Jpn. **71**, 1318 (2002).

[81] V. P. Gusynin, S. G. Sharapov, and J. P. Carbotte, *Unusual Microwave Response of Dirac Quasiparticles in Graphene*, Phys. Rev. Lett **96**, 256802 (2006).

[82] V. P. Gusynin, S. G. Sharapov, and J. P. Carbotte, *Optical far-infrared properties of a graphene monolayer and multilayer*, Phys. Rev. B **76**, 153410 (2007).

[83] A. Y. Nikitin, F. Guinea, F. J. Garcia-Vidal, and L. Martin-Moreno, *Optical far-infrared properties of a graphene monolayer and multilayer*, Phys. Rev. B **84**, 195446 (2011).

[84] E. Hecht, *Optics*, Addison-Weesley Longman Inc., 1998.

[85] S. Thongrattanasiri, F. H. L. Koppens, and F. J. García de Abajo, *Complete Optical Absorption in Periodically Patterned Graphene*, Phys. Rev. Lett. **2**, 108 (2012).

[86] Y. A. Nikitin, F. Guinea, F. J. Garcia-Vidal, and L. Martin-Moreno, *Fields radiated by a nanoemitter in a graphene sheet*, Phys. Rev., B **84**, 195446 (2011).

[87] A. J. R. Cole and N. J. Halas, *Optimized Plasmonic Nanoparticle Distributions for Solar Spectrum Harvesting*, Appl. Phys. Lett. **89**, 153120 (2006).

[88] N. I. Landy, S. Sajuyigbe, J. J. Mock, D. R. Smith, and W. J. Padilla, *Perfect Metamaterial Absorber*, Phys. Rev. Lett. **100**, 207402 (2006).

[89] V. Teperik, F. J. Garcia de Abajo, A. G. Borisov, M. Abdelsalam, P. N. Bartlett, Y. Sugawara, and J. J. Baumberg, *Omnidirectional Absorption in Nanostructured Metal Surfaces*, Nat. Photon. **2**, 299 (2008).

[90] M. Liu, X. Yin, E. Ulin-Avila, B. Geng, T. Zentgraf, L. Ju, W. F., and X. Zhang, *A Graphene-Based Broadband Optical Modulator*, Nature **474**, 64 (2011).

[91] H. Li, Y. Anugrah, K. S. J., and M. Li, *Optical Absorption in Graphene Integrated on Silicon Waveguides*, Appl. Phys. Lett **101**, 111110 (2012).

[92] M. Furchi, A. Urich, A. Pospischil, G. Lilley, K. Unterrainer, H. Detz, P. Klang, A. M. Andrews, W. Schrenk, and S. G. *et al.*, *Microcavity-Integrated Graphene Photodetector*, Nano Lett. **12**, 2773 (2012).

[93] M. Engel, M. Steiner, A. Lombardo, A. C. Ferrari, H. v. Loneysen, A. P., and R. Krupke, *Light-Matter Interaction in a Microcavity-Controlled Graphene Transistor*, Nat. Commun. **3**, 2773 (2012).

[94] A. Ferreira, N. M. R. Peres, R. M. Ribeiro, and T. Stauber, *Graphene-Based Photodetector with Two Cavities*, Phys. Rev. B **85**, 115438 (2012).

[95] T. J. Echtermeyer, L. Britnell, A. Lombardo, R. V. Gorbachev, A. N. Grigorenko, A. K. Geim, A. C. Ferrari, and K. S. Novoselov, *Strong Plasmonic Enhancement of Photovoltage in Graphene*, Nat. Commun. **2**, 458 (2001).

[96] Z. Fang, Y. Wang, A. E. Schlather, Z. Liu, P. M. Ajayan, F. J. Garcia de Abajo, P. Nordlander, X. Zhu, and N. J. Halas, *Active Tunable Absorption Enhancement with Graphene Nanodisk Arrays*, Nano Lett. **14**, 299 (2014).

[97] A. Y. Nikitin, F. Guinea, and L. Martin-Moreno, *Resonant plasmonic effects in periodic graphene antidot arrays*, Appl. Phys. Lett. **101**, 151119 (2012).

[98] *Graphene Supermarket*, **https://www.graphene-supermarket.com**.

[99] X. Li, Y. Zhu, W. Cai, M. Borysiak, B. Han, D. Chen, R. D. Piner, L. Colombo, and R. S. Ruoff, *Transfer of Large-Area Graphene Films for High-Performance Transparent Conductive Electrodes*, Nano Lett. **9**, 4359 (2009).

[100] V. G. Kravets, A. N. Grigorenko, R. R. Nair, P. Blake, S. Anissimova, N. K.S., and A. H. Geim, *Spectroscopic Ellipsometry of Graphene and an Exciton-Shifted van Hove Peak in Absorption*, Phys. Rev. B **81**, 155413 (2010).

[101] A. C. Ferrari, J. C. Meyer, V. Scardaci, C. Casiraghi, M. Lazzeri, F. Mauri, S. Piscanec, D. Jiang, and K. S. t. Novoselov, *Raman Spectrum of Graphene and Graphene Layers*, Phys. Rev. Lett. **97**, 187401 (2006).

[102] A. Gupta, G. Chen, P. Joshi, T. S., and P. C. Eklund, *Raman Scattering from High-Frequency Phonons in Supported n-Graphene Layer Films*, Nano Lett. **6**, 2667 (2006).

[103] S. Reich and C. Thomsen, *Raman Spectroscopy of Graphite*, Phil. Trans. R. Soc. Lond. A **97**, 2271 (2004).

[104] Z. Ni, Y. Wang, Y. T., and Z. Shen, *Raman Spectroscopy and Imaging of Graphene*, Nano Res. **1**, 273 (2008).

[105] Y. V. Bludov, M. I. Vasilevskiy, and N. M. R. Peres, *Tunable Graphene-Based Polarizer*, J. Appl. Phys. **112**, 084320 (2012).

[106] Y. V. Bludov, M. I. Vasilevskiy, and N. M. R. Peres, *Mechanism for Graphene-Based Optoelectronic Switches by Tuning Surface Plasmon-Polaritons in Monolayer Graphene*, Europhys. Lett. **92**, 68001 (2010).

[107] M. Klopfleisch, G. M., and U. Trutschel, *Experimental Verification of a Virtual-Mode Treatment for the Excitation of Surface Plasmon Polaritons by Attenuated Total Reflection*, Appl. Opt. **31**, 5017 (1992).

[108] P. Blake, E. W. Hill, A. H. Castro Neto, K. S. Novoselov, D. Jiang, R. Yang, T. J. Booth, and A. K. Geim, *Making Graphene Visible*, Appl. Phys. Lett. **91**, 063124 (2007).

[109] G. Pirruccio, G. Lozano, Y. Zhang, S. R. K. Rodriguez, R. Gomes, H. Z., and J. Gomez Rivas, *Coherent Absortpion and Enhanced Photoluminescence in Thin Layers of Nanorods*, Phys. Rev. B **85**, 165455 (2012).

[110] M. S. A. and K. Ziegler, *New Electromagnetic Mode in Graphene*, Phys. Rev. Lett. **99**, 016803 (2007).

[111] A. Rogalski, *Infrared detectors: status and trends.*, Prog. Quant. Electron. **27**, 59–210 (2003).

[112] J. Clark and G. Lanzani, *Organic photonics for communications.*, Nat. Photon. **4**, 438 (2010).

[113] J. H. Chen and *et. al.*, *Intrinsic and Extrinsic Performance Limits of Graphene Devices on SiO_2*, Nat. Nanotech. **3**, 206 (2008).

[114] R. R. Nair, P. Blake, A. N. Grigorenko, K. S. Novoselov, T. J. Booth, T. Stauber, N. M. R. Peres, and A. K. Geim, *Fine Structure Constant Defines Visual Transparency of Graphene*, Science **320**, 1308 (2008).

[115] L. Britnell and *et. al*, *Strong Light-Matter Interactions in Heterostructures of Atomically Thin Films*, Science **340**, 1311 (2013).

[116] G. Konstantatos and *et al.*, *Hybrid graphene–quantum dot phototransistors with ultrahigh gain.*, Nature Nanotech. **7**, 363–368 (2012).

[117] G. Pirruccio, L. Martin-Moreno, G. Lozano, and J. Gomez-Rivas, *Coherent and broadband enhanced optical absorption in graphene*, ACS Nano **7**, 4810 (2013).

[118] Y. Zhang, T. Liu, B. Meng, X. Li, G. Liang, X. Hu, and O. J. Wang, *Broadband high photoresponse from pure monolayer graphene photodetector*, Nat. Commun. **4**, 1811 (2013).

[119] C. Liu, Y. Chang, T. B. Norris, and Z. Zhong, *Graphene photodetectors with ultra-broadbandand high responsivity at room temperature*, Nat. Nanotech. **9**, 273–278 (2014).

[120] Z. Fang, Z. Liu, Y. Wang, P. M. Ajayan, P. Nordlander, and N. J. Halas, *Graphene-antenna sandwich photodetector.*, Nano Lett. **12**, 3808–3813 (2012).

[121] Y. Liu, R. Cheng, L. Liao, H. Zhou, J. Bai, G. Liu, L. Liu, Y. Huang, and X. Duan, *Plasmon resonance enhanced multicolour photodetection by graphene*, Nat. Commun. **2**, 579 (2011).

[122] G. de Abajo F. J. and J. J. Saenz, *Electromagnetic surface modes in structured perfect-conductor surfaces*, Phys. Rev. Lett. **95**, 233901 (2005).

[123] K. T. Carron, W. Fluhr, M. Meier, A. Wokaun, and H. W. Lehmann, *Resonances of twodimensional particle gratings in surface-enhanced Raman scattering*, J. Opt. Soc. Am. B **3**, 430 (1986).

[124] S. Zou, N. Janel, and S. G. C., *Silver nanoparticle array structures that produce remarkably narrow plasmon lineshapes*, J. Chem. Phys. **120**, 10871 (2004).

[125] Z. S. and S. G. C., *Narrow plasmonic/photonic extinction and scattering line shapes for one and two dimensional silver nanoparticle arrays*, J. Chem. Phys. **121**, 12606 (2004).

[126] E. M. Hicks, S. Zou, G. C. Schatz, K. G. Spears, R. P. Van Duyne, L. Gunnarsson, T. Rindzevicius, B. Kasemo, and M. Kall, *Controlling Plasmon Line Shapes through Diffractive Coupling in Linear Arrays of Cylindrical Nanoparticles Fabricated by Electron BeamLithography*, Nano Lett. **5**, 1065 (2005).

[127] A. Christ, S. G. Tikhodeev, N. A. Gippius, J. Kuhl, and H. Giessen, *Waveguide-Plasmon Polaritons: Strong Coupling of Photonic and Electronic Resonances in a Metallic Photonic Crystal Slab*, Phys. Rev. Lett. **91**, 183901 (2003).

[128] T. Zentgraf, S. Zhang, R. F. Oulton, and X. Zhang, *Ultranarrow coupling-induced transparency bands in hybrid plasmonic systems*, Phys. Rev. B **80**, 195415 (2009).

[129] S. R. K. Rodriguez, S. Murai, M. A. Verschuuren, and J. Gomez Rivas, *Light-emitting waveguide-plasmon polaritons*, Phys. Rev. Lett. **109**, 166803 (2012).

[130] V. Ferry, M. A. Verschuuren, H. B. T. Li, E. Verhagen, R. J. Walters, R. E. I. Schropp, H. A. Atwater, and A. Polman, *Light trapping in ultrathin plasmonic solar cells*, Opt. Expr. **18**, A237 (2010).

[131] P. Spinelli, V. E. Ferry, J. van de Groep, M. van Lare, M. A. Verschuuren, R. E. I. Schropp, H. A. Atwater, and A. Polman, *Plasmonic light trapping in thin-film Si solar cells*, J. Opt **14**, 024002 (2012).

[132] M. van Lare, F. Lenzmann, M. A. Verschuuren, and A. Polman, *Mode coupling by plasmonic surface scatterers in thin-film silicon solar cells*, Appl. Phys. Lett. **101**, 221110 (2012).

[133] T. V. Teperik and A. Degiron, *Design strategies to tailor the narrow plasmon-photonic resonances in arrays of metallic nanoparticles*, Phys. Rev. B **86**, 245425 (2012).

[134] W. L. B. O. H. G. Weick, C. Woollacott and E. Mariani, *Dirac-like Plasmons in Honeycomb Lattices ofMetallic Nanoparticles*, Phys. Rev. Lett. **110**, 106801 (2013).

[135] S. Murai, M. A. Verschuuren, G. Lozano, G. Pirruccio, S. R. K. Rodriguez, and J. Gomez Rivas, *Hybrid plasmonic-photonic modes in diffractive arrays of nanoparticles coupled to light-emitting optical waveguides*, Opt. Expr. **21**, 4250 (2013).

[136] B. Auguie, X. M. Bendana, W. L. Barnes, and F. J. Garcia de Abajo, *Diffractive arrays of gold nanoparticles near an interface: Critical role of the substrate*, Phys. Rev. B. **82**, 155447 (2010).

[137] F. H. L. Koppens, D. E. Chang, and F. J. García de Abajo, *Graphene Plasmonics: A Platform for Strong Light-Matter Interactions*, Nano Lett. **11**, 3370–3377 (2011).

[138] A. Taflove, *Comptational electrodynamics: the finite-difference time-domain method*, Artech house, Boston, 1995.

[139] X. Zhu and *et al.*, *Enhanced Light-Matter Interactions in Graphene-Covered Gold Nanovoid Arrays*, Nano Lett. **13**, 4690 (2013).

[140] K. Kishino, M. Selim Unlu, and H. Morkoc, *Resonant cavity-enhanced photodetectors*, IEEE J. Quantum Electron. **27**, 2025 (1991).

[141] *Graphenea*, **http://www.graphenea.com/**.

[142] S. Murai, K. Fujita, K. Iwata, and K. Tanaka, *Scattering-based hole burning in $Y_3 Al_5 O_{12} : Ce^{3+}$ monoliths with hierarchical porous structures prepared via the sol–gel route*, J. Phys. Chem. C **115(36)**, 17676–17681 (2011).

[143] K. Iwata, K. Fujita, S. Murai, and K. Tanaka, *Photobleaching in $Y_3 Al_5 O_{12} : Ce^{3+}$ macroporous monoliths prepared via sol-gel route accompanied by phase separation*, IOP Conf. Ser.: Mater. Sci. Eng. **18(5)**, 052003 (2011).

[144] Y. Tokudome, K. Fujita, K. Nakanishi, K. Kanamori, K. Miura, Hirao, and T. Hanada, *Sol-gel synthesis of macroporous YAG from ionic precursors via phase separation route*, J. Ceram. Soc. Jpn. **115(1348)**, 925–928 (2007).

[145] S. Murai, K. Fujita, K. Iwata, and K. Tanaka, *Optical properties of macroporous $Y_3Al_5O_{12}$ crystals doped with rare earth ions synthesized via sol-gel process from ionic precursors*, Opt. Mater. **33(2)**, 123–127 (2010).

[146] H. Kozuka and H. Kajimura, *Achievement of crack-free $BaTiO_3$ films over 1 µm in thickness via non-repetitive dip-coating*, Chem. Lett. **28(10)**, 1029–1030 (1999).

[147] M. Born and E. Wolf, *Principles of optics*, Cambridge University Press, 6th edition, 1997.

SUMMARY

Light plays a very fundamental role in every day life. Optical properties such as color, transparency, opacity are determined by the way in which objects scatter light. Light absorption can be interpreted as a particular case of scattering. The control of absorption is experiencing a rapidly increasing interest both in fundamental and applied research. Absorption has been regarded for long time as a secondary and unmanageable phenomenon, thus developing ways to externally control it is a growing field in its infancy. Acting on absorption allows to design the amount of energy delivered to a specific spatial location of an object and predict the amount of energy dissipated in it. The control on the optical absorption allows for the design and the optimization of novel optoelectronic devices, such as solar cells, photodetectors or light-emitting diodes. To increase the efficiency of such devices it is crucial to enhance the interaction of light with them, i.e. their optical absorption. However, many of the mentioned devices are based on materials which are inherently weakly absorbing, therefore one of the biggest challenges is to find ways to boost their absorption. This thesis focuses on the interaction of light with weakly absorbing materials, such as light emitting layers and graphene. By properly structuring the illumination pattern and the materials, we describe and exploit new ways to considerably enhance light absorption. The materials investigated in this thesis play a crucial role in lighting applications and photodetection.

In chapter 1 we introduce the fundamental concept of optical absorption and we revise the literature describing new methods to externally control and modulate the absorption of a given structure. These methods rely on the superposition principle of electromagnetic waves. In particular, the concept of Coherent Perfect Absorption provides a general framework for the manipulation of the absorption and demonstrates that the way a medium absorbs depends not only on its optical constants and the frequency of the incident radiation, but also on the detailed spatial distribution of the incident fields. Because the absorption is a phase-dependent quantity, structuring the phasefront of the incident wave or externally controlling the relative phase between multiple incident waves, allow to gain control over the absorption of a given material.

In chapter 2 we use a single beam illumination to demonstrate in two experiments a

large light absorptance in a thin layer of quantum dots in rods and Ce^{3+} doped yttrium aluminium garnet, $Y_3Al_5O_{12}$ (YAG:Ce). This behavior is explained in two complementary ways: in the first experiment we describe the result in terms of the coherent absorption by interference of the light incident at a certain angle on the layers. In the second experiment, light couples to the fundamental waveguide mode in the YAG:Ce layer where it is eventually absorbed, resulting in an enhanced absorption. We exploit this coherent light absorption to enhance the photoluminescent emission from the light emitting layers. A photoluminescence enhancement factor of 7 and 30 is measured for the two systems, respectively.

So far we have described how it is possible to control the absorption engineering the interference of scattered waves originating from the interaction of one beam with the sample. In chapter 3 we propose a multiple beam illumination scheme to experimentally demonstrate the possibility of external control and modulation of the intensity of the light emitted by a luminescent layer. This is realized through a tunable optical absorption of the incident light into the layer at a wavelength longer than the wavelength at which the absorption coefficient of the phosphor is maximum. The experiment is designed to get as close as possible to the condition of Coherent Perfect Absorption (CPA), realized by externally acting on the phase difference between the incident beams. When a destructive interference pattern is built outside the layer of luminescent material the incident light is efficiently absorbed. We elucidate the experimental difficulties in achieving CPA in a layer of YAG:Ce. Nevertheless, we theoretically demonstrate that our design can allow for a reduction of 35% of the Stokes' shift and, therefore, an increase in the efficiency of the system.

Graphene has been recognized as a revolutionary material for opto-electronic applications and in particular for photodetection because of its broadband absorption and its high carrier mobility. Nevertheless, the efficiency of such devices is limited by the limited absolute absorption per graphene layer. In order to increase the absorption in graphene, in chapter 4 we propose a multilayer structure in an Attenuated Total Reflectance (ATR) configuration. We experimentally demonstrate a broadband enhancement of the light absorption in graphene over the whole visible spectrum. We reach an enhancement factor of almost an order of magnitude in our geometry with respect to the absorption of bare graphene, which we explain in terms of coherent absorption arising from interference and dissipation. We demonstrate this result for a single- and multi-layer of graphene. The interference mechanism leading to the phenomenon of coherent absorption allows for its precise control by varying the refractive index and/or thickness of the medium surrounding the graphene.

Following the ideas presented in chapter 4, in chapter 5 we present a novel design for a graphene-based photodetector, which aims to enhance the light absorption of a single layer of graphene by engineering the electric field intensity enhancement at the location of the graphene layer. The multilayer structure makes use of a metallic array of nanoparticles as a coupling element for the incident light in the structure, in a similar way as the prism

was employed in the ATR experiment. In a first place this allows to miniaturize the device and facilitates the integration in complex photonic devices. The metallic array sustains collective hybrid plasmonic-photonic resonances arising from the radiative coupling of localized plasmon resonances. We propose the use of a quasi-waveguide mode because it generates a spatial distribution of enhanced electric field conveniently overlapping with the area covered by the graphene. We calculate that this mode allows for a wavelength-dependent enhancement of the optical absorption of graphene by a factor 7, introducing an advantageous spectral specificity which was lacking in the design investigated in chapter 4. A photocurrent enhancement proportional to the absorption enhancement is predicted.

LIST OF PUBLICATIONS

This thesis is based on the following publications:

1. *Coherent absorption and enhanced photoluminescence in thin layers of nanorods*, G. Pirruccio, G. Lozano, Y. Zhang, S. R. K. Rodriguez, R. Gomes, Z. Hens and J. Gómez Rivas, Phys. Rev. B **85**, 165455 1-6 (2012). **(Chapter 2)**

2. *Enhanced absorption and emission of $Y_3Al_5O_12$:Ce^{3+} thin layers prepared by epoxide-catalyzed sol-gel method*, S. Murai, M. A. Verschuuren, G. Lozano, G. Pirruccio, A.F. Koenderink and J. Gómez Rivas, Opt. Mater. Express **2**, 1111-1120 (2012). **(Chapter 2)**

3. *Coherent modulation of light generation and Stokes' shift reduction*, G. Pirruccio, J. Gómez Rivas, in preparation. **(Chapter 3)**

4. *Coherent and broadband enhanced optical absorption in graphene*, G. Pirruccio, L. Martin Moreno, G. Lozano and J. Gómez Rivas, ACS Nano **7(6)**, 4810 - 4817 (2013). **(Chapter 4)**

5. *Enhanced light absorption in graphene by arrays of nanoantennas*, G. Pirruccio, J. Giesbers, M. Ramezani, J. Gómez Rivas, in preparation. **(Chapter 5)**

Other publications by the author:

1. *Hybrid plasmonic-photonic modes in diffractive arrays of nanoparticles coupled to light-emitting optical waveguides*, S. Murai, M. A. Verschuuren, G. Lozano, G. Pirruccio, S. R. K. Rodriguez, and J. Gómez Rivas, Opt. Expr. **21**, 4250 (2013).

2. *Excitation of confined modes in particle arrays*, X. M. Bendana, G. Lozano, G. Pirruccio, J. Gómez Rivas and F. J. Garcia de Abajo, Opt. Expr. **21**, 5636 (2013).

3. *Long-range guided THz radiation by thin layers of water*, R. Sczech, J. Gómez Rivas, A. Berrier, V. Giannini, G. Pirruccio, C. Debus, H. Schafer-Eberwein, and P. H. Bolivar, Opt. Expr. **20**, 27781-27791 (2012).

4. *Design, fabrication and characterization of plasmonic gratings for SERS*, F. Romanato, R. Pilot, M. Massari, T. Ongarello, G. Pirruccio, P. Zilio, G. Ruffato, M. Carli, D. Sammito, V. Giorgis, D. Garoli, R. Signorini, P. Schiavuta, R. Bozio, Microelectron. Eng. **88**, 2717-2720 (2011).

Patents:

1. *Enhanced light coupling in 2D materials*, J. Giesbers, G. Pirruccio, M. Ramezani, T. Frach, R. Balkenende and J. Gómez Rivas, EU and US Patent Application in collaboration with Philips, Patent pending.

2. *Coherent absorption for Stokes shift reduction, modulation and increase of the photoluminescence intensity of phosphor-based lighting applications*, G. Pirruccio, J. Gómez Rivas, EU and US Patent Application in collaboration with Philips, Patent pending.

ACKNOWLEDGMENTS

When I arrived to The Netherlands for my PhD I did not have a crystal clear idea of what my life as a scientist would have been in the coming four years. Surely, thanks to the experience in my former group at the University of Padua, I had a clue of what a PhD project looks like and that exciting feeling was the one that brought me here making me undertake this challenge. The PhD has been my first valuable working experience. Although it was not the first time that I was taking first person responsibilities, it has been the first time that I felt the ownership of a result coming out of a long-period work. Suddenly, a positive result was not anymore just a small step forward in my private career but, as a consequence of the publication *iter*, it becomes a publicly acknowledged and recognized success.

Carrying out a research project is not only about science. It corresponds to a growth as a person and as part of the society. As such, with the honors come the duties. I always found fascinating and profound that universities not only recognize the value of the student by providing him with the title of doctor, but also point out the obligations associated with that title: intellectual honesty, high ethical standards and respect for the institutions. Obviously, this evolution in the consciousness does not come out of the blue at the moment of the final ceremony. It is a hard path which passes through many successes and many failures, during which it is easy to loose prospective, hope or feeling lost. The person who is in charge to be the guide of a PhD student is the supervisor. In my case this role has been played by Jaime Gómez Rivas. Jaime, I am very grateful to you, certainly for your help and your time spent with me during scientific meetings, but also because of all our discussions at lunch ranging from political problems, to society issues and hypothetical future scenarios. I always found those discussions intellectually stimulating and passionate. Working with you has been a pleasure but also a challenge, you have been supporting in the (very few) hard times, exciting and stimulating in the good ones. Thank you also for the openness you demonstrated me at the personal level.

Although a PhD is typically an individual project, it is impossible to accomplish it without the help of colleagues and collaborators. First of all I would like to thank all the members of the Surface Photonics group. It has been a great pleasure to share labs and offices

with you, struggling every day to get our results. Yichen, you have been the first one who introduced me to an optical lab, I have been lucky to inherit from you the 'seed' of my first project and to have you as a mentor following me on a daily basis. Gabriel, you have been my closest collaborator for three years, many parts of this thesis would not have been possible without your constant input and without all our exciting discussions. As i told you many times, I strongly believe that having a colleague directly involved in your own project and with whom discuss constantly, is the best and most efficient way to get the work done quickly and well. Thank you for your motivating attitude, for cheering me up and for your friendship. Of course I cannot forget about all our cooking sessions, dinners and beers that we had along the way and all the wonderful time spent together outside work. Grzegorz, we got to know each other more in the last year than in the previous three. Not only because we were sharing the same office, but also because of personal reasons. I want to thank you for all the fruitful suggestions and tips in the lab and for life. And of course, our 2000-mile trip around the USA was definitely a great experience. Working in the lab, I could not avoid to share my enthusiasm and my complains with your first student, Yannik. It was quite comforting to have someone arriving before me in the morning and often leaving after me in the evenings. Said, discussing with you has been always a good experience, it often made me look at things (scientifically and not) from a different prospective, thanks also for the help and suggestion about my holiday trips. Mohammad, it is nice to know that someone will take over and continue my unfinished projects. I am sure you will do a great job and I wish you lots of success with your PhD. Martijn, Giorgos, Arkabrata, Hemant, we had a limited interaction due to the different work location, but I thank you for your helpful comments during the group meetings. One of most remarkable experience that my PhD offered me was to get in contact with completely different cultures. The collaboration with Shunsuke, which generated the part of the results of Chapter 2, represents the most clear example. I am happy to have met you and to have worked with you. Dick, Tommy, Tom, i want to thank you for you contribution to the well-being in the group.

I spent the great majority of my time in the Philips Research environment. The collaboration with Philips has been of crucial importance for me, since I could appreciate the differences, the advantages and the disadvantages of research carried out in a company in respect with the academic one. Particularly important has been the collaboration with Marc Verschuuren, with whom I had great scientific discussions and who was responsible for the fabrication of the sample used in Chapter 5. As part of the Metamaterials group, I could appreciate the actual potential of the application of pour fundamental research. I have to thank Marc Verschuuren, Dick de Boer, Remco van Brakel and Manuela Lunz for this opportunity. Eugene Timmering, Hans Cillessen, Toon de Win, Frank van der Kruis, always available for any discussion and who helped me in the fabrication of the sample used in Chapter 3. During the last year I had the pleasure to collaborate with Jos Giesbers, who contributed to the results presented in Chapter 5, with Jack Boerekamp and Sandra Spoor wo fabricated the sample used in Chapter 2. In general I am grateful to Hans van Sprang and to all the members (including the formers) of the Photonics Materials and Devices group for hosting me in Philips during my PhD. Last but

not least, I thank Pauline Deuning for her administrative support.

At the same time I was also part of the Center for Nanophotonics at AMOLF. I am thankful to the group leaders, Femius Koenderink, Ad Lagendijk, Ewold Verhagen, Albert Polman, Erik Garnett and Kobus Kuipers for very positive and useful criticisms during the poster sessions and the nanophotonics colloquia. Also because of your comments the preparation of my oral presentations has been progressively smoother and qualitatively superior. Special thanks go also to everyone who looked carefully and positively critically to my results during the poster sessions. I also have to recognize the great quality and efficiency of the all staff of AMOLF, particularly evident during the setting-up of the demo for the Physics@FOM conference. Special thanks go to Henk-Jan Boluijt, who realized the cover of my thesis. I have to give credit to Albert Polman, the former, and to Vinod Subramian, the current director of AMOLF for making this possible.

After the people related with the work environment, I definitely cannot forget all the people that have lived with me and shared with me any kind of adventure during the last four years. People that made each day incredibly interesting, lively, crazy and breathtaking. Ciccio, Gabriele, Betty, Valentina, Nico, Salvatore, Laura, Christian, Mariusz, Manuel, Daniele, Agnese, Ginny, Alberto, Marco, Serena, Juan, I will never thank you enough for all the moments spent together, for our indissoluble friendship which transcends the limits of the physical distance and for the support you gave me in the hard times. You are family to me. You always succeeded in creating a relaxed atmosphere. Everyone knows very well which has been his/her role and I will leave the one-to-one thanks for a future more appropriate moment. Many other people played an important role in my personal life, among these I should mention Joan, Noemi, Sami, Florent and Paul.

During my life I moved a lot, I changed many cities. This helped me in shaping and strengthening my character. Initially I was not happy about the idea of moving from place to place and I did not understood the richness that each moving implies. Now I know that my father was right (most of the times) in pushing me to move and in describing each change as a challenge and as an enrichment, rather than a loss. It was an important life lesson. I understood that the physical distance is not an important parameter when it comes to true friendship and feelings. In each of the places where I have been living I met many friends, many of them are still present in my life regardless the limited occasions we have for seeing each other. I do not want to mention here all of you, it would be offensive to limit your contribution to a mere list. Nevertheless, thanks are indeed due to Francesca, Michele, Nicola, Matteo, Alessandro, Greg, Philips, Natasa and Andrea for the experiences we shared, for being present and for their help along my way.

Moving does not need to be permanent, also trips count in the personal growth and enrichment. And it is just during one of these trips that I met one of the most important person of my life. Izchell, our meeting and our story is among the most astonishing, intriguing and exciting I have ever lived. This year with you has been simply amazing, I am so happy that I met you and I fell in love with you. We have been through few hard

times and many more wonderful times, which contributed to make our feelings mature. Now your presence and your love in my life is tangible and irreplaceable. Ya no puedo esperar más para empezar nuestra vida juntos.

Infine voglio ringraziare la mia famiglia: i miei fratelli Andrea e Riccardo, mia madre Donatella e mio padre Salvatore per il vostro amore incondizionato, il vostro supporto, per aver sempre creduto in me, per le opportunitá ho avuto grazie a voi, per tutti i sacrifici che avete affrontato per permettermi di fare tutto ció che ho fatto, per la pazienza infinita dimostratami in tutti questi anni. I extend my thanks to all the rest of my relatives which are too many to be mentioned separately here, but that occupy an important place in my life.

<div align="right">

Thank you.
Giuseppe

</div>

ABOUT THE AUTHOR

Giuseppe Pirruccio was born in 1986 in Palermo, Italy. He studied Physics at the Universitá degli Studi di Padova in Italy and graduated Magna cum Laude Honors in 2010, with a thesis entitled "Plasmonic nanodevice for controlled Surface Enhanced Raman Spectroscopy". For his master thesis project he worked at the LaNN Laboratory in Padua under the supervision of prof. Filippo Romanato. In 2010 Giuseppe started his PhD studies in the Surface Photonics group under the supervision of prof. Jaime Gómez Rivas, within an Industrial Partnership Program between FOM Institute AMOLF and Philips in the Netherlands. During his PhD Giuseppe has investigated different ways to enhance light absorption in thin layers of weakly absorbing materials, such as light emitting layers and graphene. These materials play a crucial role in solid state lighting and in novel opto-electronic devices. Giuseppe has been coauthor of 7 published scientific articles in peer-reviewed journals, has filed 2 patent applications and given 5 talks at international and national conferences.